Optoelectronic Devices Using

2D Layered Materials



Qianyang Zhang

Supervised by Professor Jamie H. Warner

Department of Materials

St Cross College

University of Oxford

A thesis submitted for the degree of

Doctor of Philosophy

Declaration

The material contained within this thesis has not previously been submitted for a degree at the University of Oxford or any other university. The research reported within this thesis has been conducted by the author unless indicated otherwise.

Copyright Notice

The copyright of this thesis rests with the author. No quotation from it should be published without the prior written consent of the author, and any information derived from it should be acknowledged.

Abstract

Optoelectronic Devices Using 2D Layered Materials

By Qianyang Zhang

St Cross College

In pursuit of DPhil Degree, Trinity Term, 2021

The new diverse family of two-dimensional (2D) materials has aroused researchers' enormous interest as key components in next-generation optoelectronic devices. In this thesis, ultrathin all-2D devices based on graphene, molybdenum disulphide (MoS_2) and tungsten disulphide (WS_2), synthesized using the scalable bottom-up approach, are investigated in both single- and multi-stacked configurations.

The first chapter of results demonstrates a novel stacking method for assembling uniform-patterned periodic 2D arrays into vertical-layered heterostructures. The fabricated heterostructure, showing the photovoltaic effect, can serve as photodetectors, with graphene as electrodes and MoS_2 as the photo-absorber. All 2D materials used are grown into continuous films with only mono- or bilayer thickness. Each layer is prepatterned into a specific shape on a substrate and then transferred to the device substrate with aligned precision in the microrange by using interlocking marker pairs. Hundreds of identical devices are produced with 2D periodic spacing on a 1 cm × 1 cm SiO_2/Si substrate, which is a fundamental prerequisite for future pixelated detectors.

The second chapter of results explores the graphene-WS_2 van der Waals Schottky heterojunction. The device of WS_2 with laterally spaced graphene electrodes behaves as a diode with a rectification ratio up to 90 under a laser power of 1.37 μW at a bias voltage of ±3 V. This is attributed by the different dielectric environments of two graphene electrodes, leading to asymmetric Schottky barriers of $graphene_{bottom}$-WS_2 and $graphene_{top}$-WS_2. Both the laser illumination and back-gate voltage can tune the rectification behaviour of the device. Furthermore, a constant bias voltage applied to the device causes a strong electroluminescence in the junction area, with an average current of 2.16×10^{-5} A. This work contributes to the current understanding of the 2D metal−semiconductor heterojunction and offers an idea to obtain all-2D Schottky diodes by retaining the ultrathin device concept.

The third chapter of results shows a new type of photodetectors with an enhanced photodetecting efficiency by creating the multi-stacked heterostructure. The optoelectronic performances under different illumination intensities are studied. The average net photocurrent of the multi-stacked (graphene/WS_2/MoS_2/graphene/MoS_2/WS_2/graphene) device is around 2.3 times than that of the single-stacked (graphene/WS_2/MoS_2/graphene) one due to the improved light absorbed. This study brings forward a novel concept of multi-stacked architectures which extends the current research range and paves up ways for the high efficiency yet ultrathin photodetectors.

Acknowledgements

My doctoral study in Oxford has been blessed with a lot of generous support and encouragement, and I would like to use this opportunity to express my sincere gratitude to the following people who play important roles to me, without whom this thesis would not be completed.

First and foremost, thanks to my esteemed supervisor, **Prof. Jamie H. Warner**, who offered me a position to study in Oxford and guided me in my research. His insightful feedback and advice inspired me to think more deeply and brought my work to a higher level. I am eternally grateful for his invaluable supervision and continuous encouragement. It has always been my great fortune and honour to be his student.

I also want to show my appreciation to all the colleagues in the Nanostructured Materials Group for their collaborative efforts. **Dr. Yingqiu Zhou, Dr. Hefu Huang, Dr. Martin Tweedie and Dr. Viktoryia Shautsova** trained me all the techniques used for my research and shared a lot of precise experience in the device fabrication. **Dr. Yuewen Sheng, Dr. Wenshuo Xu, Dr. Ren-Jie Chang and Dr. Tongxin Chen** demonstrated the synthesis of 2D materials. **Linlin Hou** has been my closest co-worker and we often do experiments with each other. We together with **Yi Wen**, who is also my roommate, and **Jun Chen** participated in lots of lively discussions. I give thanks to **Yang Lu** for his kind help in providing high quality MoS_2 samples for my project. I also thanks **Dr. Xiaochen Wang, Dr. Sha Li, Dr. Si Zhou, Dr. Sapna Sinha and Peng Tang** for being nice labmates.

Thanks to **A/Prof. Guodong Meng** for inviting me to his lab in China for a short visit. I should also express my appreciation to the cleanroom manager, **Dr. Paul**

Pattinson, who takes charge of the world-class facilities. Also thanks to the IT manager, **Paul Warren**, for his support and advise on all computer issues, especially during my remote working period caused by the pandemic.

I should particularly acknowledge the **Chinese Scholarship Council (CSC)** for the scholarship during my study in University of Oxford. I also thank the **Department of Materials** for providing me the funding for the travel of conferences and a Materials Continuation Bursary for supporting my living expenses during the thesis revision.

To **my friends** in Oxford: I enjoy the time spending with you and hope to have the chance to meet with each of you again.

Finally, I dedicate this thesis to **my family**, especially to my dear mom and dad for their unconditional love and understanding. I am more grateful than I could express. You earn this degree right along with me.

Publications

Chapter 4

(1) **Zhang, Q.**; Hou, L.; Lu, Y.; Chen, J.; Zhou, Y.; Shautsova, V.; Warner, J. H. Large-Scale Uniform-Patterned Arrays of Ultrathin All-2D Vertical Stacked Photodetector Devices. ACS Applied Materials & Interfaces 2021, 13 (29), 34696–34704.

Chapter 5

(2) **Zhang, Q.**; Hou, L.; Shautsova, V.; Warner, J. H. Ultrathin All-2D Lateral Diodes Using Top and Bottom Contacted Laterally Spaced Graphene Electrodes to WS_2 Semiconductor Monolayers. (Submitted)

Co-Author Papers

(3) Huang, H.; Xu, W.; Chen, T.; Chang, R.-J.; Sheng, Y.; **Zhang, Q.**; Hou, L.; Warner, J. H. High-Performance Two-Dimensional Schottky Diodes Utilizing Chemical Vapour Deposition-Grown Graphene–MoS_2 Heterojunctions. ACS Applied Materials & Interfaces 2018, 10 (43), 37258–37266.

(4) Huang, H.; Sheng, Y.; Zhou, Y.; **Zhang, Q.**; Hou, L.; Chen, T.; Chang, R.-J.; Warner, J. H. 2D-Layer-Dependent Behavior in Lateral Au/WS_2/Graphene Photodiode Devices with Optical Modulation of Schottky Barriers. ACS Applied Nano Materials 2018, 1 (12), 6874–6881.

(5) Zhou, Y.; Xu, W.; Sheng, Y.; Huang, H.; **Zhang, Q.**; Hou, L.; Shautsova, V.; Warner, J. H. Symmetry-Controlled Reversible Photovoltaic Current Flow in Ultrathin All 2D Vertically Stacked Graphene/MoS_2/WS_2/Graphene Devices. ACS Applied Materials & Interfaces 2019, 11 (2), 2234–2242

(6) Chen, T.; Sheng, Y.; Zhou, Y.; Chang, R.; Wang, X.; Huang, H.; **Zhang, Q.**; Hou, L.; Warner, J. H. High Photoresponsivity in Ultrathin 2D Lateral Graphene:WS_2:Graphene Photodetectors Using Direct CVD Growth. ACS Applied Materials & Interfaces 2019, 11 (6), 6421–6430.

(7) Hou, L.; **Zhang, Q.**; Tweedie, M.; Shautsova, V.; Sheng, Y.; Zhou, Y.; Huang, H.; Chen, T.; Warner, J. H. Photocurrent Direction Control and Increased Photovoltaic Effects in All-2D Ultrathin Vertical Heterostructures Using Asymmetric H-BN Tunneling Barriers. ACS Applied Materials & Interfaces 2019, 11 (43), 40274–40282.

(8) Gerkman, M. A.; Lee, J. K.; Li, X.; **Zhang, Q.**; Windley, M.; Fonseca, M. V.; Lu, Y.; Warner, J. H.; Han, G. G. D. Direct Imaging of Individual Molecular Binding to Clean Nanopore Edges in 2D Monolayer MoS_2. ACS Nano 2019, 14 (1), 153–165.

(9) Chen, J.; Ryu, G. H.; **Zhang, Q.**; Wen, Y.; Tai, K.-L.; Lu, Y.; Warner, J. H. Spatially Controlled Fabrication and Mechanisms of Atomically Thin Nanowell Patterns in Bilayer WS_2 Using in Situ High Temperature Electron Microscopy. ACS Nano 2019, 13 (12), 14486–14499.

(10) Shautsova, V.; Sinha, S.; Hou, L.; **Zhang, Q.**; Tweedie, M.; Lu, Y.; Sheng, Y.; Porter, B. F.; Bhaskaran, H.; Warner, J. H. Direct Laser Patterning and Phase Transformation of 2D $PdSe_2$ Films for On-Demand Device Fabrication. ACS Nano 2019, 13 (12), 14162–14171.

(11) Tai, K.-L.; Chen, J.; Wen, Y.; Park, H.; **Zhang, Q.**; Lu, Y.; Chang, R.-J.; Tang, P.; Allen, C. S.; Wu, W.-W.; Warner, J. H. Phase Variations and Layer Epitaxy of 2D $PdSe_2$ Grown on 2D Monolayers by Direct Selenization of Molecular Pd Precursors. ACS Nano 2020, 14 (9), 11677–11690.

(12) Hou, L.; **Zhang, Q.**; Shautsova, V.; Warner, J. H. Operational Limits and Failure Mechanisms in All-2D van Der Waals Vertical Heterostructure Devices with Long-Lived Persistent Electroluminescence. ACS Nano 2020, 14 (11), 15533–15543.

(13) Hou, L.; Xu, W.; **Zhang, Q**.; Shautsova, V.; Chen, J.; Shu, Y.; Li, X.; Bhaskaran, H.; Warner, J. H. Ultrathin Lateral 2D Photodetectors Using Transition-Metal Dichalcogenides $PtSe_2$–WS_2–$PtSe_2$ by Direct Laser Patterning. ACS Applied Electronic Materials 2022, 4 (3), 1029–1038.

Table of Contents

List of Abbreviations ..... **x**

List of Symbols ..... **xii**

Chapter 1 Introduction **1**

1.1 Project Aims 1

1.2 Layout of this Thesis 1

Chapter 2 Literature Review **4**

2.1 Introduction 4

2.2 Fundamentals of 2D Materials 6

2.2.1 Graphene 6

2.2.2 TMDs 7

2.3 Preparation Methods of 2D Materials and Heterostructures 8

2.3.1 Production 8

2.3.2 Transfer and Stacking 18

2.4 Optoelectronics based on 2D Materials 22

2.4.1 Photodetectors 22

2.4.2 Electroluminescent Devices 41

2.5 Conclusions and Outlook 49

Chapter 3 Methodology **51**

3.1 Introduction 51

3.2 Synthesis of 2D Materials 52

3.2.1 Graphene 52

3.2.2 TMDs 53

3.3 Device Fabrication Process 54

3.3.1 2D Materials Transfer Method 54

3.3.2 Electron-Beam Lithography (EBL) 55

3.3.3 Metal Deposition 56

3.3.4 Reactive-Ion Etching (RIE) 57

3.4 Materials Characterization 58

3.4.1 Optical Microscopy (OM) 58

3.4.2 Scanning Electron Microscopy (SEM) 58

3.4.3 Raman and Photoluminescence (PL) Characterization 59

3.4.4 Annular Dark-Field Transmission Electron Microscopy (ADF-TEM) 60

3.5 Electrical and Optoelectrical Measurements 61

Chapter 4 Large-Scale Uniform-Patterned Arrays of Ultrathin All-2D Vertical Stacked

Photodetector Devices **63**
4.1 Introduction 63
4.2 Results and Discussions 64
4.2.1 Demonstration of the Marker-Assist-Aligned Stacking Method 64
4.2.2 Fabrication of Device Arrays 69
4.2.3 SEM, Raman and PL Characterization 70
4.2.4 Photodetecting Characterization 73
4.3 Conclusion 79
4.4 Contribution Statement 80
Chapter 5 Ultrathin All-2D Lateral Diodes Using Top and Bottom Contacted Laterally Spaced Graphene Electrodes to WS_2 Semiconductor Monolayers **81**
5.1 Introduction 81
5.2 Results and Discussion 82
5.2.1 Demonstration of the Asymmetric Structure 82
5.2.2 SEM, Raman and PL Characterization 84
5.2.3 Photodetecting Characterization 85
5.2.4 Light-emitting Characterization 90
5.3 Conclusion 96
5.4 Contribution Statement 97
Chapter 6 Single- and Multi-Stacked Heterostructures **98**
6.1 Introduction 98
6.2 Results and Discussions 99
6.2.1 Fabrication of the Single-Stacked Heterostructure 99
6.2.2 SEM, Raman and PL Characterization 101
6.2.3 Limitation of the Single-Stacked Heterostructure 103
6.2.4 Demonstration of the Multi-Stacked Heterostructure 104
6.2.5 Comparative Study on the Single- and Multi-Stacked Heterostructures 108
6.3 Conclusion 112
6.4 Contribution Statement 113
Chapter 7 Conclusion and Future Outlook **114**
7.1 Thesis Summary 114
7.2 Future Outlook 115
Appendix A Supporting Information of Chapter 4 ..... **117**
Appendix B Supporting Information of Chapter 5 ..... **121**
Appendix C Supporting Information of Chapter 6 ..... **123**
References **124**

List of Abbreviations

2D	Two-dimensional
ADF-TEM	Annular dark-field transmission electron microscopy
APS	Ammonium persulfate
CCD	Charged-coupled device
CMOS	Complementary metal-oxide-semiconductor
CNP	Charge neutrality point
CVD	Chemical vapour deposition
EBL	Electron-beam lithography
EL	Electroluminescence
FET	Field-effect transistors
FWHM	Full-width half maximum
Gr	Graphene
h-BN	Hexagonal boron nitride
IPA	Isopropanol
KOH	Potassium hydroxide
LED	Light-emitting diode
MoS_2	Molybdenum disulphide
MSH	Multi-stacked heterostructure
OM	Optical microscopy
PL	Photoluminescence
PMMA	Poly(methyl methacrylate)
RIE	Reactive ion etching

QE	Quantum efficiency
QW	Quantum well
SBH	Schottky barrier height
SEM	Scanning electron microscopy
SSH	Single-stacked heterostructure
TMD	Transition-metal dichalcogenide
VLH	Vertical layered heterostructure
WS_2	Tungsten disulphide

List of Symbols

c	Speed of light
D*	Detectivity
e	Elementary charge
G	Photogain
h	Planck’s constant
I	Current
P	Laser power
R	Photoresponsivity
V	Voltage
λ	Wavelength of light
ν	Frequency of light

Chapter 1 Introduction

1.1 Project Aims

This doctoral project aims to explore a new class of ultrathin, large-scale and good-performance yet high-density optoelectronic devices based on all two-dimensional (2D) materials. To be specific, transparent graphene (Gr) is utilized as the metallic electrodes and transition-metal dichalcogenides (TMDs), molybdenum disulphide (MoS_2) and tungsten disulphide (WS_2) in my case, act as the active semiconducting materials.

1.2 Layout of this Thesis

This thesis presents the research I carried out during my four years' DPhil study at the Department of Materials, University of Oxford. It starts with a literature review in *Chapter 2* that offers a broad overview of the state-of-the-art research in 2D materials that are exploited in this work. This includes fundamentals, preparation methods and also typical optoelectronic devices (particular focus on photodetectors and electroluminescent devices). The methodology in *Chapter 3* brings together all techniques of synthesis, fabrication and characterization applied to the research.

As for the core parts, *Chapter 4* illustrates my work on a novel stacking method for assembling uniform-patterned periodic 2D arrays into vertical-layered heterostructures on a large scale. The fabricated heterostructure, showing the photovoltaic effect, can serve as photodetectors with graphene as electrodes and MoS_2 as the photo-absorber. All 2D materials used are grown into continuous films with only mono- or bilayer thickness. Each layer is prepatterned into a specific shape on a substrate and then transferred to the device substrate with aligned precision in the microrange by using interlocking marker pairs. Hundreds of identical devices are produced with 2D periodic spacing on a 1 cm × 1 cm SiO_2/Si substrate. *Chapter 5* probes the graphene-WS_2 van der Waals Schottky heterojunction. The device of WS_2 with laterally spaced graphene electrodes behaves as a diode because the two graphene electrodes are in different dielectric environments. This leads to asymmetric Schottky barriers of $graphene_{bottom}$-WS_2 and $graphene_{top}$-WS_2. It is then evidenced by constructing $graphene_{bottom}$-WS_2-$graphene_{bottom}$ symmetric structure. Both the laser illumination and back-gate voltage can tune the rectification behaviour of the device. Furthermore, a constant bias voltage applied to the device causes a strong electroluminescence (EL) in the junction area, with an average current of 2.16×10^{-5} A. *Chapter 6* introduces a new type of photodetectors with an enhanced photodetecting efficiency by creating the multi-stacked configuration. The optoelectronic performances under different illumination intensities are studied. The multi-stacked (graphene/WS_2/MoS_2/graphene/MoS_2/WS_2/graphene) devices show an increased average net photocurrent, around 2.3 times than that of the single-stacked (graphene/WS_2/MoS_2/graphene) ones due to the improved light absorbed.

Finally, *Chapter 7* summarizes my DPhil work and ends by discussing the opportunities and challenges within this area in future studies.

Chapter 2 Literature Review

2.1 Introduction

Since the discovery of graphene in 2004[1], 2D materials have attracted significant attention across physics, chemistry and materials science due to their excellent properties. With a unique structure of atomic-layer thickness, these layered materials provide several advantages compared with the other existing materials. First, they are ultrathin, the thickness of which is just a few nanometres or less. Also, due to their high flexibility, they can be easily transferred to various substrates, which is important for the integration with the traditional microfabrication[2]. In addition, there are hundreds of possible 2D crystals that can be isolated, with different band gaps ranging from metals, semi-metals, semiconductors to insulators[3]. Therefore, it is possible to create an all-2D device with each material playing a specific role. Moreover, as shown in **Figure 2.1**, by stacking those 2D layers, one can create heterostructures which have strong interlayer coupling between each 2D material due to the van der Waals interactions[4,5]. This will lead to some interesting effects such as interlayer tunnelling, rapid exciton splitting for charge separation, and charge injection[6,7,8]. All of these make 2D materials promising in replacing the conventional materials in producing high-performance but compact devices. It is possible that 2D materials will bring a new

revolution in the next generation of optoelectronic applications, such as photodetectors, solar cells, light-emitting diodes (LEDs), and optical image sensors.

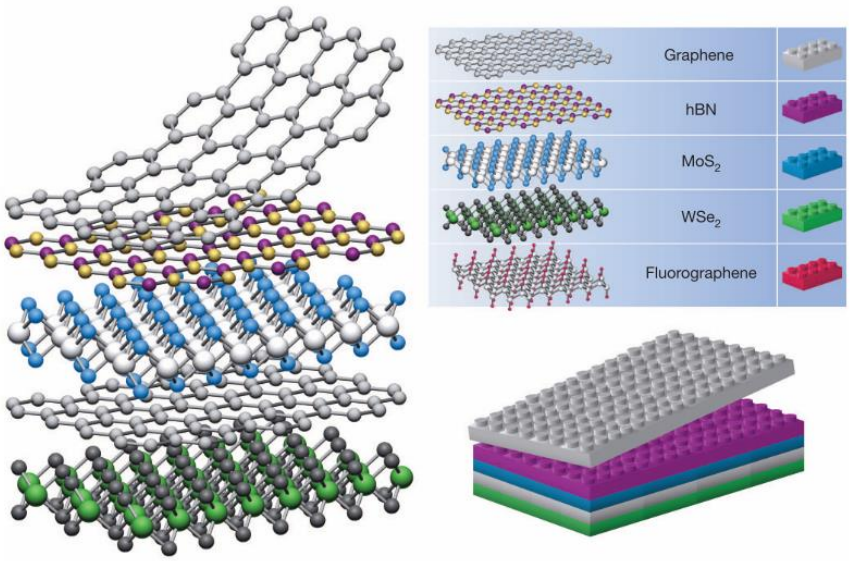


Figure 2.1 Different 2D materials, like 'Lego' on atomic scale, serving as building blocks for the assembly of various van der Waals heterostructures. Reproduced with permission from Ref 9. Copy right 2013, Nature Publishing Group.

This chapter reviews some essential progress of optoelectronic devices based on 2D materials. It starts with the fundamental properties of 2D materials, including graphene and TMDs, followed by the preparation methods for both the 2D materials and their heterostructures. Next is the 2D optoelectronics with main focus given to photodetectors and electroluminescent devices. Finally, a summary is presented with an outlook to help develop this field further.

2.2 Fundamentals of 2D Materials

2.2.1 Graphene

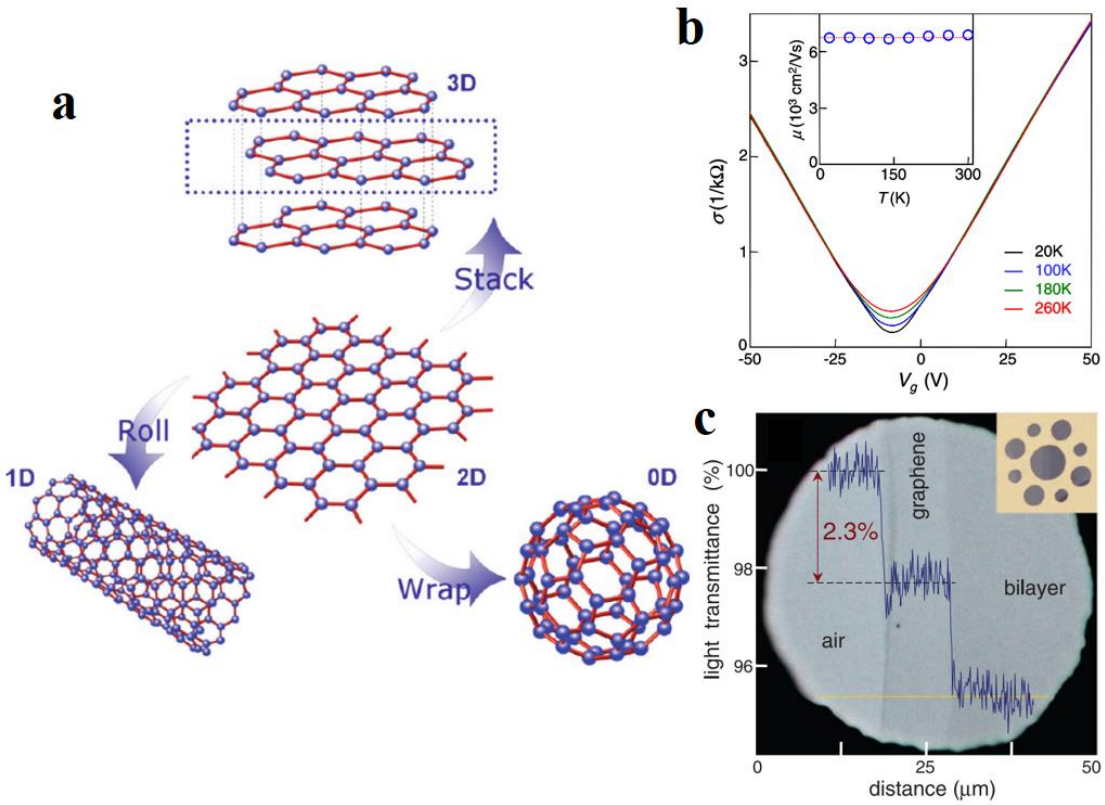


Figure 2.2 Properties of graphene. (a) Atomic models showing that graphene is the basic building block for other carbon materials. Reproduced with permission from Ref 10. Copy right 2012, American Chemical Society. (b) Conductivity σ of a bilayer graphene as a function of the gate voltage under different temperatures. Inset: mobility μ showing no change within 2%. Reproduced with permission from Ref 11. Copy right 2013, American Physical Society. (c) Image of a 50 mm aperture partially covered by mono- and bilayer graphene. Reproduced with permission from Ref 12. Copy right 2011, Macmillan Publishers Limited.

Monolayer graphene has only one-atom-layer thickness with sp2-hybridized carbon atoms in a honeycomb network. As displayed in **Figure 2.2**a, it is the basic building block for other carbon materials with various dimensionalities, such as 0D fullerenes, 1D nanotubes and 3D graphite[10]. As a semimetal with zero bandgap[13], it owns the following special properties: charge carriers behaving as massless Dirac fermions[14], giant carrier mobility with a theoretical limit of 200,000 $cm^2V^{-1}s^{-1}$ (**Figure 2.2**b)[11], half-integer quantum Hall effect[15] and low absorption of only 2.3% visible

light (**Figure 2.2**c)[12]. It is believed that graphene is an ideal candidate for transparent conductors and optoelectronic devices but the lack of the band gap also limits its applications where a semiconductor is preferred.

2.2.2 TMDs

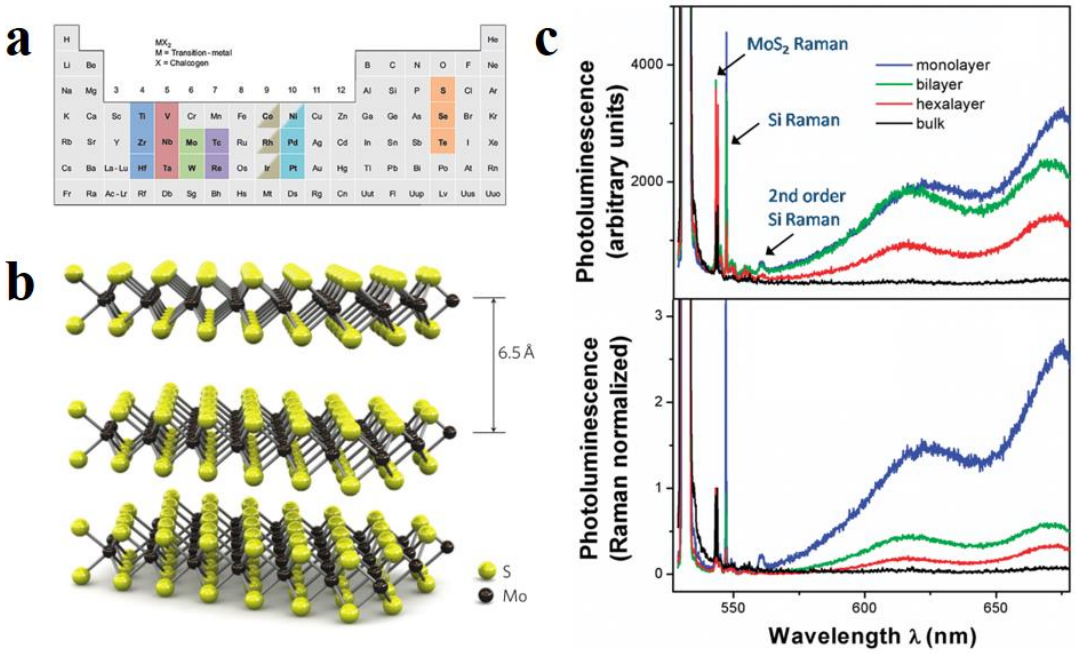


Figure 2.3 Properties of TMDs. (a) Periodic table with highlighted transition-metal and chalcogen elements which can form layered TMDs. Reproduced with permission from Ref 16. Copy right 2013, Nature Publishing Group. (b) Atomic model of layered MoS_2. Reproduced with permission from Ref 17. Copy right 2011, Nature Publishing Group. (c) Photoluminescence in MoS_2 layers with different thickness. After the Raman normalization, there is a strong increase of photoluminescence in monolayer MoS_2. Reproduced with permission from Ref 18. Copy right 2013, American Chemical Society.

As shown in **Figure 2.3**a, TMDs have generalized formula MX_2 where M and X represent a transition-metal from group 4-7 and a chalcogen atom (S, Se or Te), respectively[16]. Each layer of TMDs exists in a sandwich structure (X-M-X) where two atomic layers of chalcogen atoms covalently bonded on each side of a layer of hexagonally packed metal atoms[17,19], as the example of MoS_2 demonstrated in **Figure 2.3**b. Atomically thin TMDs usually exhibit several distinct features due to the

quantum confinement effects[20]. For example, monolayer TMDs (M=W, Mo; X=S, Se) own direct band gaps in the visible spectral region and have the ability to interact with the incident light strongly (**Figure 2.3**c). Additionally, by tuning the illuminated photon energy and handedness[21], one can control the electron spin due to the spin-orbit splitting of a few meV in the conduction band and hundreds of meV in the valence band[22]. All of these features indicate that TMDs have the potential for transistors in electronics or detectors and emitters in optoelectronics[17,18,23,24].

As intriguing building blocks, 2D materials show great possibilities in the optoelectronic devices of the next generation. In research, different 2D materials are often combined together to form heterostructures to obtain superior properties and realize new functions which cannot be achieved in individual ones.

2.3 Preparation Methods of 2D Materials and Heterostructures

2D crystals are produced but usually need to be transferred to another substrate for the device fabrication. Therefore, the preparation of high quality 2D layers in a clean, scalable and cost-efficient way is of great importance for the investigation of novel devices and superior performances. Here, the state-of-the-art preparation methods are overviewed, with a further discussion on their advantages and limitations.

2.3.1 Production

Two types of approaches exist for the production of 2D materials: top-down and bottom-up. The top-down strategy involves reducing the size from the bulk towards the nano scale, whilst the bottom-up route is to grow nanomaterials from atoms and molecules. A selection of some typical methods are described below.

Mechanical exfoliation is the first used method to produce graphene[1]. It has a

simple process where an adhesive tape (scotch-tape) is used to cleave a piece of graphite repeatedly until one or few-layer graphene is obtained. The same method is generally applied for other 2D materials later[6,25,26]. Crystals produced via this method are of high quality, free of defects and dopants. Therefore, it is ideal for the study of intrinsic properties of 2D crystals and some proof-of-concept devices. However, the very limited size it can realize, only up to millimetre scales[27], largely hinders its development in the industry.

Bulk layered materials can be sonicated in solvents to obtain nanosheets in a large amount. This is the so-called liquid exfoliation, which was first reported in 2018[28]. Basically, it involves three steps: dispersion, sonication and purification. Considering 2D sheets are held together by weak van der Waals forces, solvents with high surface tensions/energies (40-50 mJ/m^2 for liquids or 70-80 mJ/m^2 for solid) are thus chosen so that it can overcome the cohesive energy between the 2D adjacent layers[29]. This approach is widely applied in coating, ink-jet printing, making composites, etc. It is effective for high-yield production but lacks the homogeneity in the crystal size. Also, the cost and toxicity of solvents is another problem.

Laser ablation is to remove an entire or partial layer from a materials surface by using a laser beam. The layer thinning or shape patterning of 2D sheets can be realized by tuning the laser energy density[30,31]. Considering the materials may get oxidized during ablation, this process is better performed in a vacuum condition or inert atmosphere[32]. This technique is pretty straightforward but requires more efforts for the precise control.

To solve the drawbacks of these top-down methods, some bottom-up approaches

have been developed. Epitaxial growth is a typical process which usually refers to the graphene growth on SiC[33]. The substrate is insulating and compatible for the industrial fabrication, such as high frequency electronics, radiation hard devices and LEDs. However, one limitation for this technique is that SiC wafers cost much more than Si. Besides, thermal decomposition is not a self-limiting process, and thus the thickness of the growing materials is difficult to control.

According to crystallology, crystal seeding requires the pre-deposition of seeds as the nucleation sites and homoepitaxy templates[34]. These seeds can either be precursors, non-reacting metals (Au, Pt/Ti) or etched holes[35]. These well-defined seeds can better determine the size, phase, density, location and orientation of the crystals. This strategy enables the periodic growth of 2D materials into arrays due to the nucleation sites are pre-designed. Since it requires additional steps, this method is more costly and complicated. In addition, particles tend to aggregate during deposition, making multi-layer regions inevitably.

Compared to the aforementioned methods, chemical vapour deposition (CVD) has more potential in the long term and is considered as one of the most promising techniques to produce large-area 2D materials with relatively high quality in an easy, versatile and low-cost way. Here, focus will be put on the current progress of the direct growth of 2D crystals and their heterostructures via CVD method.

When choosing the precursor, cost, toxicity and availability should all be taken into consideration. Extensive research has been carried out in growing graphene and TMDs respectively. Graphene can be synthesized using a gas mixture of methane (CH_4) and hydrogen (H_2) with different ratios under atmospheric or low pressure. The most

widely used metal substrates are nickel and copper, which act as catalysts. A large percentage of monolayer graphene with high quality can be achieved by well controlling the reaction conditions. As an example shown in **Figure 2.4**a,b, a piece of continuous graphene film with some multilayer islands is synthesized on the copper foil. So far, the most remarkable report on the synthesis of graphene is from Kobayashi et al. who realized a 100-meter-long graphene film with a sheet resistance as low as 150 Ω/sq by roll-to-roll CVD[36].

Figure 2.4c presents a typical schematic of a CVD experimental set-up for TMDs[37]. The growth process usually involves two starting materials to deposit TMDs on SiO_2/Si substrates or other insulating substrates such as quartz and sapphire at high temperature under an inert atmosphere[37,38,39,40,41]. Researchers show that the shape of MoS_2 domains varies from triangular to hexagonal geometries. This is due to the local changes in the Mo:S ratio of precursors which influences the kinetic growth dynamics of edges (**Figure 2.4**d). Extensive studies have been done to synthesize large-area homogeneous domains or continuous films with controllable thickness. To date, the film size of TMDs is still much smaller than that of graphene.

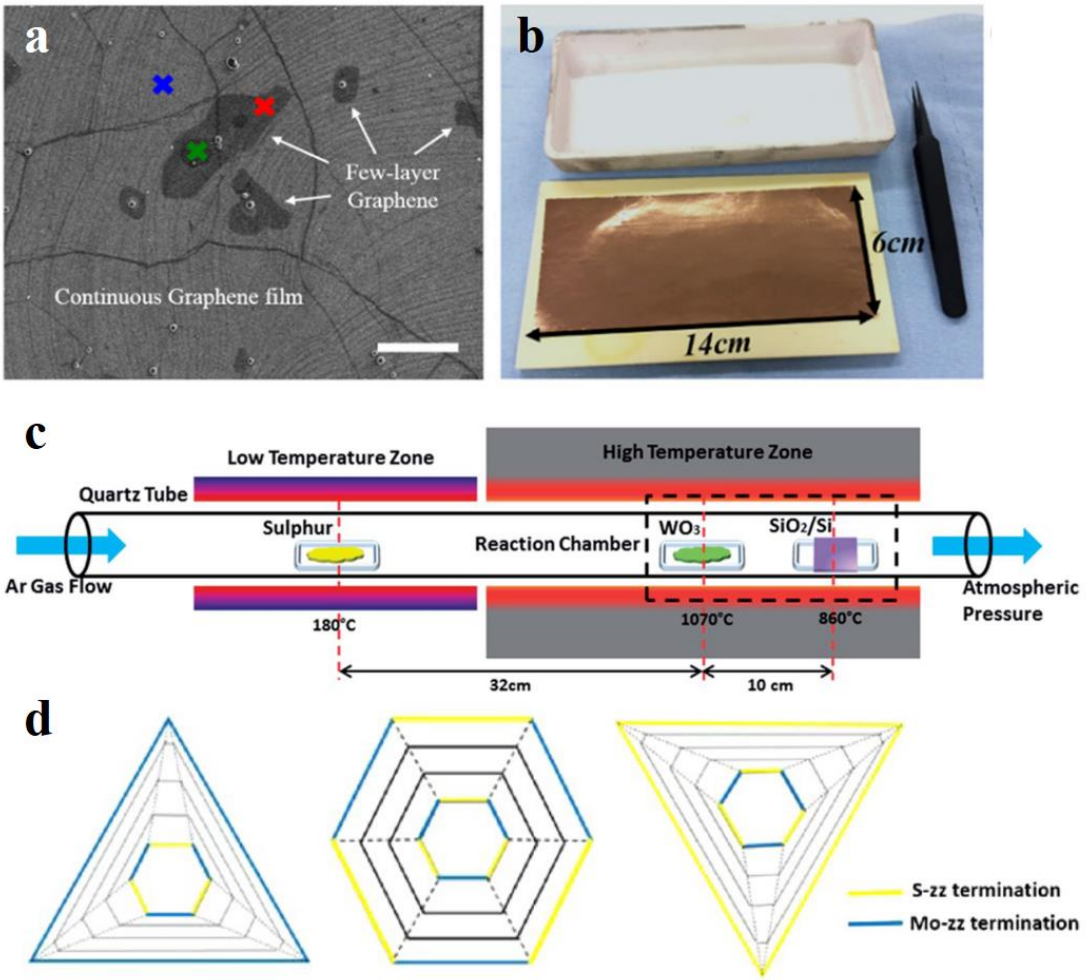


Figure 2.4 CVD synthesis of 2D materials. (a) SEM image showing continuous graphene film transferred from copper to SiO_2/Si substrate. Scale bar: 5 μm. (b) Image of a piece of large-area graphene film growing on the copper foil. (a,b) Reproduced with permission from Ref 42. Copy right 2015, IOP Publishing Ltd. (c) Typical schematic of a CVD experimental set-up with the WS_2 reaction chamber highlighted (black dashed line). Reproduced with permission from Ref 37. Copy right 2014, Royal Society of Chemistry. (d) Schematics showing the shape of MoS_2 domain changes with the growing rates of two different terminations. Reproduced with permission from Ref 38. Copy right 2014, American Chemical Society.

Apart from growing 2D materials individually, more studies have been focused on the synthesis of 2D heterostructures in recent years. It is found that h-BN is a good platform for the growth of other 2D materials. Since the first realization of graphene/h-BN stacks by a manually transfer process, ideas have been inspired for the growth of 2D materials on h-BN directly. Generally, Oshima et al. first indicated the potential of

growing monolayer graphene on monolayer h-BN[43]. Later, the realization of it by CVD without the support of any metal catalysts was first reported by Ding et al. in 2011[44]. Raman results show that the intensity ratio of $2D$ and G varies from 0.56 to 0.79 for samples prepared under different conditions. This indicates that graphene samples obtained are few layered, recognizing h-BN as one of the best candidates for growing graphene. Subsequently, more progress has been made on growing graphene/h-BN stack with an improved quality, including high flatness graphene pads with homogenous diameter[45], graphene domains with maximum size of ~270 nm[46] and the use of consecutive CVD[47]. In spite of all the progress, the investigation for growing large-area graphene/h-BN stacks with a reproducible method is still required with more improved quality.

The lack of dangling bonds and charged impurities also makes h-BN an atomically flat surface for growing TMDs (**Figure 2.5**a,b). For example, Groups in Japan first synthesized WS_2 on exfoliated h-BN flakes directly[48]. By using a 3-furnace CVD apparatus, the supply of each source (WCl_6, sulphur and h-BN/SiO_2) is stable due to the independent control on the supply rate and growth temperature, resulting in an optimum condition of growing the heterostructure. It is also found that there are two different dominant orientation for triangular WS_2 grown on h-BN with a relative angle of 60°. This interesting phenomenon shows that WS_2 crystals and h-BN substrates have a strict relation in the crystallographic orientation. They also determine the growth mechanism as the Frank-van der Merwe which refers to that small 2D nuclei are formed and then grow to large crystals. By utilizing a seeding promoter, Ling et al. show that a relatively low growth temperature (~650 °C) can be employed for growing monolayer MoS_2 on exfoliated h-BN[49]. Various substrates can be used to deposit those

seed molecules on and the seed concentration will make an influence on the growth results. This method can also be applied to grow MoS_2 on graphene. More research focusing on the direct growth on h-BN is summarized in **Table 2.1**.

Table 2.1 Summary of the direct growth on h-BN by CVD process.

Year	Structure	Results	Ref
2011	Gr/h-BN	few layer graphene on powder h-BN single crystal flakes	44
2011	Gr/h-BN	graphene pads on exfoliated h-BN	45
2012	Gr/h-BN	single crystal graphene with maximum size of ~270 nm on exfoliated h-BN single crystal flakes	46
2013	Gr/h-BN	graphene flakes on h-BN flakes through consecutive CVD	47
2014	WS_2/h-BN	triangular-shaped monolayer WS_2 with average size of ~3 μm on exfoliated h-BN flakes with a size of tens of micrometres	48
2014	MoS_2/h-BN	large-area, continuous and high-quality MoS_2 monolayer on exfoliated h-BN using a seeding promoter	49
2015	MoS_2/h-BN	truncated three-point stars monolayer MoS_2 with a flake size ~3 μm on few layer CVD grown h-BN	50
2016	WS_2/h-BN	continuous bilayer-thick film with local monolayer inclusions on h-BN flakes	51
2017	MoS_2/h-BN	submonolayer or fully monolayer MoS_2 films deposited on the full-coverage h-BN/Au	52
2018	Gr/h-BN	AB-stacked bilayer graphene on h-BN/Pt foil	53
2020	Gr/h-BN	vertical heterostructure with graphene at the interface between the h-BN and Cu substrate	54
2021	Gr-h-BN	well-aligned h-BN domains on Ge (110) substrate with graphene laterally grown from the h-BN edge	55

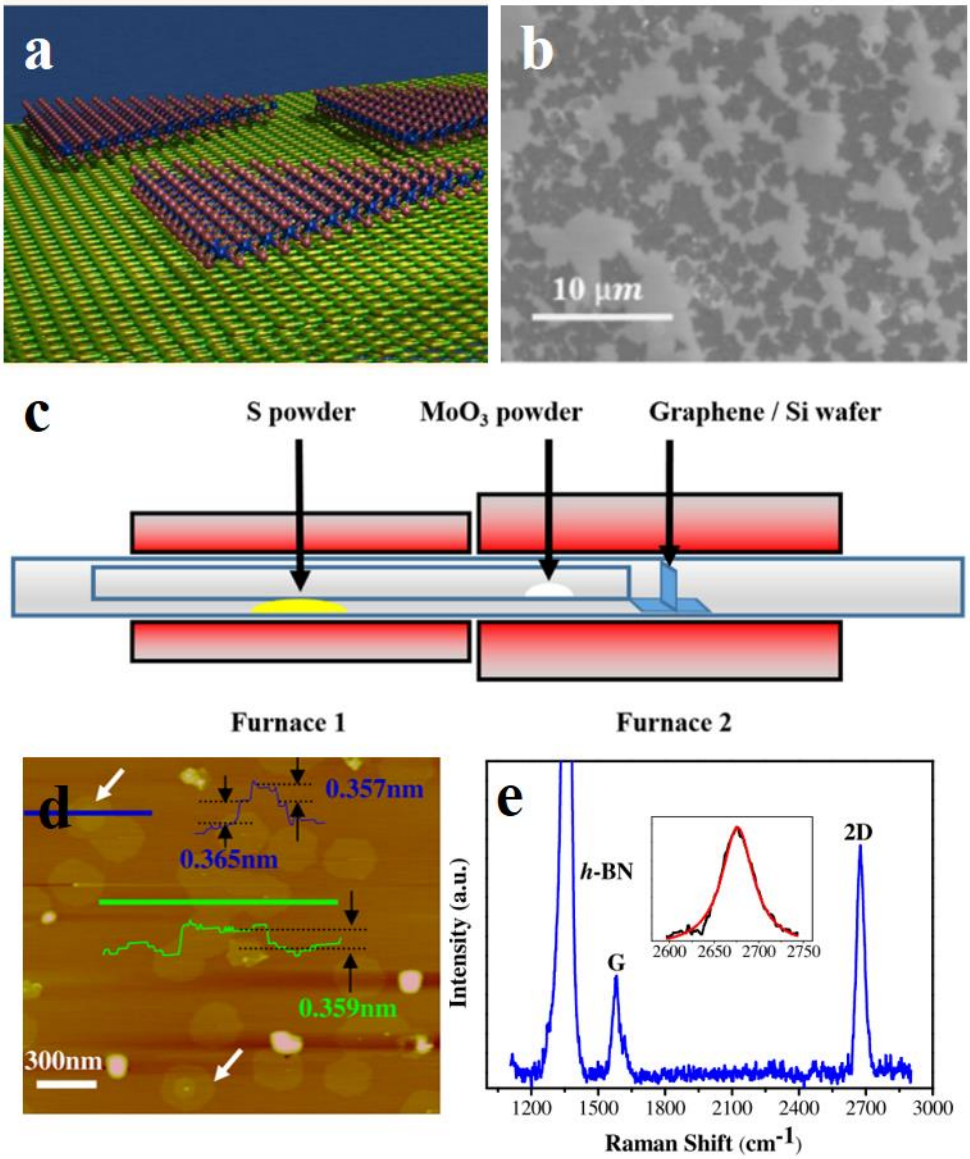


Figure 2.5 Direct CVD synthesis of heterostructures. (a,b) Atomic model and SEM image of MoS_2 domains grown on h-BN film. Reproduced with permission from Ref 50. Copy right 2015, American Chemical Society. (c) Typical schematic of a two-furnace system for growing MoS_2 on graphene. Reproduced with permission from Ref 56. Copy right 2018, American Chemical Society. (d,e) AFM and Raman results showing single crystal graphene domains grown on h-BN flakes. Reproduced with permission from Ref 46. Copy right 2011, Elsevier Ltd.

Graphene is also a promising platform for the growth of other 2D materials, as demonstrated in **Figure 2.5**d,e. Growing TMDs on graphene is particularly interesting because graphene can serve as electrodes which can optimize the interface between TMDs and metals. Shi et al. first reported a method for synthesizing the MoS_2/graphene stack on Cu foil on a growth template with a low temperature of 400 °C[57]. In this work, they use organic solvents for carrying and depositing the precursor onto the surface of graphene. Although a precise control of the MoS_2 layer number is not achieved, it is found that graphene has the potential of serving as an epitaxial substrate for MoS_2 and other hexagonal structured substrates such as h-BN. Robinson's group demonstrates the growth of MoS_2, WSe_2 and h-BN on epitaxial graphene directly[58]. They investigate the important roles of strain, wrinkles and defects on graphene surface which act as nucleation centres for growing TMDs. A subsequent progress is to synthesize centimetre-scale continuous MoS_2 films on graphene with the aid of H_2, reported by Chen et al[56]. SEM results show that MoS_2 can grow into domains and continuous films on graphene without and with H_2, respectively. The addition of H_2 allows the survival of graphene for a longer time during the growth of MoS_2 under a high temperature. More work for growing other 2D materials on graphene has been summarized in **Table 2.2**.

The main advantage of the direct synthesis of heterostructures is that few impurities are introduced during the production. However, the challenges for growing stacks by direct CVD require to develop a technique to increase the domain size and control the grown layer number precisely. Another hot issue is to realize the free synthesis of different 2D heterostructures with unlimited combinations.

Table 2.2 Summary of direct growth on graphene by CVD process.

Year	Structure	Results	Ref
2011	h-BN/Gr	h-BN on mechanically exfoliated graphene	59
2012	MoS_2/Gr	single crystalline hexagonal MoS_2 flakes with a typical lateral size from several hundred nms to several μms	57
2013	h-BN/Gr	h-BN flakes on graphene flakes through consecutive CVD	47
2014	MoS_2/Gr WSe_2/Gr h-BN/Gr	MoS_2, WSe_2 and h-BN on epitaxial graphene	58
2014	MoS_2/Gr	continuous and uniform MoS_2 monolayer films on graphene	60
2016	MoS_2/Gr	centimetre-scale, continuous and uniform films of bilayer MoS_2 on graphene	61
2016	WS_2/Gr	continuous bilayer-thick film with local monolayer inclusions on CVD-grown graphene	51
2018	MoS_2/Gr	centimetre-scale continuous films of MoS_2 monolayer on graphene with the aid of H_2	56
2020	h-BN-Gr	lateral heterostructure with h-BN growing from the edges of the existing graphene islands	54

2.3.2 Transfer and Stacking

In general, there are mainly two basic techniques for transferring individual 2D materials: dry and wet transfer[62]. Their detailed steps are shown in **Figure 2.6.** Plenty of research has been done to optimize the techniques and thus they have become quite mature[63,64,65]. Here, more attention will be focused on transfer techniques for heterostructures.

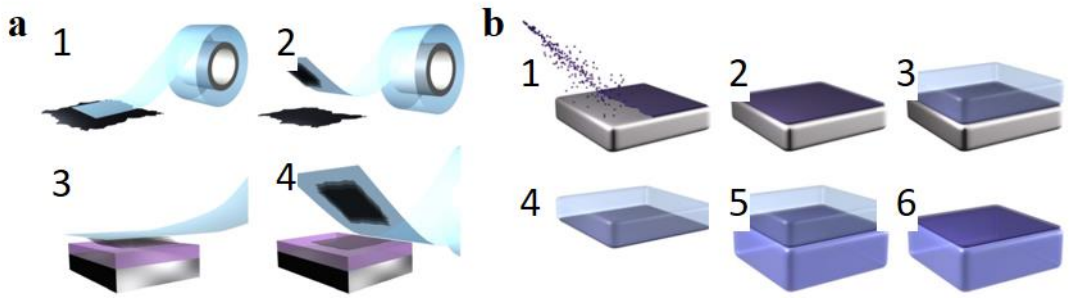


Figure 2.6 Traditional transfer techniques for individual 2D materials. (a) Dry transfer. Step 1: Adhesive tape (scotch tape) is pressed against a 2D material so that the top few layers are attached to the tape. Step 2 and 3: The tape with layers is pressed against a surface of a substrate. Step 4: Upon peeling off, the bottom layer is left on the substrate. (b) Wet transfer. Step 1 and 2: 2D materials are grown on a substrate. Step 3: A sacrificial layer, for example PMMA, is deposited on top of 2D layers. Step 4: The metal is etched away, leaving 2D layers with the sacrificial layer. Step 5: 2D layers with the sacrificial layer are transferred onto the target substrate. Step 6: The sacrificial layer is removed. (a,b) Reproduced with permission from Ref 62. Copy right 2012, IOP Publishing.

The initial motivation for realizing a vertically stacked architecture is to obtain high-quality graphene devices without suspending it. Although graphene has been expected to own giant carrier mobility[11], its actual performance on SiO_2/Si substrates is not satisfying due to many factors, such as scattering from charged impurities[66,67], optical phonons[33,68] and substrate surface roughness[69,70]. To overcome this problem, Dean et al. from Columbia University first reported a deterministic transfer process to produce graphene/h-BN devices[71]. As demonstrated in **Figure 2.7**a, the process involves four steps. First, exfoliated graphene is attached onto a stack consisted of a

PMMA layer, a water-soluble layer and a SiO_2/Si substrate. The sample is then placed on the surface of deionized water. After the fully dissolution of the water-soluble layer, the SiO_2/Si substrate sinks to the bottom of the water bath, leaving the super-hydrophobic PMMA on top of graphene. It is then scooped up by a glass slide which is clamped onto the arm of a micromanipulator of an optical microscope. Meantime, exfoliated h-BN flakes are obtained from high-purity BN single crystals on the SiO_2/Si substrate. By optically adjusting the position of the graphene and h-BN, two materials are aligned and brought into contact. During the process, the sample is heated to 110 °C so that water can be driven off and PMMA will be adhered to the SiO_2/Si surface strongly. Finally, PMMA is removed by acetone. This transfer technique with alignment is considered versatile and has been widely used to make various heterostructures, such as MoS_2/Gr[72,73], MoS_2/h-BN/Gr[74] and h-BN/Gr/h-BN/Gr/h-BN[6]. Later, Zomer et al. developed a similar transfer method using an optical mask consisted of a transparent glass, an adhesive tape with the adhesive side facing the glass and a ~1 μm thick methyl/n-butyl methacrylate co-polymer[75]. By using a mask aligner, graphene flake can be precisely aligned to the target h-BN crystal. The majority of the graphene (typically 95%-100% for an area of 100 μm^2) after transfer is found free of bubbles and wrinkles, which is considered to be a huge improvement.

Wedging transfer is another novel transfer method reported by the group at Delft[76]. Here, the position of graphene towards the target substrate is adjusted by manipulating a probe needle which contacts with the layer, as depicted in **Figure 2.7**b. A syringe pump is used here to move out the water gradually so that the layer can be successfully deposited on the desired position after all the water is pumped out. This method has a notable limitation that the binding between TMDs and SiO_2/Si substrates is quite weak

and thus TMDs will be washed off by water[77]. Therefore, this aqueous transfer method is not suitable for stacking another layer on top of TMDs.

The above methods all aim at exfoliated materials while for CVD-grown materials, stacks can be prepared directly with minimal alignment steps due to a high domain density, making the production yield high[78,79]. As shown in **Figure2.7**c, the Au/Gr electrodes are directly transferred to a SiO_2/Si substrate with TMD domains without alignment. Devices are fabricated by the wafer-scale batch transfer which permits a statistical analysis on the performance of the devices, which cannot be achieved in exfoliated ones.

Despite the above mentioned wet transfer processes, an all-dry method using the viscoelastic stamps is presented by Castellanos-Gomez et al.[80]. Here, they take advantages of the viscoelasticity which means the stamp can slowly flow over long timescales otherwise acts as an elastic solid. After the flake is brought into contact with the target surface in the desired position under the optical microscope, the stamp is slowly peeled off, leaving the flakes on the substrate. This all-dry process allows free of contamination from wet chemicals. It is clean, straightforward for suspended structures and can achieve a high yield (nearly 100% for flat substrates).

The flexible manually transfer method exhibits great freedom in combining different layered materials together and allows us to study the fundamental properties of them. However, some limitations are emerged as well, such as the complicated steps for alignment, contamination at the interface caused by tapes or polymers, bad quality of interlayer binding and low possibility for future scalable production of device arrays.

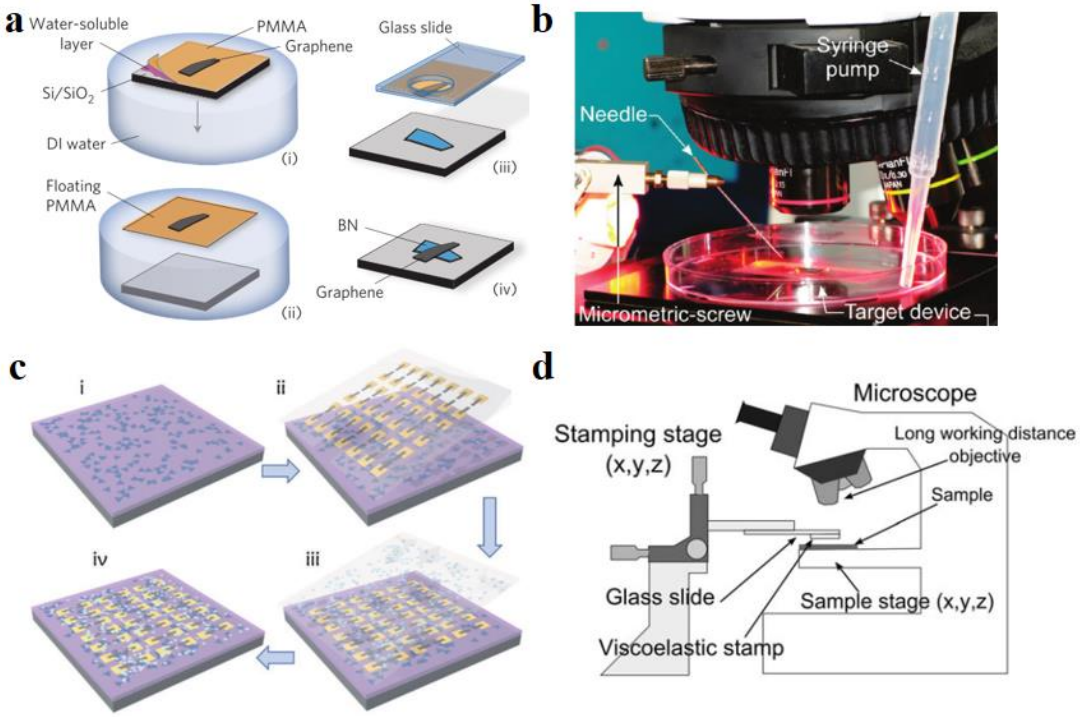


Figure 2.7 Transfer techniques for 2D heterostructures. (a) Schematics of the transfer steps for preparing graphene/h-BN stacks. Reproduced with permission from Ref 71. Copy right 2010, Nature Publishing Group. (b) Experimental setup consisted of a conventional optical microscope with low magnification and a standard needle connected to a micrometric screw for precisely aligning the wedged polymer film (including the graphene pattern) on top of a target substrate. Reproduced with permission from Ref 76. Copy right 2010, American Chemical Society. (c) Schematics showing PMMA film, pre-patterned Cr/Au bond pads and graphene electrodes transferred onto the SiO_2/Si substrate with pre-transferred TMD domains. Reproduced with permission from Ref 78. Copy right 2017, John Wiley & Sons - Books. (d) Schematics of the experimental setup employed for the all-dry transfer process. Reproduced with permission from Ref 80. Copy right 2014, IOP Publishing Ltd.

2.4 Optoelectronics based on 2D Materials

2.4.1 Photodetectors

As an important part of the optoelectronic devices, photodetectors have the feature of converting the absorbed light energy to electrical signals, either photocurrent or photovoltage. In this section, the mechanisms of photodetectors and derive equations for key parameters are listed and elaborated, with typical photodetectors further discussed.

2.4.1.1 Mechanisms

Basically, the photocurrent generation can be driven by two factors: electric field separation of electron–hole pairs and thermal process[81]. The mechanisms of the former one are usually classified as the photoconductive, photogating and photovoltaic effects which are especially relevant for (photo)-field-effect transistors (FETs). For the thermal process, it includes the photo-thermoelectric and bolometric effects.

Electron-Hole Separation

The photoconductive effect relies on the change of electric conductivity of the photoactive material by the photon absorption. Under an applied bias without illumination, a small source–drain current can flow through the device. When illuminated by photons with energy higher than the band gap, electron-hole pairs will be generated and separated by the bias, producing a photocurrent which adds to the dark current.

The photogating effect is a special case of the photoconductive effect. In this case, one or two carrier types (holes for example) generated under illumination is trapped in localized states, usually at defects or the surface of the semiconducting materials. Those trapped charges act as an additional local gate electric field, changing the

resistance of the materials effectively by inducing more charges in the channel. Therefore, this effect is particularly important for 2D photoconductors because of its large surface. Due to the huge difference between the electron and hole mobilities, the electrons will have a much shorter transit time. Consequently, more electrons will be then supplied from the other electrode and circulate many times in the channel during the lifetime of holes to maintain charge neutrality. This means more electrons can contribute to the photocurrent, resulting in a large photogain but a slow response speed. For example, a photogain up to 3.4×10^4 has been reported by Tan et al. by constructing a lateral graphene-contacted vertically stacked WS_2/MoS_2 hybrid photodetector[78]. The illumination horizontally shifts the charge neutrality point (CNP), and the polarity of the trapped charges can be judged by the shift direction. Both photoconductive and photogating can take place in the same device and participate in the photocurrent simultaneously.

The photovoltaic effect is that the separation of electron-hole pairs are created by an intrinsic electrical field, the origin of which could be a p-n junction or a Schottky barrier at the interface between a metal and a semiconductor where there is a great difference in the work functions between materials. Therefore, photodetectors operating by this effect is called photodiodes. They usually display a nonlinear I-V curve (rectifying behaviour) without illumination. When illuminated, there are two modes that the device can function at: the photovoltaic mode (at zero bias) and the photoconductive mode (under bias). In the first mode, electrons and holes separated by the intrinsic electric field are collected at opposite electrodes, generating the open-circuit voltage (V_{oc}) or the short-circuit current (I_{sc}). Devices working in this mode have the lowest dark current, resulting in an enhanced detectivity, maximized linearity

and sensitivity. In the second mode, the separation efficiency of the electron-hole pairs and the response speed will increase as a result of the same direction of the external and internal electric field.

Thermal Process

The photo-thermoelectric effect is based on when there is a temperature difference (ΔT) between two dissimilar conductors or semiconductors caused by non-uniform light-induced heating. This temperature gradient ΔT will make a voltage difference V (photo-thermoelectric voltage) through the thermoelectric effect, defined as

$$V = (S_1 - S_2)\Delta T \qquad (2.1)$$

where S_1 and S_2 are the Seebeck coefficients of the two substances. This voltage will further produce a current through the circuit at zero bias. This effect can only be found in a non-uniform semiconductor and the temperature difference can be achieved by either local illumination[82,83] or global illumination but with distinct absorption coefficients in different parts of a device[84].

Bolometric effect occurs when the resistivity of a material changes owing to uniform heating from the absorption of photon. There are two factors that can determine the magnitude of this effect: the conductance variation of a material with temperature and the homogenous temperature increase from the heat. This effect has been observed in photodetectors based on graphene where electron cool down is limited by the available phonons[85,86].

2.4.1.2 Key Parameters

The photoelectrical performances of a photodetector are usually characterized by the following key parameters.

Photoresponsivity (R, unit: A/W): It can be expressed by the formula

$$R = \frac{I_{photo}}{P_{laser}} \tag{2.2}$$

where I_{photo} is the generated photocurrent and P_{laser} is the incident laser power on the semiconducting device. It is used to measure a photodetector's output photocurrent under a given incident laser power at a certain wavelength.

Quantum efficiency (QE, unit: %): It can be further divided into external quantum efficiency (EQE) and internal quantum efficiency (IQE).

EQE can be expressed as

$$EQE = \frac{I_{photo}/e}{P_{laser}/h\nu} = \frac{Rhc}{e\lambda} \tag{2.3}$$

where e is the elementary charge, h is Planck's constant, ν is the frequency of the incident laser, c is the speed of incident laser and λ is the wavelength of incident laser. EQE is the ratio between the number of electron–hole pairs contributed to the photocurrent and the number of incident photons. Photodetectors with a large EQE require a high optical absorption of the active layer but a minimal of carrier recombination and trapping before collected. For IQE, it is the ratio between the number of electron–hole pairs contributed to the photocurrent and the number of absorbed photons, which can be determined by deducting the photon losses due to transmission and reflection. Additionally, the optical interference effects should be

considered for photodetectors with an ultrathin active layer especially.

Photogain (G): It is the number of detected charge carriers per single incident photon, which are given by

$$G_{ext} = \frac{Rhv}{e} \qquad (2.4)$$

Speed or response time: It describes a photodetector's ability to follow a rapid modulated optical signal. In some cases, it indicates the time needed for a photodetector to go from 10% to 90% of final output. A fast response speed is usually preferred for a photodetector especially in some particular fields, such as video imaging, optical communication, etc.

Bandwidth (Δf): It is the difference between the upper (f_2) and lower (f_1) light modulation frequencies, where the detector has uniform response in this range and no response out of this range, expressed as

$$\Delta f = f_2 - f_1 \qquad (2.5)$$

Noise equivalent power (NEP): It is the amount of laser power needed to generate a signal which is comparable to the noise of the device, defined as

$$NEP = \frac{P_1}{\sqrt{\Delta f}} \qquad (2.6)$$

where P_1 is the incident laser power that produces signal to noise ratio = 1.

Detectivity (D^*, unit: Jones = cm $Hz^{1/2}$ W^{-1}): It characterizes a photodetector's sensitivity with regards to the geometry, bandwidth and noise of the device. It is given by

$$D^* = \frac{R \times (A\Delta f)^{1/2}}{i_n} \quad (2.7)$$

where A is the effective area of the detector and i_n is the noise current.

The noise current can be generated from many sources, such as Johnson–Nyquist noise (thermal noise), shot noise, flicker noise (low frequency $1/f$ noise) and so on. Thermal noise happens regardless of an applied voltage, which is originated by the random thermal motion of charge carriers. Shot noise is induced by the statistical uncertainty of the electron arrival rate, and is particular obvious in semiconductors due to more potential barriers. Flicker noise has a $1/f$ dependence and stems from nonohmic contacts and disorders or edge defects due to the trap states. There have been reports on the measurements of flicker noise in some 2D electronics[87,88,89].

In this thesis, for a rough estimation of the sensitivity, the noise current is assumed to be dominated by shot noise[78,90]. Since shot noise (i_{n_sn}) is a Poisson process, it can be expressed by

$$i_{n_sn} = (2eI_{dark}\Delta f)^{1/2} \quad (2.8)$$

where I_{dark} is the dark current.

Therefore, D* can then be expressed as

$$D^* = \frac{RA^{1/2}}{(2eI_{dark})^{1/2}} \quad (2.9)$$

2.4.1.3 Photodetectors based on 2D materials

Interesting phenomena and exceptional properties are expected for photodetectors based on all-2D materials thanks to their atomic thickness and large surface area. In this part, some typical photodetectors based on 2D materials are illustrated by different categories.

Metal-graphene-metal

With an absorption spectrum covering the entire ultraviolet to far-infrared range, graphene appears to be a promising candidate for ultra-broadband photodetectors.

Past experiments have shown a strong photoresponse near metal/graphene contacts. In 2008, Lee et al. used scanning photocurrent microscopy to investigate the metal contact and sheet edge influence on the photoelectric properties of monolayer graphene[91]. Later, Park et al. from Cornell University applied the same technique to explore further the photocurrent generation and collection in monolayer graphene, displayed in **Figure 2.8**a,b[82]. Results show that the strong electric field generated by the metal-graphene contacts can result in an efficient photocurrent generation (30% efficiency for electron-hole separation). Researchers from IBM find that a p-type graphene transistor could turn into p-n-p channel if the gate bias goes beyond the Dirac point voltage[92]. When this p-n junctions are illuminated, the external responsivity can be as high as 0.001 A/W. Following the progress, displayed in **Figure 2.8**c, this group extended their work where mono- and few-layer graphene is used to realize ultrafast transistor-based photodetectors by an internal field. This kind of novel photodetectors enables zero-dark current operation, good internal quantum efficiency (estimated in the range of 6-16%), very high bandwidth (potentially >500 GHz) light detection and very wide wavelength detection range[93].

Asymmetric metal contacts for source and drain have shown great advantages in terms of decreasing the orders of the dark current and generating the photocurrent. The first use of graphene as the active layer of a photodetector was reported by the same group from IBM in 2010[94]. In the previous work, due to the lack of a high electric field in the bulk graphene sheet, carrier recombination is always happened before generating the external current. Here, a strong electric field is created by utilizing multiple, interdigitated and asymmetric metal fingers. The responsivity goes up to 6.1 mA/W, representing a 15-fold improvement over the past reported results. Since graphene grown by CVD inevitably has more intrinsic defects than mechanically exfoliated ones, it is necessary to explore the asymmetric work function scheme for the photodetectors based on CVD-grown graphene. As presented in **Figure 2.8**d, Yoo et al. fabricated the device using a various combination of Au, Pd and Ti. The difference of work functions for the Au−Ti is 0.34 eV while that for the Au−Pd is 0.15 eV. With these asymmetric source and drain metal contacts, it is possible for a photodetector based on CVD graphene to operate under the zero-bias[95]. Moreover, for the Au−Ti case, its photoresponsivity is ~63 times higher than that with a symmetric Au-Au contact combination (0.82 mA/W). This is achieved by using metals with different work functions which generates a gradient in the Fermi level of the graphene channel. Due to this intrinsic potential, the carriers can be more efficiently collected with the asymmetric metal contacts.

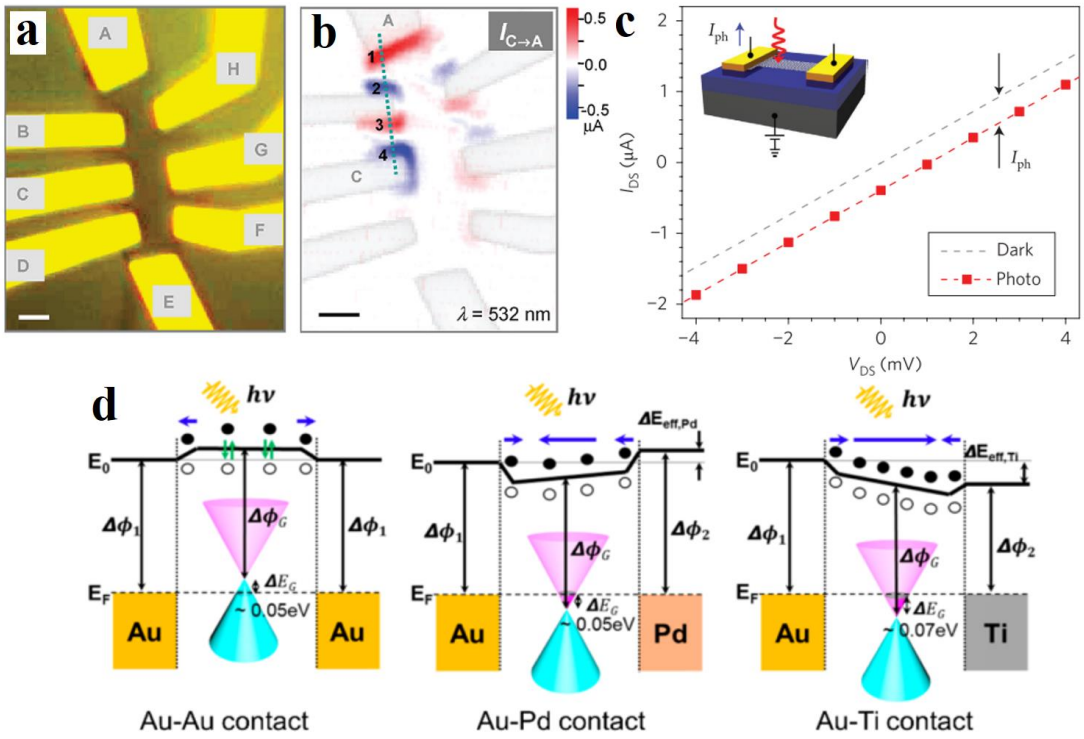


Figure 2.8 Graphene-based photodetectors. (a) Optical image of the graphene photodetector contacted by eight Cr/Au electrodes. Scale bar: 2 μm. (b) Corresponding photocurrent image of the device in (a). Scale bar: 4 μm. (a,b) Reproduced with permission from Ref 82. Copy right 2009, American Chemical Society. (c) Output I_{ds}-V_{ds} curves of the graphene photodetector with and without illumination. Inset: Schematics of the graphene device. Reproduced with permission from Ref 93. Copy right 2009, Nature Publishing Group. (d) Band diagrams of graphene photodetectors with different source/drain metal combinations. Δϕ1 and Δϕ2 are the work functions of Au and Pd (Ti) respectively. E_0 is the vacuum level and E_F is the Fermi level of the metal and graphene. ΔE_G represents the doping state of the graphene channel. The black-filled (empty) dots are electrons (holes) generated by the light absorption. ΔE_{eff} is the difference in the effective work functions of the metals used for source and drain. Reproduced with permission from Ref 95. Copy right 2018, American Chemical Society.

Metal-TMDs-metal

Compared with graphene, TMDs based photodetectors usually exhibit better performance mainly due to the slower electron-hole recombination caused by the inherent property of the semiconductor bandgap and carrier transfer.

Researches on the MoS_2-based photodetectors are illustrated here as an example.

Monolayer MoS_2 owns a band gap of 1.8 eV, which corresponds to ~680 nm wavelength[26] (**Figure 2.9**d). For the first time, Yin et al. fabricated monolayer MoS_2 photodetector and studied its optoelectronic performance, as demonstrated in **Figure 2.9**a-c[25]. Compared to the previous reported MoS_2 FETs, the device shows a higher photoresponsivity (7.5 mA/W under an illumination of 80 μW and a gate voltage of 50 V) and ON/OFF ratio (~10^3). It also indicates that the thermal annealing treatment before the measurement will help remove the photoresist residue and improve the contact. In the same year, Groups in Korea further explored multilayer MoS_2 photodetectors which show a wide spectral response from ultraviolet to infrared and a higher photoresponsivity (0.1 A/W) compared to its monolayer counterparts[96]. A 50-nm-thick Al_2O_3 gate insulator is deposited on top of the SiO_2 prior to decrease power consumption due to the increased gate capacitance and dielectric screening of Coulomb scattering[97]. Later, an ultrasensitive photodetector with a photoresponsivity of 880 A/W was reported by Lopez-Sanchez et al[26]. This large improvement is due to the increased mobility, the contact quality and positioning technique.

Different environments can have huge influences on materials that are critical to the performance of photodetectors. As shown in **Figure 2.9**e,f, Zhang et al. fabricated photodetectors using CVD-grown MoS_2 at room temperature in a high vacuum[98]. The device owns superior performances, reaching a high photoresponsivity and photogain of 2200 A/W and 5000, respectively. This study indicates that the air adsorption can cause a p-doping effect on the device, leading to the increase of the hysteresis, the decrease of the mobility and the change in output characteristics. Another common way to avoid the adsorbates in air is by encapsulating the device with h-BN, hafnium oxide, etc[90,99,100].

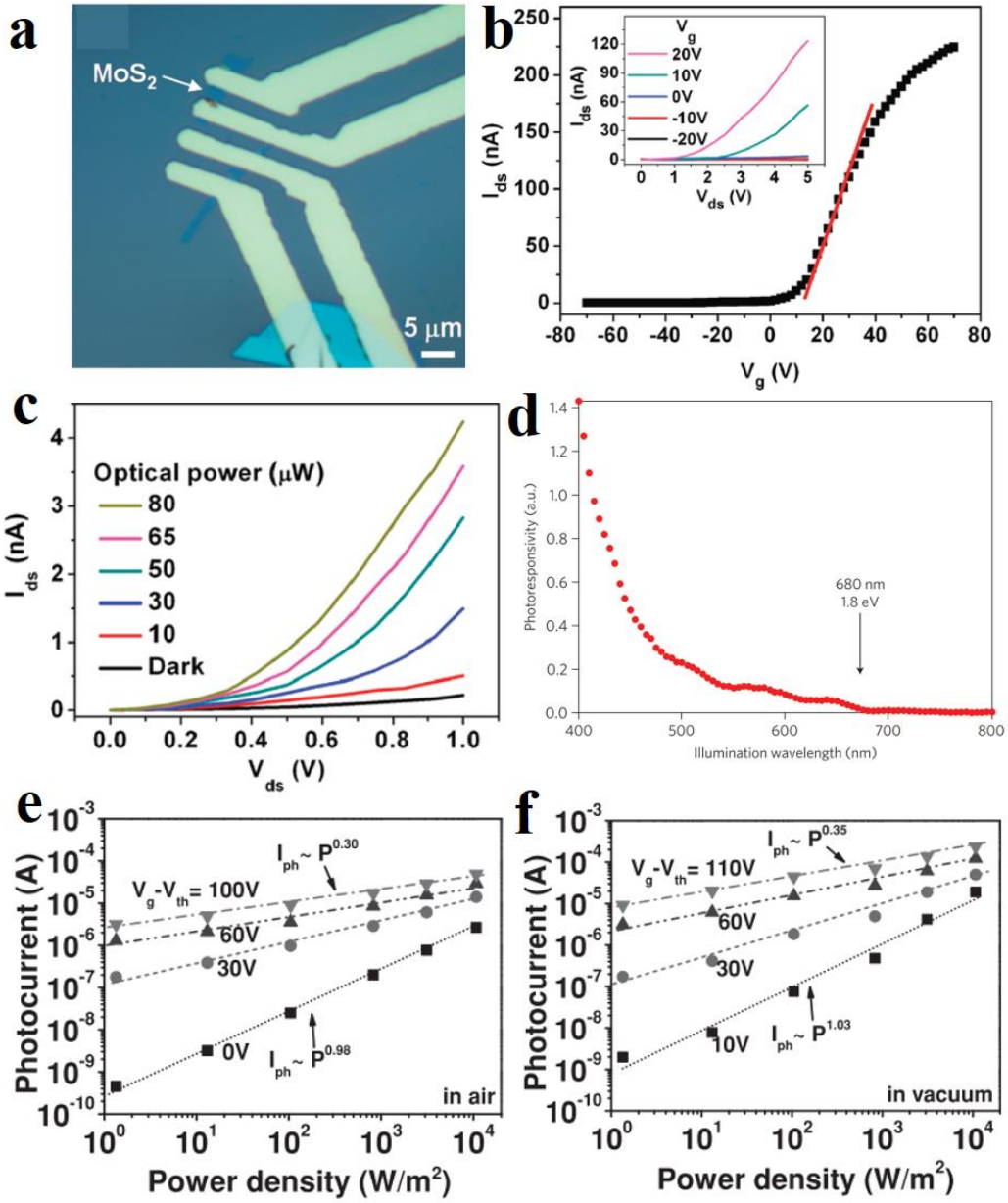


Figure 2.9 MoS_2-based photodetectors. (a) Optical image of a monolayer MoS_2 device. (b) Output I_{ds}-V_g curve of monolayer MoS_2 device under a bias voltage of 3 V. The red line is for the channel mobility calculation. Inset: Output I_{ds}-V_{ds} at different gate voltages. The device exhibits an N-type semiconducting behaviour. (c) Output I_{ds}-V_g curve of the same MoS_2 device under different illumination powers. (a-c) Reproduced with permission from Ref 25. Copy right 2012, American Chemical Society. (d) Photoresponsivity of another monolayer MoS_2 device as a function of illumination wavelength. Laser wavelengths with energies beyond the band gap of MoS_2 can generate electron-hole pairs. Reproduced with permission from Ref 26. Copy right 2013, Nature Publishing Group. (e,f) Power density dependence of the photocurrent in air and vacuum respectively. Reproduced with permission from Ref 98. Copy right 2013, John Wiley & Sons - Books.

In addition to the individual 2D materials, more special phenomena and unusual performances have been found in some heterojunctions that surpass their individual constituents. When stacked together, TMDs with type-II band alignment are particularly interesting as photocarriers generated in this kind of heterojunction can separate efficiently, with an ultrafast speed within 50 fs[101]. Moreover, owing to the intrinsic electric field at the interface of the heterojunction, this kind of heterostructure has the potential for a self-driven photodetector with no source-drain bias. As shown in **Figure 2.10**a-d, vertical and planar transistors based on multilayer MoS_2 and WS_2 heterostructure were demonstrated by Huo et al[102]. With an unusual rectifying and bipolar behaviour, the vertical transistor can serve as a self-driven photodetector with a photo-switching ratio exceeding 10^3 due to the existence of an intrinsic potential. As for the planar device, it also owns a high electron mobility of 65 cm^2/Vs and a photoresponsivity of 1.42 A/W. Following this success, Xue et al. reported a two-step CVD approach method for synthesizing few-layer MoS_2 and WS_2 heterojunction arrays in a scalable production[103]. Raman and photoluminescence (PL) were performed to evaluate the vibrational properties and the thickness, as presented in **Figure 2.10**e,f. For MoS_2/WS_2 heterojunction, there is no change of the positions of $^1E_{2g}$ and A_{1g} phonon modes in Raman compared with those of individual ones, suggesting no obvious affect from the long-range Coulomb interactions between the effective charges. As for PL, a blue shift to 623 nm of the dominant peak of the heterojunction is observed because of the band bending and its influence on each other. Additionally, the MoS_2/WS_2 heterojunction has a much lower PL intensity compared

to that of the individual ones. Further evaluation on the optoelectronic properties of the heterostructure shows a high photoresponsivity of 2.3 A/W.

In addition to the TMDs mentioned above, there are many other TMDs explored for photodetection, including group IVB metal (Hf), VIIB metal (Re), IIIA metal (Ga, In), IVA metal (Ge, Sn) chalcogenides, group IVB metal (Ti, Zr, Ha) trichalcogenides and ternary metal chalcogenides. They are not listed here due to the length reason. More relevant research on the metal-TMDs-metal structure has been summarized in **Table 2.3**.

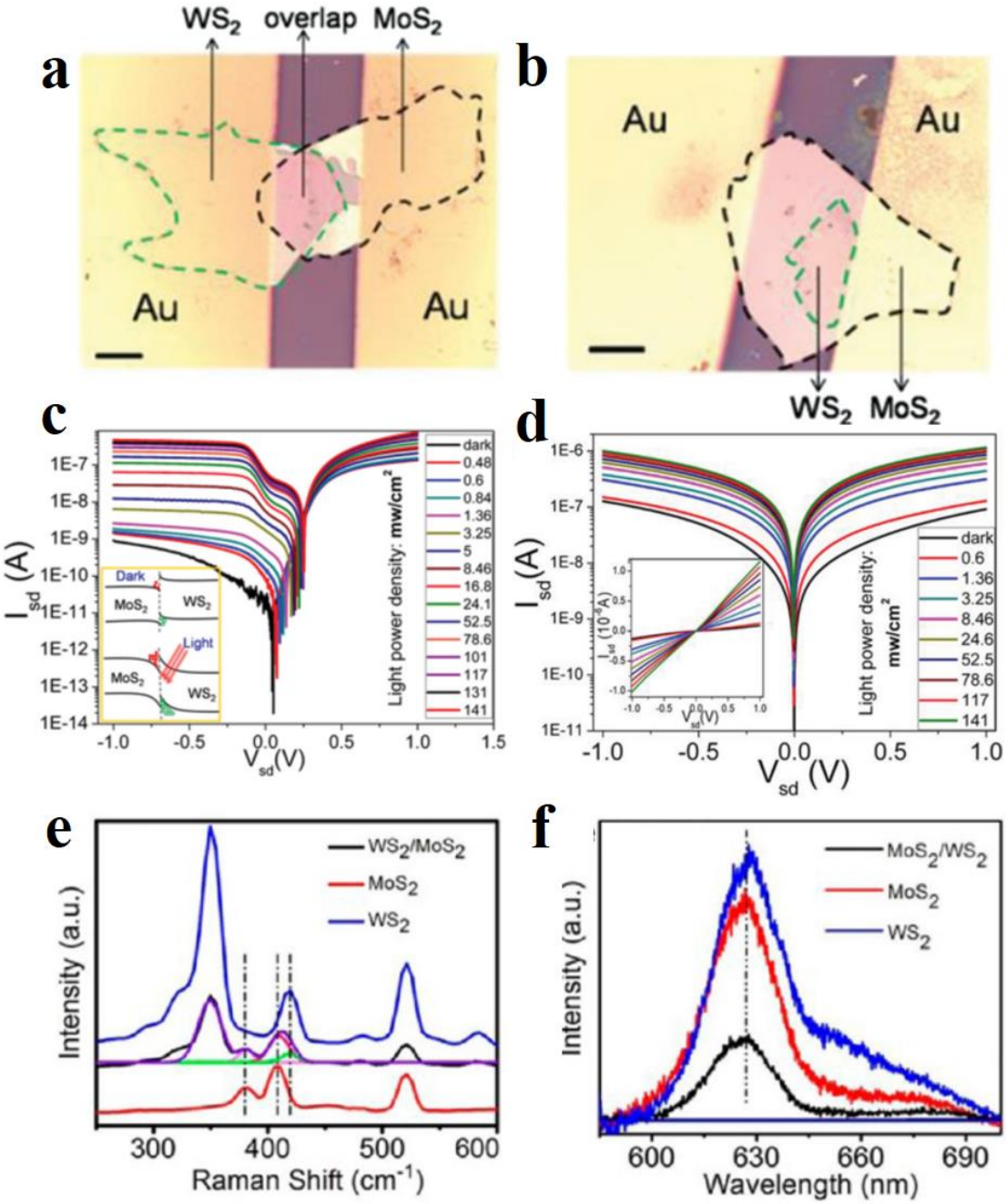


Figure 2.10 TMDs heterojunction-based photodetectors. (a,b) Optical images of the vertical and planar stacked multilayer MoS_2/WS_2 heterostructure transistors. Scale bar: 10 μm. (c) Output I_{ds}-V_{ds} curves of the vertical device with increasing incident power densities. Inset: corresponding band diagrams under dark and light illumination. (d) Output I_{ds}-V_{ds} curves of the planar device with increasing incident power densities. Inset: corresponding data plotted in linear scale. (a-d) Reproduced with permission from Ref 102. Copy right 2014, John Wiley & Sons - Books. (e,f) Raman and PL spectra of WS_2, MoS_2 and their vertical heterojunction. Reproduced with permission from Ref 103. Copy right 2016, American Chemical Society.

Table 2.3 Performance of photodetectors based on TMDs. 1L: 1 layer; 2L: 2 layers; ML: multilayer; FL: few layers.

Materials	Layer number	Year	R [A/W]	Response times [ms]	Ref
MoS_2	1L	2012	0.0075	50	25
	ML	2012	0.1	-	96
	FL	2013	0.57	0.11	104
	1L	2013	880	600	26
	1L	2013	2200	-	98
	1L	2014	0.0011	-	105
	ML	2015	342.6	-	106
	1L 2L	2015	10000	10	107
	FL	2015	2570	1.8	108
	FL	2015	5750	-	109
$MoSe_2$	FL	2014	97.1	15	110
	1L	2014	0.013	60	111
	ML	2015	93.7	400	112
WS_2	FL	2013	0.000092	5.3	113
	ML	2015	884	-	114
	1L	2015	0.0188	-	115
WSe_2	1L	2014	180000	<23	116
	1L	2015	1.1	-	117
MoS_2/ WS_2	ML/ML	2014	1.42	-	102
	FL/FL	2016	2.3	-	103

Graphene-TMDs-Graphene and Graphene/TMDs/Graphene

There are mainly two configurations that are often investigated: (1) lateral structure graphene-TMDs-graphene, where TMDs cover the gap between two graphene ribbons, and (2) vertical structure graphene/TMDs/graphene, where TMDs are sandwiched between two graphene ribbons. Lateral or vertical integration of 2D materials formed by stacking up different 2D materials paves a new way to design novel electronic and optoelectronic devices, where semimetal graphene with a tunable work function serves as contact electrodes and TMDs as the active absorbing channel in photodetectors.

For the lateral structure, graphene is employed to serve as a medium between the conventional metal electrodes and semiconductors, which helps eliminate the Fermi level pinning at the interface. Also, the Fermi level of graphene can be easily tuned due to its finite density of states. For example, **Figure 2.11** shows a typical lateral stack using all CVD-grown 2D materials proposed by Tan et al[78,118]. In this paper, they show how the gate, laser power, layer number and channel length can influence the performance in a lateral-stacked photodetector. The physical mechanism that contributes to the photocurrent generation in this configuration is the photogating effect. Upon the illumination, electron-hole pairs generate, with electrons transferred to graphene while holes residing in WS_2. This cause a rise in the Fermi level of graphene, resulting in a lowered Schottky barrier height of graphene and WS_2. Moreover, by exploiting a lateral graphene-contacted vertically stacked WS_2/MoS_2 device, the photoresponsivity is improved by over an order of magnitude compared with bilayer photodetectors and two orders of magnitude compared with monolayer photodetectors of WS_2 and MoS_2. This significant improvement is explained by the

strong Coulomb interaction between the heterobilayer.

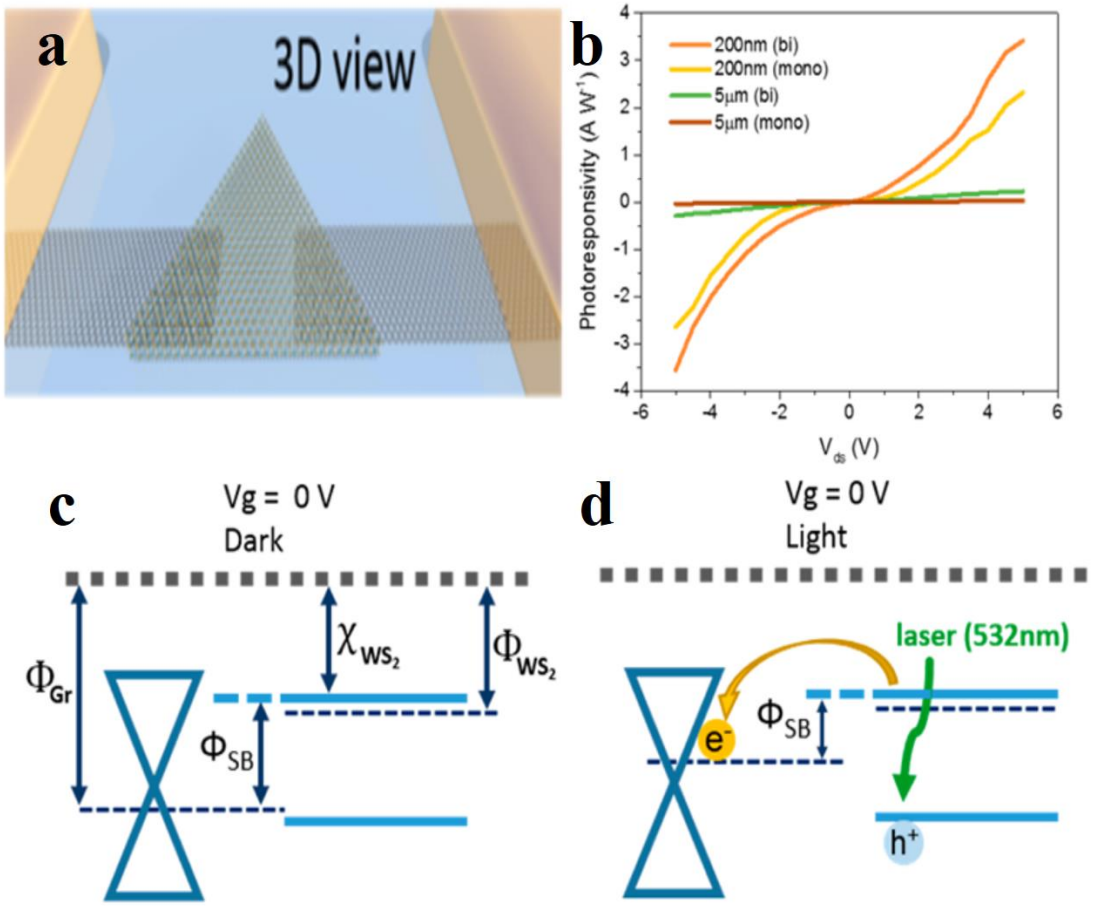


Figure 2.11 Photodetectors based on the Gr-TMDs-Gr configuration. (a) Schematic 3D view of the Gr-WS_2-Gr photodetector. (b) Photoresponsivity of different types of devices under an incident light density of 3.8×10^6 mW/cm^2. (c,d) Band diagrams of Gr-WS_2 heterojunction under dark condition and illumination. Φ_{Gr}: work function of graphene. χ_{WS2}: electron affinity of WS_2. (a-d) Reproduced with permission from Ref 118. Copy right 2016, American Chemical Society.

Compared with the lateral one, Gr/TMDs/Gr vertical structure offers a large surface contact area and short carrier transportation distance, leading to an ultrafast charge-transfer rate[101,119]. In addition, graphene only absorbs 2.3% of visible light, which means stacking it on the semiconducting layer will not block much light passing through it[12]. Therefore, a high photodetecting efficiency can be obtained, which is ideal for the photosensing applications. The physical mechanism that contributes to the

photocurrent generation is the photovoltaic effect, where a built-in potential is formed by creating different tunnelling barrier heights between the top and bottom graphene electrodes.

For example, **Figure 2.12**a-c demonstrates a typical vertical stack proposed by Britnell et al where semiconducting WS_2 is sandwiched between two graphene ribbons[6]. This structure is found to exist strong light-matter interactions, resulting in large photon absorption and photocurrent production. In the idealized condition, the electron-hole pairs generated in TMDs have no favorred diffusion direction thanks to the symmetric structure and hence no photocurrent is measured. However, due to a difference in the initial doping between the top and bottom graphene, an intrinsic electric field across the TMDs is created and the electron-hole pairs are separated, generating the photocurrent. Later, Zhou et al. studied the same structure by using all CVD-grown 2D materials[79]. The large number of devices realized a statistical analysis of the performance of the device. As shown in **Figure 2.12**d, they show Gr/WS_2(2L)/Gr exihibits a huge improvement in photovoltaic response compared with the monolayer ones. This is explained by the long inter- and intralayer exciton lifetimes and the small exciton binding energy in bilayer WS_2. However, keeping increasing the layer number of TMDs will not always lead to an increasing photoresponse. Yu et al. investigated the influence of the TMDs layer number towards the performance of the graphene/TMDs/graphene devices[120], as displayed in **Figure 2.12**e-g. They show that photodetectors of one-layer MoS_2 have remarkably seven times higher photoresponsivity than seven-layer MoS_2. Spectral-dependent studies further indicate that the internal quantum efficiency in monolayer MoS_2 can be as high as 65%, far better than the 7% in seven-layer MoS_2, which is due to the reduced charge seperation

in bulk MoS_2.

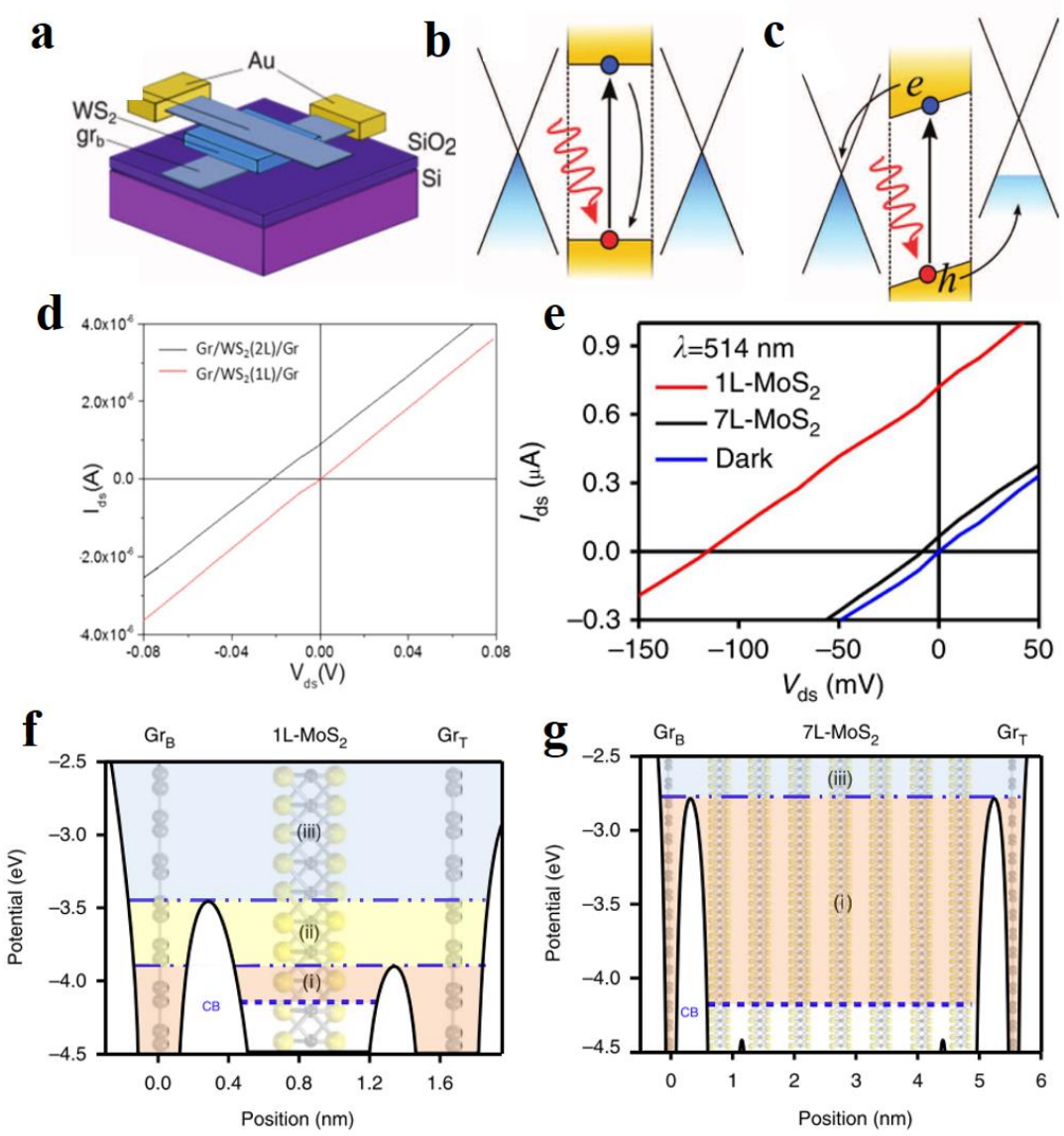


Figure 2.12 Photodetectors based on the Gr/TMDs/Gr configuration. (a) Schematics of a typical graphene/WS_2/graphene device. (b,c) Band diagrams for the heterostructure without and with a built-in electric field to separate the generated electron-hole pairs. (a-c) Reproduced with permission from Ref 6. Copy right 2013, The Author(s). (d) Output I_{ds}-V_{ds} curves of Gr/WS_2 (1L)/Gr and Gr/WS_2 (2L)/Gr vertical devices under 532 nm illumination. Reproduced with permission from Ref 79. Copy right 2018, American Chemical Society. (e) Output I_{ds}-V_{ds} curves of Gr/MoS_2 (1L)/Gr and Gr/MoS_2 (7L)/Gr vertical devices under 514 nm illumination and dark condition. (f,g) Schematics of Gr/MoS_2 (1L)/Gr and Gr/MoS_2 (7L)/Gr vertical devices. (e-g) Reproduced with permission from Ref 120. Copy right 2016, The Author(s).

2.4.2 Electroluminescent Devices

As another important part of the optoelectronic devices, electroluminescent devices have the feature of converting the electrical energy to the light energy by emitting light. In this section, the mechanisms of EL and calculation equations for key parameters are listed, with typical electroluminescent devices further discussed.

2.4.2.1 Mechanisms

Understanding the mechanisms of carrier injections and transport in electroluminescent devices is of great importance for the structure design as well as the device performance. **Figure 2.13** summarizes six typical structures of the electroluminescent devices reported so far with their corresponding band diagrams illustrating the mechanisms[121].

P-n junction is the simplest structure to obtain EL where emission is induced by the bipolar carrier injection. This is achieved by controlled doping or selecting naturally p- or n- type 2D materials. The main challenge of this structure is the low density of holes in the p-type materials.

Quantum well (QW) structure is consisted of an emissive layer sandwiched by tunnelling barriers and electrodes. It has a typical form of Gr/h-BN/TMD/h-BN/Gr where the bias is applied between the graphene. Electrons and holes are recombined in the TMD layer by the tunnelling effect. Here, h-BN is used to help confine the carriers while assuring the efficient injection. This structure owns the benefit of reducing the undesirable dissociation of excitons and leakage current.

Metal–insulator–semiconductor or semiconductor–insulator–semiconductor structure requires the injection of minority carriers into the semiconducting layer. The

injection of holes to the electron-rich semiconductor is effective because the holes have a high probability to form excitons upon the recombination.

Impact excitation generates excitons in a high field regime, where electrons and holes recombine and produce EL.

Thermal emission is due to the local heat caused by the high current passing through the sample. The emission occurs in the region that the heat dissipates most unproductively. Therefore, this is a low-efficient process because of the mass thermal losses.

Interlayer exciton is resided in a hetero-bilayer where the electrons and holes in the adjacent layers recombine and give emission. It is formed when two or more 2D semiconducting layers are stacked and electrons/holes in the different layers are bound by Coulomb interaction across the van der Waals gap. The interlayer exciton owns a longer lifetime because it is spatially indirect if compared to the intralayer exciton.

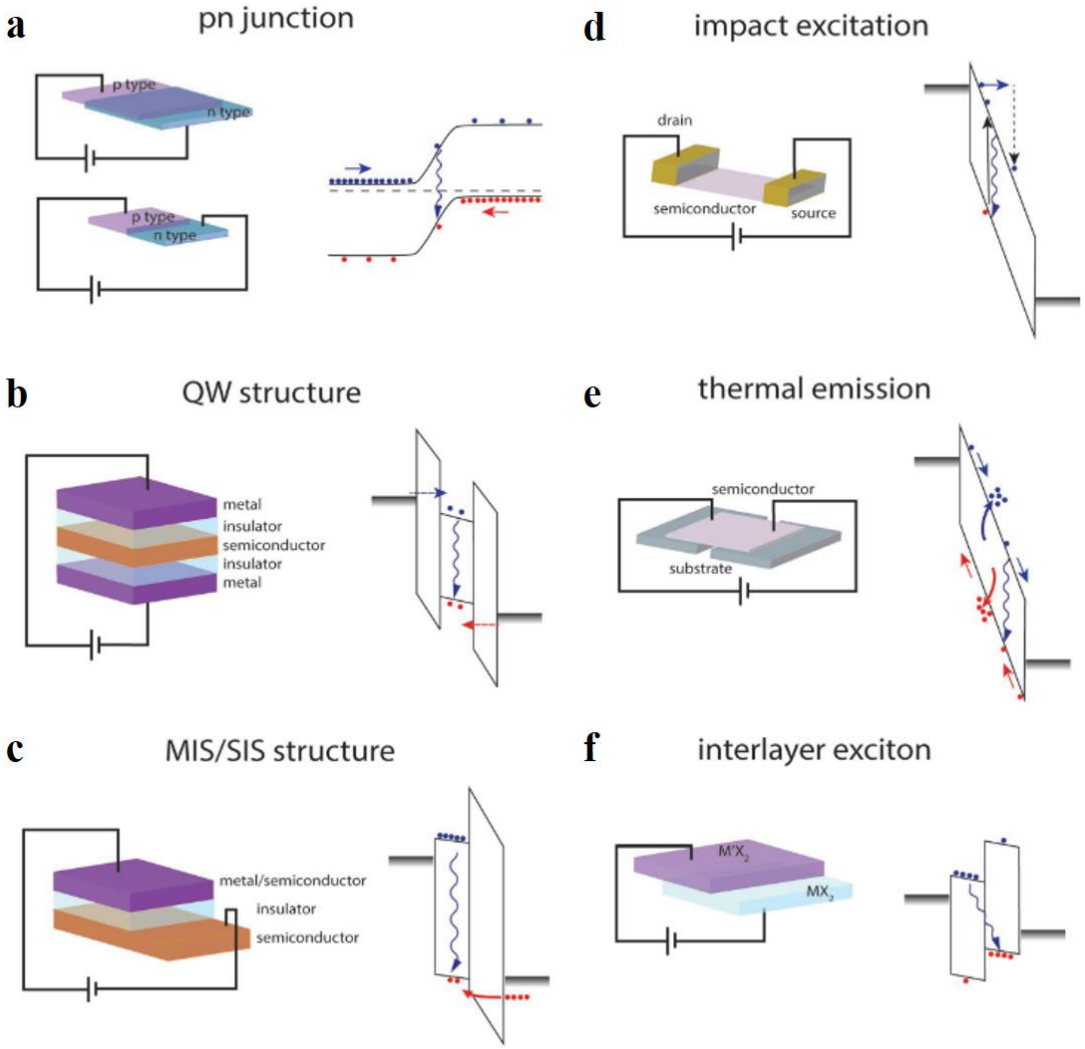


Figure 2.13 Basic structures of electroluminescent devices and their emission mechanisms. Reproduced with permission from Ref 121. Copy right 2018, John Wiley & Sons -Books.

2.4.2.2 Key Parameter

Quantum efficiency (QE) is the foremost parameter for electroluminescent devices. It is defined as:

$$QE = \frac{N_{Photons}}{N_{Carriers}} \qquad (2.10)$$

where $N_{Photons}$ is the number of photons emitted and $N_{carriers}$ is the number of carriers injected into the active semiconducting layer.

In most cases, we can simplify the process by assuming that the internal loss or gain mechanism during the thermalization of injected carriers is neglectable and thus the emission is only caused by the ground excitons. Then the QE is mainly determined by α, the ratio of the number of excitons formed per each injected carrier, and γ, the quantum efficiency of the radiative recombination for ground excitons.

To optimize α is to increase the probability of injected carriers to form an exciton within the active layer. Either different injection rates of electrons and holes or short transient time for carriers to form excitons will be harmful to the device performance. Therefore, it is essential to control the thickness of the barrier layers. If the barrier layer is too thin, it will not enable the injected carriers to remain localized in the active layer and recombine for emission. If the barrier layer is too thick, the carriers will not be able to tunnel through and get emission. A suitable thickness of h-BN is 3-5 layers in electroluminescent devices[122,123].

To optimize γ, the control of the interface quality is essential. It has been reported that encapsulation by h-BN and chemical passivation using a super acid are both effective in enhancing the device performance[124,125,126].

2.4.2.3 Electroluminescent Devices based on 2D Materials

Conventional Electroluminescent Devices

Here, some conventional electroluminescent devices with their characteristics are listed. Jo et al. compared the EL signal of mono-, bilayer and bulk WS_2 light-emitting transistors where the WS_2 in monolayer gives the strongest emission (**Figure 2.14**a)[127]. This indicates that materials in the 2D form allow new optoelectronic functionalities

that do not exist in their bulk form. Besides, as shown in **Figure 2.14**b,c**,** by creating a p-n junction with a p-typed WSe_2 and an n-typed MoS_2, prominent EL can be observed with peaks fitted using multiple Gaussian functions[128]. This reveals deep insights about electron−orbital interaction in TMD-based materials.

Electroluminescent devices using CVD-grown materials have also been constructed. This allows a statistically robust analysis on the performance variations of devices. As demonstrated in **Figure 2.14**d, Sheng et al. fabricated devices in the QW structure (Gr/h-BN/WS_2/h-BN/Au) and showed their performance variations in PL and EL[122]. The stability of the devices is further tested by operating the device under a negative bias of 7 V, switched on and off over several cycles (**Figure 2.14**e). The standard deviation of the EL intensity is calculated to be ~12%, indicating rather standard performances. As for the durability, Hou et al. have shown a long-lived persistent EL in a vertical QW structure (Gr/h-BN/WS_2/h-BN/Gr) for more than 2 h without apparent degradation of WS_2 under a high bias condition of 20 V, shown in **Figure 2.14**f,g[123]. This study shows that CVD-grown 2D materials are promising in the EL devices with long-lived requirements.

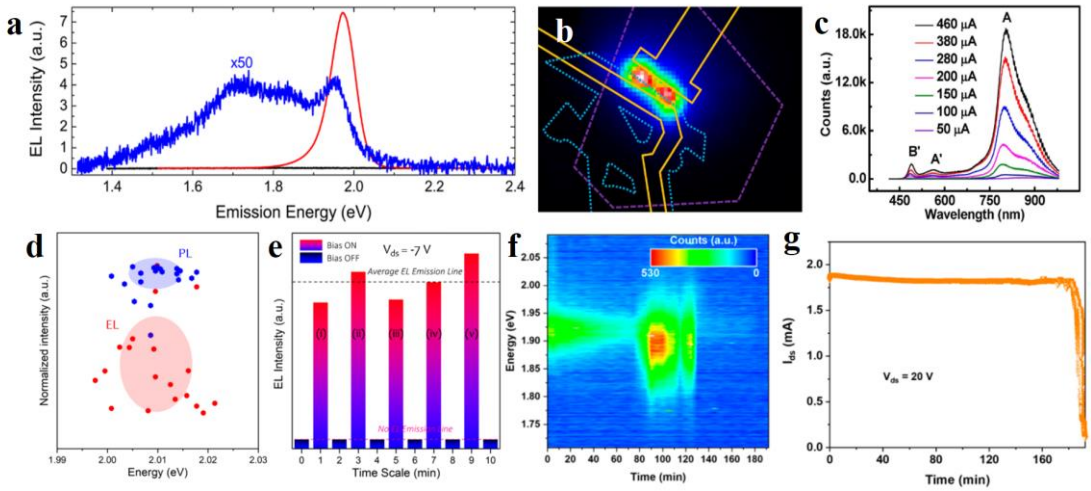


Figure 2.14 Conventional electroluminescent devices based on 2D materials. (a) EL intensities of monolayer (red), bilayer (blue) and bulk (black) WS_2. Reproduced with permission from Ref 127. Copy right 2014, American Chemical Society. (b) EL image in false colour of the heterojunction device under an injection current of 100 μA. (c) EL spectra of the WSe_2/MoS_2 heterojunction under different injection currents. (b,c) Reproduced with permission from Ref 128. Copy right 2014, American Chemical Society. (d) Statistic results of the PL and EL of WS_2-based LEDs. (e) Transient EL intensities of the WS_2-based device under a negative switch-on bias (−7 V) and zero bias. (d,e) Reproduced with permission from Ref 122. Copy right 2019, American Chemical Society. (f) Durability test for a typical WS_2-based device under a fixed bias of 20 V. (g) Corresponding I−t curve of the device in (f). (f,g) Reproduced with permission from Ref 123. Copy right 2020, American Chemical Society.

Novel Electroluminescent Devices

To further promote the device performance, researchers have explored many ways in terms of the material selection, structure design, operation mode and integration with other photonics. Here, some novel electroluminescent devices are introduced and discussed. In 2015, Withers et al. reported an LED using multiple QWs[129], illustrated in **Figure 2.15**a-d. Compared with the device based on a single QW which owns a QE of more than 1%, there is a significant improvement in the structure of multiple QWs, with the best QE up to 8.4%. This research indicates that the probability of the generation of the electron-hole pairs can be enhanced by increasing the time that carriers transport in the active layer. Another way to improve

the EL emission is by utilizing the interlayer excitons[130,131,132], shown in **Figure 2.15** e,f. Interlayer excitons can be formed when two or more semiconductors are stacked together and electrons/holes reside in the adjacent layers are bound by Coulomb interaction across the van der Waals gap. They usually have long lifetimes and the dipoles orient in the out-of-plane direction allows the external electric field to control.

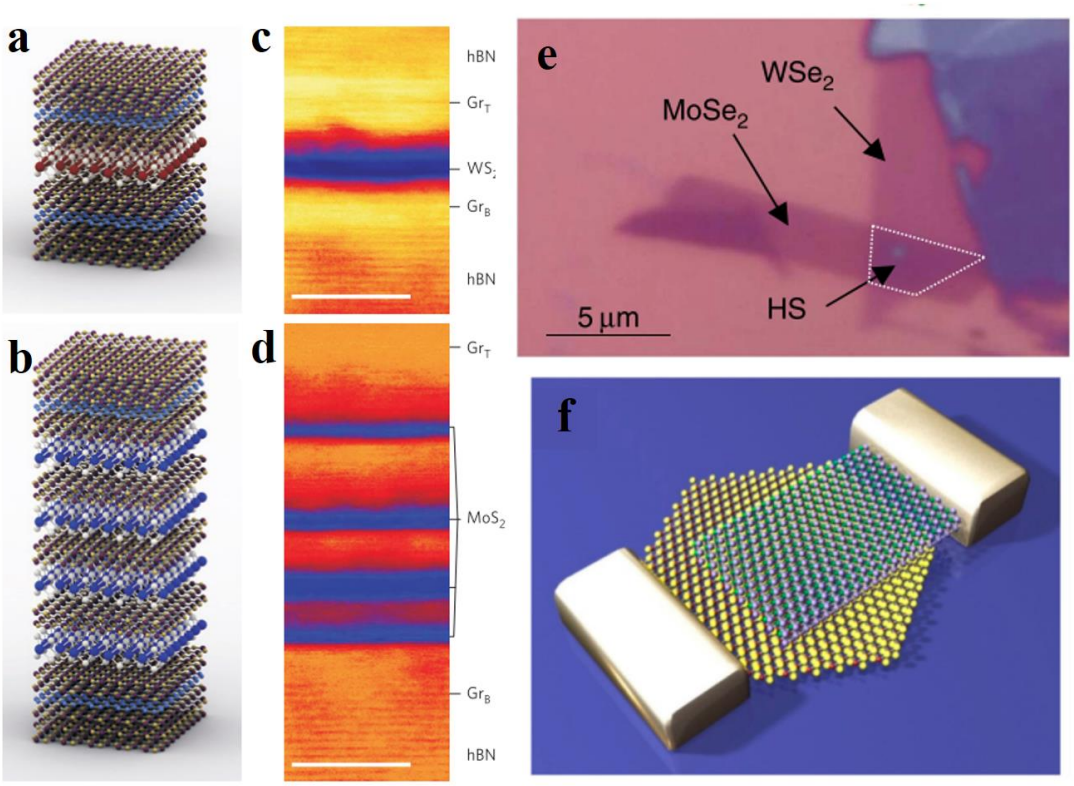


Figure 2.15 Novel electroluminescent devices based on 2D materials. (a-d) Schematics and cross-sectional bright-field scanning transmission electron microscope images of h-BN/Gr/h-BN/WS_2/h-BN/Gr/h-BN and h-BN/Gr/h-BN/MoS_2/h-BN/MoS_2/h-BN/MoS_2/h-BN/MoS_2/h-BN/Gr/h-BN. Scale bar: 5 nm. Reproduced with permission from Ref 129. Copy right 2015, Nature Publishing Group. (e) Optical image of the $MoSe_2$/WSe_2 heterostructure. Reproduced with permission from Ref 130. Copy right 2015, Nature Publishing Group. (f) Schematics of the WSe_2/MoS_2 heterojunction device. Reproduced with permission from Ref 133. Copy right 2014, American Chemical Society.

More studies on the electroluminescent devices are summarized in **Table 2.4**, with detailed structures, device types, quantum efficiencies and turn-on currents[121].

Table 2.4 Summary of the electroluminescent devices based on 2D materials

Year	Structure	Device type	QE	Turn-on current	Ref
2013	MoS_2	Schottky diode	~10^{-5}	~100 μA	134
2014	Ion-gated WS_2	Lateral p-n diode	-	~μA	127
2014	Split-gated WSe_2	Lateral p-n diode	~1%	-	135
2014	Split-gated WSe_2	Lateral p-n diode	~0.1%	<50 nA	136
2014	Split-gated WSe_2	Lateral p-n diode	~0.1%	200 pA	137
2014	p+Si/MoS_2	Vertical p-n diode	-	100 nA	138
2014	p+Si/MoS_2	Vertical p-n diode	-	15 μA	139
2014	WSe_2/MoS_2	Vertical p-n diode	-	~10 μA	128
2015	Gr/h-BN/WSe_2/h-BN/Gr	Single QW	~6%	0.5 μA/μm^2	140
2015	Gr/h-BN/MoS_2/h-BN/Gr	Single and multiple QWs	1-10%	1.8 nA/μm^2	129
2016	WS_2	Schottky diode	-	~400 nA	141
2016	Gr/h-BN/WSe_2	MIS	-	~0.57 μA	142
2017	WS_2/h-BN/Gr	MIS	~1%	<1 nA	143
2017	Gr/h-BN/MoS_2/h-BN/Gr	Single QW	0.2%	-	144
2019	Gr/h-BN/WS_2/h-BN	Single QW	0.69%-4.52%	-	122
2020	Gr/h-BN/WS_2/h-BN/Gr	Single QW	0.02%-0.18%	-	123

2.5 Conclusions and Outlook

In summary, the unique properties of 2D materials provide several benefits over other bulk materials, such as ultrathin, highly transparent, high surface to volume ratio and 2D quantum confinement of excitons. All of these make 2D layered materials a prime candidate in the field of next-generation optoelectronics. Devices based on individual 2D materials and heterostructures have been successfully fabricated by the direct growth of CVD or manually transfer. For graphene-based devices, they appear to be a promising candidate for ultra-broadband photodetectors. Devices based on TMDs normally show very high responsivities and gains due to the slower electron-hole recombination caused by the inherent property of the semiconductor bandgap and carrier transfer. Moreover, devices based on the hybrids of 2D layers pave a new way to design novel electronic and optoelectronic devices, where semimetal graphene with a tunable work function serves as contact electrodes and TMDs as the active absorbing channel in photodetectors. As for the electroluminescent devices, the durability, reproducibility and scalability are always a striving direction for the researchers. The quality of the surface and interface is also worth exploring as it influences the device performances.

Despite the recent progress, there are still many challenges existing in this field. For scientific research, more efforts are required to increase the homogeneity in 2D materials during the production. Optoelectronics with superior performances are always expected to achieve, which is a hot subject in the field of 2D devices. For the practical application, the cost, yield, stability and uniformity are critical issues that must be tackled.

In future work, investigations on 2D optoelectronics must be based around their unique properties, not simply replacing other materials in existing frameworks. I envision that 2D material-based optoelectronics can be further developed in mainly two directions. On the one hand, a stacking technique is required for assembling each 2D layer one-by-one to achieve arbitrary stacks in arrays. On the other hand, by utilizing graphene as a metallic electrode and TMDs as the active semiconductor material, it will be possible to create a new class of optoelectronics that have multi-stacked heterostructures to increase the light absorbed, like a ‘tandem cell’.

Chapter 3 Methodology

3.1 Introduction

This chapter aims to list all the techniques employed throughout this doctoral project. It begins with the materials synthesis, followed by the device fabrication and characterization, and ends by the device measurement. The flow chart of the process is drawn in **Figure 3.1** as below.

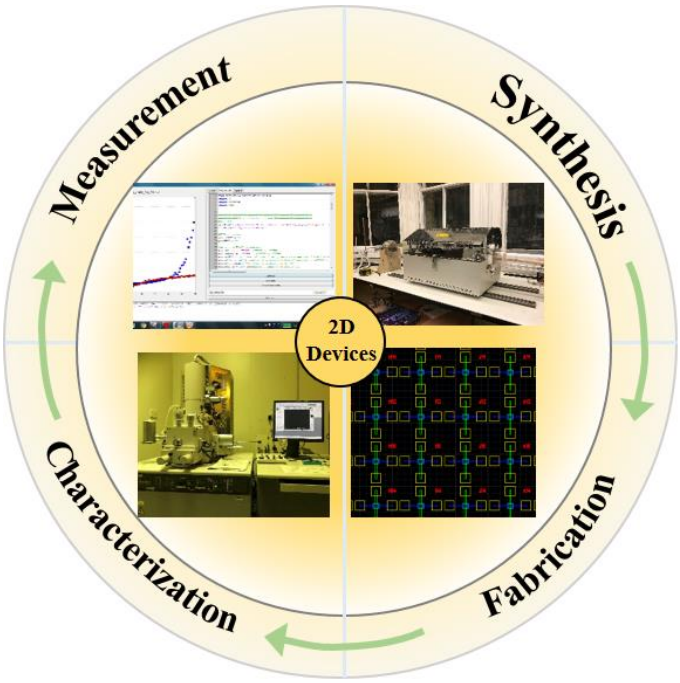


Figure 3.1 Overview of the main steps involved in this project.

3.2 Synthesis of 2D Materials

All 2D materials used here are produced by the bottom-up approach, either CVD or sulfurization. The recipes are established by the senior group members, but optimized by the author in order to get a higher coverage, 100% ideally. For all the projects, graphene and WS_2 are synthesized by the author while MoS_2 is provided by the collaborator from my group. The schematic of a typical setup for the synthesis is displayed in **Figure 3.2** as below.

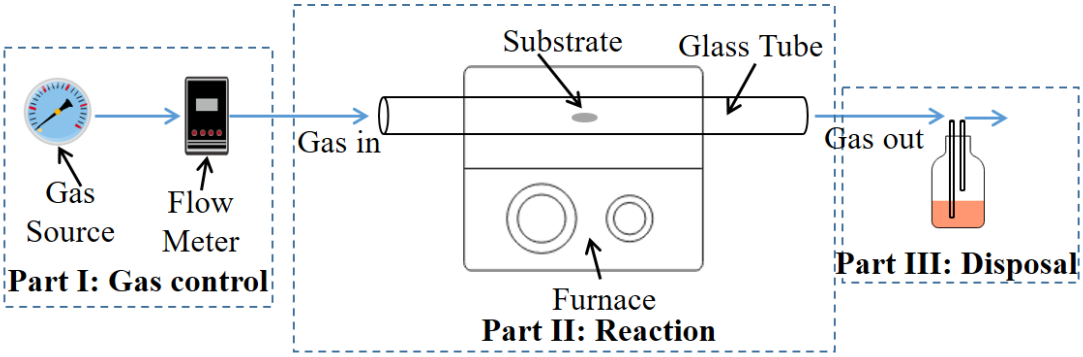


Figure 3.2 Schematics of a typical synthesis setup, including three parts: gas control, reaction and disposal.

3.2.1 Graphene

The graphene film was grown via the CVD method on the copper foil (25 μm thickness, 99.8% purity, Alfa Aesar)[42]. The foil was first ultrasonicated in diluted hydrochloric acid solution (HCl, 1 mol/L) for 5 min to remove the copper oxide and rinsed in deionized water to remove the HCl. This is followed by another cleaning process for 10 min each in acetone and isopropanol (IPA) to remove the organic residuals. After dried by the nitrogen gun, the copper foil was placed on a ceramic boat in a 4-inch tube. Three gases were involved during the reaction: Ar (pure), H_2 (25% in argon) and CH_4 (1% in argon). The system was first purged with all three gases for 20 min, followed by another 10 min purging with only Ar and H_2 to remove the residual air. The furnace was then ramped up to 1060 ºC under flows of 500 sccm Ar and 100

sccm H_2. The copper foil was annealed for 1 h in order to smoothen the surface. Then 5 sccm CH_4 was introduced to the system for the growth of graphene for another 1 h. Finally, CH_4 was turned off and the furnace was slid away in order to fast cool down the furnace to the room temperature.

3.2.2 TMDs

MoS_2: The MoS_2 film was grown via the sulfurization method on the soda lime silicate glass[145]. Molybdenum trioxide (≥99.5%, Sigma-Aldrich) was first dissolved in 28.0% NH_4OH solution followed by spin-coating at 4500 rpm for 60 s. The glass was then heated at 300 ºC in air for 10 min to completely remove the water residue. Two furnaces were used to separately control the temperature. 300 mg sulphur powder (≥99.5%, Sigma-Aldrich) was loaded in the centre of the furnace upstream while the predeposited substrate was placed in the centre of the second one. The system was first purged with Ar for 30 min to remove the residual air. Then the gas flow was maintained at 150 sccm when the temperature of the substrate was increased to 840 ºC. The substrate was annealed for 15 min and the temperature of S was set to 130 ºC afterwards. The reaction was complete in 20 min. Finally, the furnace was slid away in order to fast cool down to the room temperature.

WS_2: The WS_2 film was grown via the CVD method on the SiO_2/Si substrate (300 nm oxide layer, University Wafer)[37]. The substrate was ultrasonicated in acetone and then IPA for 15 min each. Two furnaces were used to separately control the temperature. 300 mg sulphur powder and 200 mg tungsten trioxide (≥ 99.5%, Sigma-Aldrich) were loaded at the central area of furnace 1 and 2 in the outer and inner tube, respectively. The substrate was placed 10 cm downstream away from WO_3. The system was first purged with Ar for 30 min to remove the residual air. Then furnace 1

was heated to 180 °C at a ramping rate of 30 °C/min while furnace 2 was heated to 1145 °C at a ramping rate of 40 °C/min under a flow of 250 sccm Ar. The growth lasted for 4 min and was stopped by reducing the gas flow to 10 sccm and setting furnace 2 to 25 °C. After the temperature of furnace 2 was decreased to 1010 °C, furnace 1 was set to 400 °C. This is followed by increasing the gas flow back to 500 sccm to remove the remaining S powder. Finally, the furnace was slid away in order to fast cool down to the room temperature.

3.3 Device Fabrication Process

3.3.1 2D Materials Transfer Method

In general, a wet transfer process was used to transfer the as-grown 2D materials from the substrate. A layer of poly (methyl methacrylate) (PMMA, 495K, A8) was spin-coated on the grown 2D materials as a sacrificial medium and then cured at 180 °C for 90 s. For graphene, ammonium persulfate solution (APS, 0.2M) was used to etch the copper foil. For WS_2, potassium hydroxide (KOH solution, 1 mol/L) was used to etch the SiO_2. After etching, the PMMA membrane with 2D materials was transferred to deionized water for three times (2 hours each time) to wash away the remaining residuals. For MoS_2, deionized water was used to directly detach the film from the glass. The floating film was scooped with the target substrate. After dried overnight in the fume hood, the sample was annealed at 150 °C for 30 min for a better adhesion between the film and the substrate. Finally, PMMA was removed by acetone.

3.3.2 Electron-Beam Lithography (EBL)



Figure 3.3 Image of the EBL system in the cleanroom.

EBL is a powerful tool for creating super small nanostructures, down to a few nanometres. Its pattern is directly designed in *AutoCAD* without the need of designing a physical photomask, which enables fast and cost-free changes. Basically, photoresist is first deposited on the sample by spin-coating. By moving a highly focused electron beam over the sample, the pattern is written out. Being sensitive to the electron beam, the exposed part changes the solubility after the exposure. The positive resist becomes soluble after the exposure while the negative resist has the opposite effect. Finally, the soluble part is dissolved in the developer and the pattern is displayed on the sample.

In this project, the EBL system (JEOL JBX-5500FS) was used to pattern the resists (**Figure 3.3**). For the fabrication of metal bond pads, bilayer positive resists were coated to obtain an undercut structure, demonstrated in **Figure 3.4**. In details, the sample was first spin-coated with a layer of PMMA (495K, A4) with the spin speed of 4500 rmp for 45 s and baked at 180 ºC for 90 s. This is followed by spin-coating another layer of PMMA (950K, A4) with the same recipe. The dose of EBL is 650 $\mu C/cm^2$ with the developer of MIBK: IPA=1:3 for 45 s. For the fabrication of 2D arrays, a layer of the positive resist should be coated before the negative one to avoid a strong attachment between the negative resist and 2D materials. The sample was first spin-coated with a layer of PMMA (495K, A8) with the recipe mentioned before, followed by spin-coating another layer of maN-2403 with the spin speed of 3000 rmp for 30 s and baked at 90 ºC for 90 s. The dose of EBL is 180 $\mu C/cm^2$ with the developer of ma-D525 for 150 s.

3.3.3 Metal Deposition

A thermal evaporator (Edward 360) was used for the metal deposition. Samples, fixed by the tape, were placed upside down on a plate. The chamber was pumped down and the evaporation should not begin until the pressure gets down to 1×10^{-5} mbar. By slowly increasing the current passing through the metal source at ~5 A every 30 s, the metal starts to melt and evaporate. The deposition rate is controlled by the current with a desired value of ~0.1-0.2 nm/s. The metal sources were then evaporated to the sample. Usually 10 nm Cr (rod) and 70 nm Au (99.99%, pellet, Kurt J. Lesker) were deposited for the metal electrodes or 80 nm Au only for the markers. This is then followed by a lift-off process in acetone.

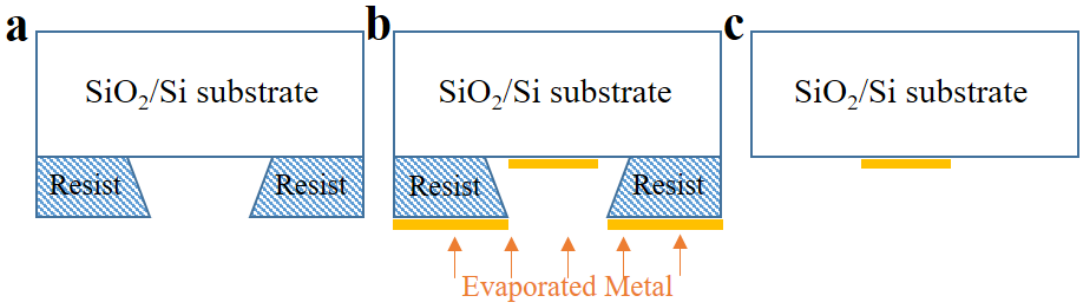


Figure 3.4 Steps for the metal deposition. (a) Undercut structure after the coating of bilayer resists. (b) Process of the thermal evaporation. (c) Metal bond pads deposited on the substrate followed by the removal of resists by acetone.

3.3.4 Reactive-Ion Etching (RIE)

The Diener plasma etcher with a 40 kHz RF was used for generating oxygen (O_2) plasma to remove the unwanted part of PMMA or 2D materials. The etching power and time should be carefully controlled or the 2D building blocks covered by the PMMA and maN-2403 will also be removed. The chamber was first pumped down and then introduced with O_2 under a chamber pressure around 0.3 mbar. The etching RF power was set to 60 W and time for 50 s each cycle. Graphene covered by PMMA requires 3 cycles. WS_2 and MoS_2 are more difficult to etch and thus requires 5 cycles. As an example, optical images of graphene ribbons before and after the RIE are displayed in **Figure 3.5**.

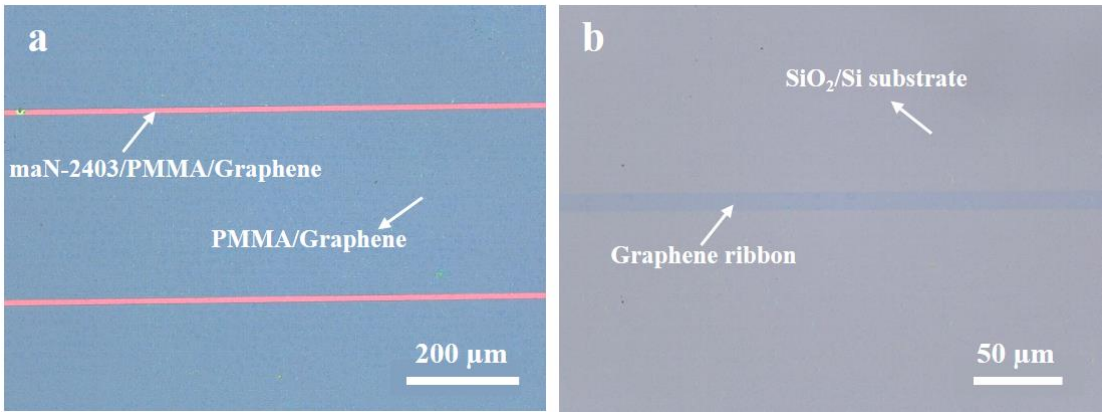


Figure 3.5 Optical images of graphene ribbons before (a) and after (b) the RIE.

3.4 Materials Characterization

3.4.1 Optical Microscopy (OM)

OM uses lenses and visible light to magnify and inspect samples. Images can be captured by complementary metal-oxide-semiconductor (CMOS) or charge-coupled device (CCD) cameras. Contrast, brightness and white balance can be adjusted using *Image J*.

A custom-built OM with 10× magnification objective lens was used to quickly check samples. Mono- and bilayer 2D materials can be obviously distinguished due to the different contrast, as shown in **Figure 3.6**.

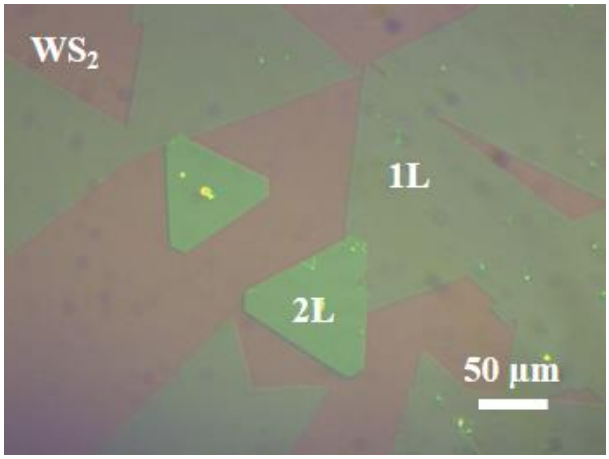


Figure 3.6 Optical image of mono- (1L) and bilayer (2L) WS_2 on the SiO_2/Si substrate.

3.4.2 Scanning Electron Microscopy (SEM)

SEM utilizes a focused electron beam to scan over the surface of a specimen, with the ability to provide high resolution images. The Rayleigh criterion is expressed by:

$$r = \frac{0.61\lambda}{n\sin(\alpha)} \qquad (3.1)$$

where r is the resolution, λ is the wavelength, n is the refractive index and α is the angular aperture of objective lens. Therefore, a smaller wavelength will result in

a closer distance between points in a specimen. In order to avoid charge building up on the sample, electrical conductivity must be rendered.

A scanning electron microscope (Hitachi-4300) was used to observe samples under an accelerating voltage of 3.0 kV, with a resolution down to 100 nm. A carbon tape was used to fix the sample on the stub.

3.4.3 Raman and Photoluminescence (PL) Characterization

Raman uses scattered light to determine the vibrational, rotational and other modes of molecules. It relies on the inelastic scattering of photons. Typically, a source of monochromatic light, usually from a laser, is used to irradiate the sample. The laser interacts with the chemical bonds, leading to a shift in the energy of the laser photons. This shift provides with the information about the molecule system, being an effective tool to quantitatively assess the thickness, strain and doping level of 2D materials[146,147,148,149,150].

PL is used to measure the purity and crystalline quality of semiconductors. The sample is initiated with a laser which gives the electrons enough energy (larger than the band gap energy) to travel from the valence band to the conduction band. The electrons then recombine with holes, emitting photons. Both WS_2 (2.03 eV) and MoS_2 (1.8 eV) are targeted for the red wavelength region[151]. The PL spectra are captured in the unit of wavelength (nm), but should be converted to the unit of energy (eV) for the peak fitting using the Planck-Einstein relation:

$$E = h\nu = h\frac{c}{\lambda} \qquad (3.2)$$

where E is energy, h is the Planck constant, c is the speed of light, ν is the frequency and λ is the wavelength.

Raman and PL measurements were carried out using an imaging confocal Raman microscopy (JY Horiba LabRAM ARAMIS) through a 50 x objective lens with a spot size of ~1 μm. An excitation wavelength of 532 nm green laser was generated by a frequency-doubled Nd:YAG laser source. Rapid profiling was performed using 1800 slits per mm gratings for Raman and 600 slits per mm gratings for PL. Both the single spectrum acquisition and mapping function were used to detect the sample, which are for the individual point and the spatial uniformity information respectively. Lorentzian multipeak fitting was applied to the spectra to extract different peaks using *Origin*. A monolayer MoS_2 domain characterized by PL single spectrum acquisition and mapping is demonstrated in **Figure 3.7** as an example.

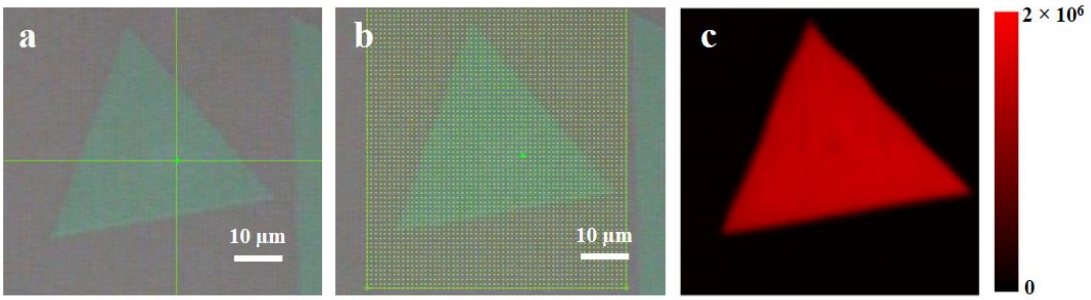


Figure 3.7 Optical characterization of a monolayer MoS_2 triangular domain. (a) Optical image of a MoS_2 domain for the single spectrum acquisition. (b) Optical image of a MoS_2 domain for the mapping acquisition. (c) PL integrated intensity mapping of the domain in (b).

3.4.4 Annular Dark-Field Transmission Electron Microscopy (ADF-TEM)

TEM characterizes the sample by using an electron beam to transmit it. This technique is capable of reaching a significant high resolution, where atomic structures, stacking orders, vacancies and grain boundaries can be captured[31,42,152].

ADF-STEM imaging was conducted using Oxford's JEOL ARM-200 cold field emission gun transmission electron microscope with a Cs probe corrector under an accelerating voltage of 80 kV. The 2D materials covered by PMMA was scooped onto

a grid. After the removal of PMMA, the 2D crystals were suspended on the grid. The obtained TEM images were often processed to have false colours for a better contrast. The corresponding atomic models were plotted using *Crystal Maker* and *Discovery Studio*. The intensity line profile was measured using *Image J*.

3.5 Electrical and Optoelectrical Measurements

Two source meters (Keithley 2400-LV) were used for the electrical measurements. Tungsten tips (Signatone SE-T) were used to probe the metal bond pads of each device and to apply a bias sweep. The gate voltage was applied from the back side of the p-doped SiO_2/Si substrate (300 nm oxide) with a silver paste.

For photocurrent measurements, a 532 nm diode-pumped solid-state laser (Thorlabs, DJ532-40) coupled into a confocal microscope was used as the illumination source with a spot size of ~150 μm^2. Its intensity was controlled via a current controller and the working temperature was set to 24.83 ºC. The power values of the laser were recorded by a manually fixated power meter (Thorlabs Optics PM100D, ± 3% accuracy) placing under the objective lens.

A custom-built microscope/spectrometer system was used to collect EL videos/spectra. It contains a spectrometer (SP-2300 spectrometer, Princeton Instruments Acton) and a CCD camera (PIXIS 100 CCD, Princeton Instruments Acton) attached to an optical microscope with a 10× objective lens and a 532 nm diode-pumped solid laser, as mentioned above. The temperature of the cooler was set to -75 °C. The background spectrum should be acquired first and the exposure time should be kept the same for the following experiments.

In this thesis, although graphene is utilized as the electrode, its resistance added to the circuit cannot be neglected. The sheet resistance of graphene film can be affected by many factors, such as the preparation method, layer number, substrate type, doping level, etc[153,154,155,156]. As reported by the group, the average sheet resistance of the CVD-grown bilayer graphene transferred on the SiO_2/Si substrate was measured to be 713.4 Ω/sq[42]. Here, to calculate the resistance of the monolayer graphene used in the following research, arrays of Cr/Au contacts were deposited on the SiO_2/Si substrate with 150 μm channel length. Then graphene was transferred and patterned to ribbons. The designed ribbon width is 5 μm but the actual width is between 5 μm and 10 μm. As shown in **Figure 3.8**, the slope of the fitting line $1/R$ is 3.76 ×10^{-5} 1/Ω. Therefore, the estimated sheet resistance of the monolayer graphene is ~ 1329 Ω/sq.

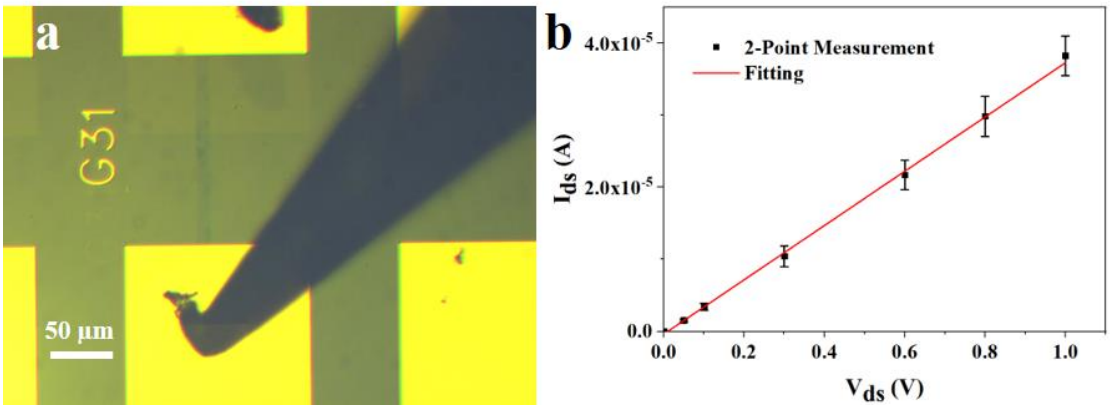


Figure 3.8 Electrical characterization of a graphene ribbon. (a) Optical image of an electrical measurement setup of a device. (b) Output I_{ds}-V_{ds} curves for the resistance measurement of graphene ribbons.

Chapter 4 Large-Scale Uniform-Patterned Arrays of Ultrathin All-2D Vertical Stacked Photodetector Devices

4.1 Introduction

Producing 2D devices in arrays is of great importance to the industrial scale-up because they are the fundamental for the modern microelectronic circuits. Currently, some possible ways to prepare 2D arrays include photolithography, 2D printing, growth, and self-assembly[157]. The scaling from single elements to arrays is relatively straightforward provided that the 2D building blocks can be grown in high quality across a large area, with the main challenge being the development of a suitable stacking method to make a pixel-by-pixel electronic readout. Therefore, the precision of the alignment is essential. Most of the alignment methods originate from the traditional wet and dry stacking, where a long working distance optical microscope is used along with micropositioning systems[71,80]. However, this approach is only for the 2D flakes/domains and has not been tested for stacking arrays. Lacking a suitable stacking method largely hinders the fundamental study and development of the electronics from the lab to the fab.

Here, a marker-assist-aligned stacking method is demonstrated for the batch assembly of 2D arrays. The whole process is industry compatible with all the 2D materials grown into continuous films initially and patterned to arrays via electron-

beam lithography. Customized markers delicately designed in pairs are predeposited to guide the transfer. Isopropanol (IPA), rather than water, is used during the transfer for a cleaner interface and stronger adhesion. To prove this idea, I fabricate hundreds of the Gr/MoS_2(2L)/Gr photodetector arrays in a batch on a 1 cm × 1 cm SiO_2/Si substrate. I also examined the uniformity of the devices by SEM, Raman spectroscopy, PL, and electrical measurements. I show that this method is suitable for the large-scale fabrication of ultrathin all-2D device arrays with various sizes, shapes, and spacings.

4.2 Results and Discussions

4.2.1 Demonstration of the Marker-Assist-Aligned Stacking Method

When multiple 2D materials are used in a vertical layout, it requires that they are prepatterned first, rather than use reactive ions or oxygen plasma to etch a multilayer stack to form the device. Therefore, our initial test is to use a needle to align the top graphene ribbon arrays orthogonal to the bottom counterparts under an optical microscope to form a cross-bar structure, as demonstrated in **Figure 4.1**a. Two sets of graphene ribbon arrays with bond pads are first prepared on the SiO_2/Si substrates, with one of them coated with poly(methyl methacrylate) (PMMA) and then etched from the substrate. **Figure 4.1**b shows the PMMA membrane consisted of graphene ribbons with bond pads floating on the deionized water which is ready for the aligned transfer. It can be clearly seen in the picture due to the yellowish bond pads. I use an IPA-based wet transfer method to first transfer the PMMA membrane onto the target substrate[77]. As it displays in **Figure 4.1**c, a needle is used to touch the corner of the film and then adjust its relative position to the substrate. It should be pointed out that the blunt end of the needle is used, rather than the sharp one, to potentially avoid

punching holes in the film. The successful part is that the free movement of the film can be achieved by the needle and I can adjust the position of the film to the substrate. However, there are still two problems found in terms of the alignment during the test. As shown in **Figure 4.1**d, one is that the graphene ribbons are highly transparent and hard to be observed, making it difficult to align the top ribbons to the bottom ones. The bond pads can be regarded as a sign to help with the alignment, although only serving as a rough guide. The other is that the scope under the optical microscope is only restricted to a small area, but the misalignment will gradually become apparent with the distance even by a tiny angular error. The SEM image in **Figure 4.1**e displays the crossbar devices in a larger region on the wafer after removing PMMA where the lateral precision decreases with the distance across the wafer scale. From this starting point, it is known that the layer-by-layer transfer of arrays poses challenges of registering each layer. This obstacle must be improved in the next step where patterned semiconducting materials between these two graphene cross-bar electrodes will be inserted to form photodetector vertical devices.

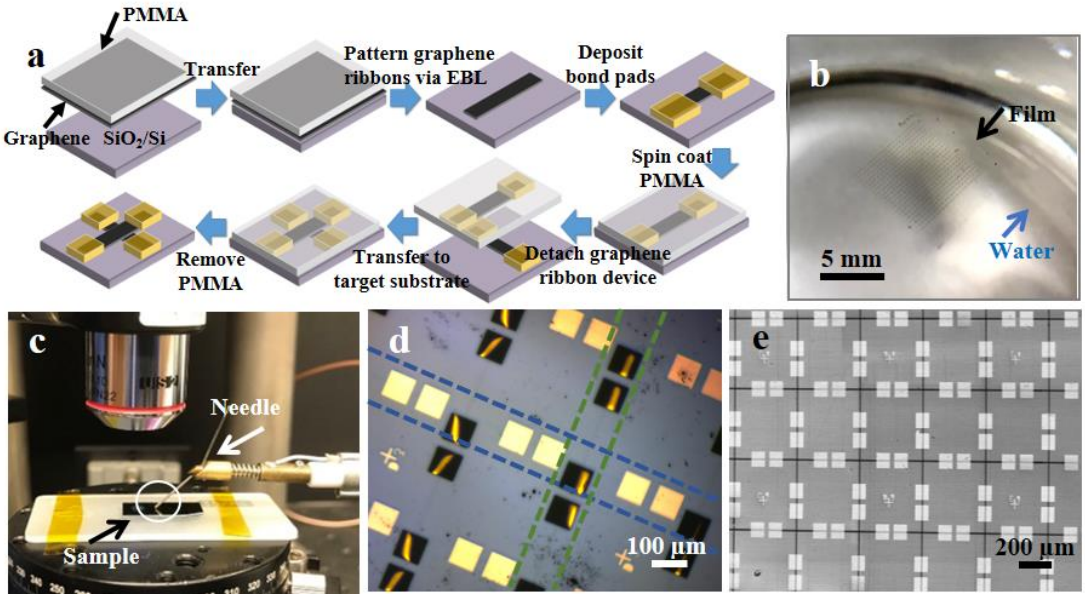


Figure 4.1 Initial test of the aligned stacking method by fabricating graphene cross-bar arrays. (a) Process of transferring one graphene ribbon orthogonally to the other graphene ribbon which forms the graphene cross-bar structure. (b) Image showing the PMMA membrane with graphene ribbons and bond pads floating on the water. (c) Demonstration of the aligned stacking method. The white circle in the image pointed out that the blunt end of the needle is in direct contact with the film. The needle is used to adjust the position of the film relative to the substrate. (d) Optical image showing the graphene ribbons before the alignment. The bottom graphene ribbons are between the blue dotted lines, while the top ones are between the green dotted lines. Due to the ray of light, the top bond pads appear blackish under an optical lens, making them easily recognizable. (e) SEM image of the aligned graphene cross-bar sample after removing PMMA.

I upgrade the existing stacking process by developing pairs of markers which can interlock with each other. The process for the marker-assist-aligned stacking method is schematically displayed in **Figure 4.2**a. The brief idea is to use standard resist-based lithography to pattern each 2D continuous film into arrays, and then use an optical aligner to correlate the position of the arrays on the substrate. Markers are designed in pairs which can interlock with each other to locate the position. By transferring each batch of arrays to the right position in sequence, the target vertical layered heterostructure (VLH) can be assembled on a large scale with lateral precision at one time.

The main steps are described as follows: first, large continuous 2D films are prepared on the SiO_2/Si substrates with the initial one known as F_1 and so on (i). Here, 2D films are favoured because exfoliated flakes or domains exhibit irregular shapes and random positions, and thus they are not ideal for the batch process. Then, the reference markers (marker X) and their matching markers (marker X′) which can interlock with each other are deposited on the target substrate and 2D layers, respectively, with special features of Roman numerals from 1 to N (ii). N is the number of times that requires the marker-assist-aligned transfer. A unified coordinate system is shared by both the target substrate and the 2D film. This is followed by patterning the 2D film into arrays via reactive ion etching (iii). After being coated with PMMA, the SiO_2/Si substrate is etched away by KOH, and the floating membrane consisting of PMMA, 2D arrays, and marker X′ is transferred to deionized water three times in order to remove the residues (iv). Next, a piece of thin cover glass is used to scoop the film from the water, and it is then transferred to the target substrate via IPA (v). After that, the substrate is placed onto a rotational mount and a needle connected to a three-axis translation stage is lowered down until touching the film (vi). Meanwhile, an optical microscope is used to see the relative position between markers X and X′. The rotational mount and the needle are for the angle and plane alignment, respectively. Once marker X′ is embedded in marker X, both the substrate and the film stopped moving, and the film will be adhered to the substrate when IPA evaporates. The sample is placed in the fume hood overnight, annealed for a better adhesion, and then put into acetone to dissolve the PMMA (vii). Finally, the first batch of 2D arrays is transferred to the desired position on the substrate (viii). By repeating the same process for the next few layers, the final target VLH can be formed.

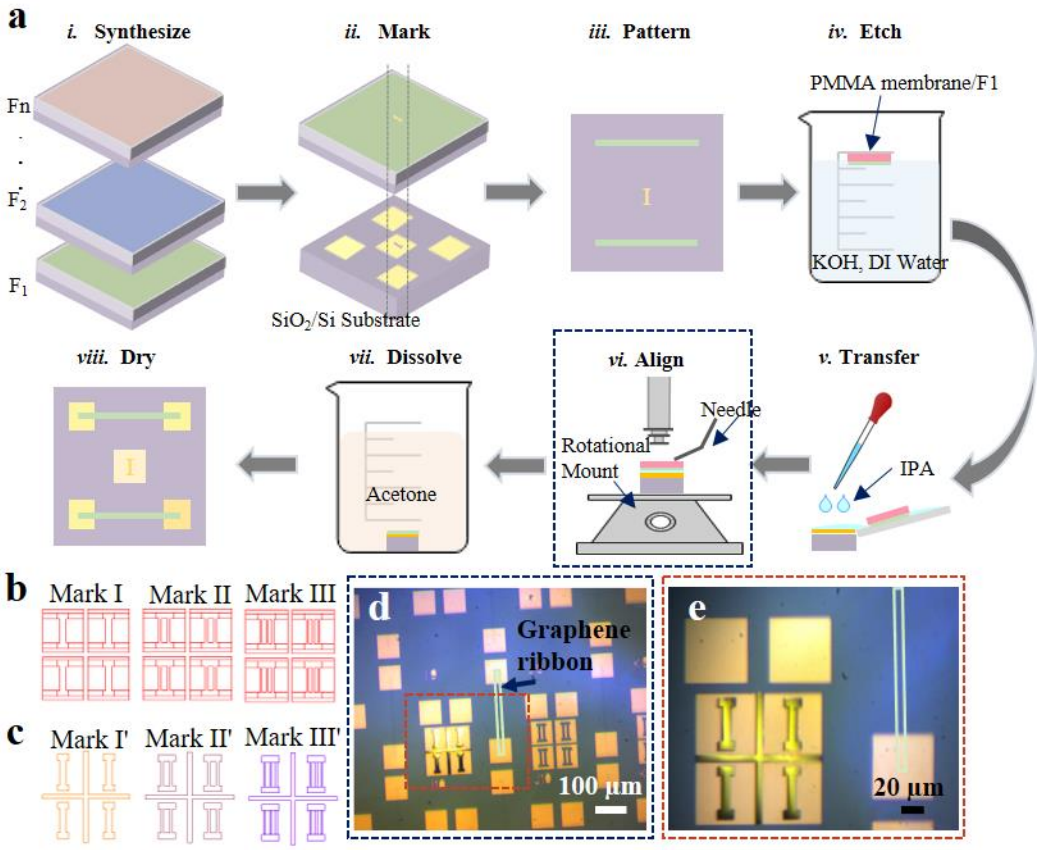


Figure 4.2 Illustration of the marker-assist-aligned stacking method for the fabrication of 2D device arrays. (a) Schematics showing the eight main steps for the fabrication process. See the main text for a detailed description. (b) AutoCAD image of the reference markers (marker X) predeposited on the target SiO_2/Si substrate. (c) Corresponding matching markers (marker X′) designed to pair marker X. (d) Optical image showing the reference marker (marker I) and matching marker (marker I′) interlocked with each other, which indicates that a batch of graphene ribbons were transferred to the desired position on the substrate. (e) Enlarged optical image of the rectangular box in (d).

Figure 4.2b shows the reference markers deposited on the substrate used for F_1, F_2, and F_3. Their matching markers deposited on the films are displayed in **Figure 4.2**c. Usually, a thin layer of chromium (Cr) is deposited before gold (Au) for a better adhesion. However, for marker X′, only Au is deposited to make the KOH etching step quicker. A further demonstration of the marker-assist-aligned transfer is presented in **Figure 4.2**d as an example. By embedding marker I′ into marker I, a batch of graphene

ribbon arrays were successfully aligned and transferred to the bottom bond pads. **Figure 4.2**e is the zoomed-in image of the red dotted box in **Figure 4.2**d. The image showing the operation stage in the lab is displayed in **Figure A1**.

4.2.2 Fabrication of Device Arrays

I prove the idea by showing an example of 2D photodetector arrays fabricated via this method. The schematic diagram in **Figure 4.3**a depicts the target Gr/MoS_2(2L)/Gr structure, where bilayer MoS_2 is sandwiched between graphene. Both the 2D materials were grown into continuous films first, characterized by SEM, as shown in **Figure 4.3**b,c. Fully continuous graphene was synthesized on copper with some thickness variation, indicated by the colour contrast. It was then transferred to the SiO_2/Si substrate and patterned to ribbons with 10 μm width to form the electrodes. As for MoS_2, instead of manually stacking it to bilayers, it was directly grown into bilayer on glass. The bilayer MoS_2 was subsequently confirmed using ADF-STEM. **Figure A2** shows that the bilayer MoS_2 sheet was well synthesized into a 3R-stacking with some monolayer parts. The coverage is not full either, attributed to the uneven deposition of the MoO_3 precursor. Moreover, the molten glass will also form a curved surface during the fast cooling. This will cause a PMMA membrane with folds during the transfer, and cracks will be left on the 2D film after removing PMMA. The 2L-MoS_2 was patterned to square blocks of 30 μm ×30 μm. **Figure 4.3**d elaborately describes the four steps for fabricating the Gr/MoS_2(2L)/Gr structure. The final substrate was first deposited with Cr/Au reference markers and bond pads. Subsequently, prepatterned bottom graphene, bilayer MoS_2, and top graphene arrays were transferred onto the substrate one-by-one using the stacking method mentioned before. This forms the target device with each one having an active region of 10 μm ×10 μm.

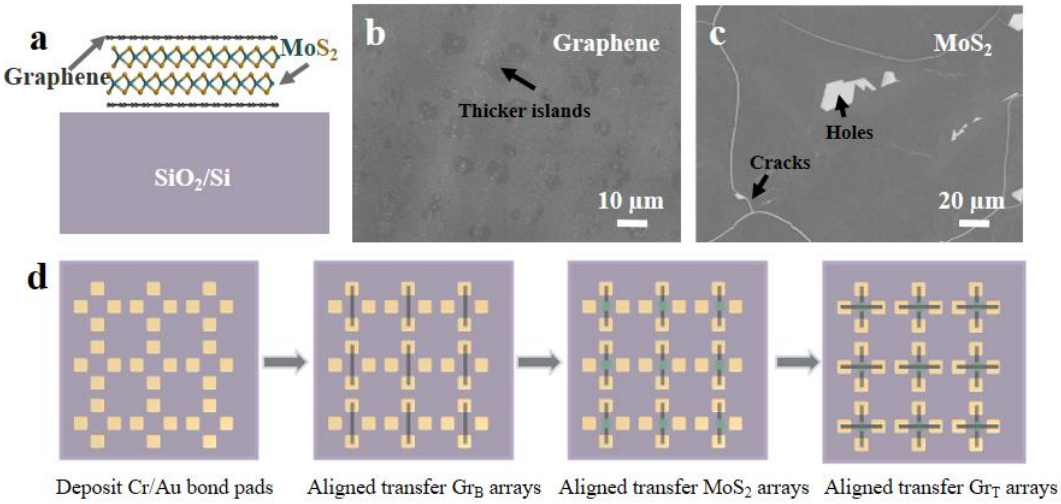


Figure 4.3 Example of the fabrication of Gr/MoS_2(2L)/Gr device arrays using the marker-assist-aligned stacking method. (a) Atomic model of the target structure Gr/MoS_2(2L)/Gr. (b) SEM image of the graphene film grown on copper foil. The non-uniform contrast indicates the thickness variation of graphene. (c) SEM image of the MoS_2 film grown on glass. It is not fully continuous with a few holes and cracks. (d) Fabrication steps for creating the target device arrays. The bond pads were first deposited on the substrate, after which the 2D arrays were aligned transferred to the target position. Gr_B: bottom graphene and Gr_T: top graphene.

4.2.3 SEM, Raman and PL Characterization

During the alignment step, error values in the microrange exist between each marker X and X′, as shown in **Figure 4.4**. It is noticed that the marker with a more refined design tends to interlock with the other better, resulting in a smaller error value. To be specific, the error values of markers II (II′) and III (III′) are smaller than those of marker I (I′) in our case. This result suggests the importance of the delicate design for the markers.

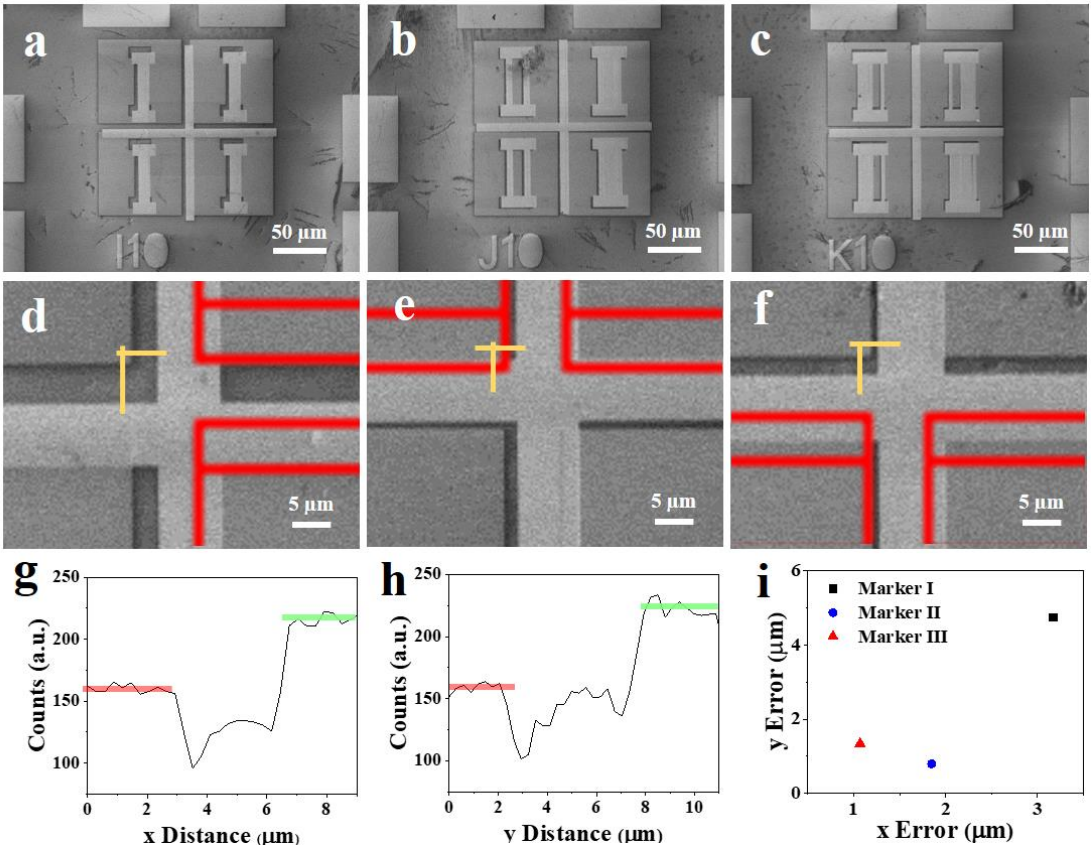


Figure 4.4 Error values in x and y directions between Marker X and X'. (a-c) SEM images of three pairs of interlocking markers after the aligned transfer. (d-f) Enlarged SEM images of the centre parts of the markers. (g,h) Intensity line profiles measured from the yellow lines in (d). The distance between Marker X and X' in x and y directions can be read from the profiles. (i) Error values in x and y directions of the three pairs of the interlocking markers.

SEM was performed first after all the fabrication process. **Figure 4.5**a presents a straightforward way to show the fabrication uniformity by viewing the spatial distribution of the device yield within an area of 0.6 cm × 0.6 cm on the SiO_2/Si substrate. Only devices that form the Gr/MoS_2/Gr cross-bar structure will be counted for the yield, and this finally allows us to obtain over 200 devices with 80% yield rate. There are three factors that result in the defective devices: (1) discontinuity of the MoS_2 film caused by the synthesis step; (2) broken graphene ribbons caused by the transfer step; and (3) the misalignment of the building blocks. **Figure 4.5**b shows an SEM image of the fabricated periodic device arrays with a magnified region shown in

Figure 4.5c. It can be seen that the graphene and MoS_2 arrays are well defined with different contrasts.

The materials were further examined by Raman and PL with an excitation wavelength of 532 nm to determine the layer number and quality. As shown in **Figure 4.5**d, the positions of G and $2D$ peaks are at 1582 cm^{-1} and 2687 cm^{-1}, respectively. Their corresponding full-width half maximum (FWHM) values are 14 cm^{-1} and 25 cm^{-1}. The $2D/G$ area and intensity ratios of Raman are 8.6 and 4.2, suggesting that the CVD-grown graphene is mostly monolayer with an estimated doping level of < 10^{12} cm^{-2} [146,148]. The small D peak at 1345 cm^{-1} implies negligible defects in graphene, proving the high quality of the material. There are some thicker islands on the graphene film and the corresponding Raman spectrum is shown in **Figure A3**a. **Figure 4.5**e shows a typical Raman spectrum of MoS_2 on the SiO_2/Si substrate with two characteristic modes of E^1_{2g} and A_{1g}. The positions of the two peaks are 382.9 and 405.2 cm^{-1}, with a delta value of 22.3 cm^{-1}. This indicates bilayer MoS_2, consistent with the previous reports[147]. The delta value for monolayer MoS_2 is around 18 cm^{-1} (**Figure A3**b). This is further confirmed by performing the PL, as shown in **Figure 4.5**f. It is noticed that the PL intensity is not very high, which is due to the indirect band gap in the bilayer. The above results prove that our marker-assist-aligned stacking method is suitable to transfer both mono- and bilayer 2D building blocks with different sizes, shapes, and spacings to the SiO_2/Si substrate to form uniform device arrays. It is friendly to 2D materials with no obvious destruction after all the fabrication process. The microthick bond pads predeposited on the target substrate will not hinder the transfer of 2D arrays because of the flexibility of the PMMA membrane.

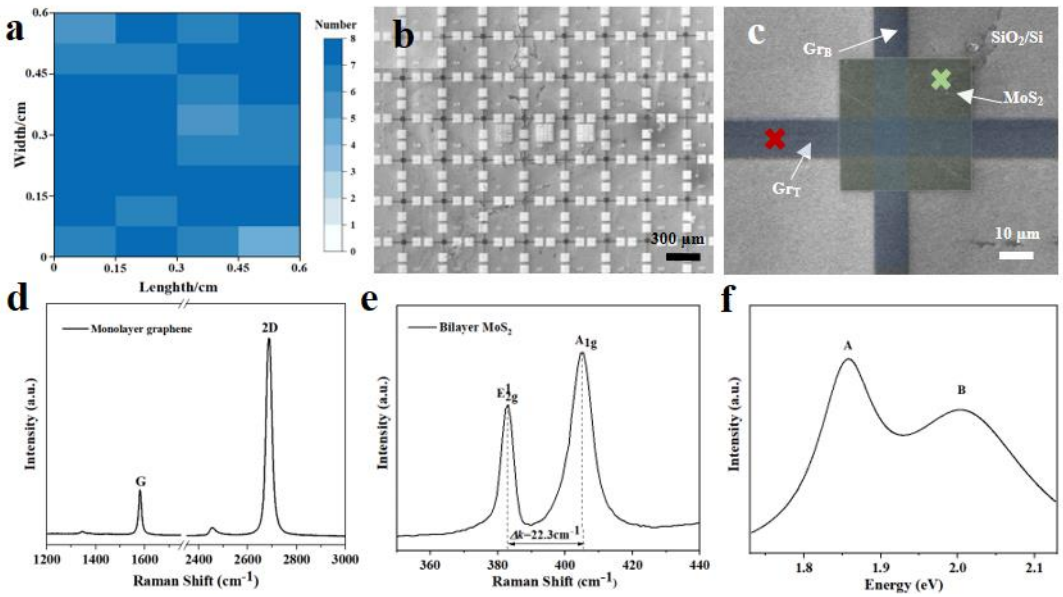


Figure 4.5 Optical characterization of the Gr/MoS_2(2L)/Gr device arrays. (a) Spatial mapping showing the uniformity of the fabrication yield on the SiO_2/Si substrate. (b) SEM image of the centre region of the fabricated device arrays. (c) SEM image of the active region of a device with false colour, showing bilayer MoS_2 sandwiched between top and bottom graphene ribbons. (d) Raman spectrum of monolayer graphene, obtained from the red cross in (c). (e,f) Raman and PL spectra of bilayer MoS_2, obtained from the green cross in (c).

4.2.4 Photodetecting Characterization

To further test the performance of the device, I applied a source−drain bias to the device under different back gates and laser powers. Here, graphene serves as transparent electrodes and sandwiched MoS_2 is the light-sensitive material. Its corresponding equivalent circuit model is presented in **Figure 6.4**b. In this common model, I_P represents the photo-generated current in the cross-bar, whilst I_{SH} and I_S are the current lost due to the shunt resistance (R_{SH}) and series resistance (R_S). The shunt resistance is attributed by the leakage due to crystal defects and impurities across the Gr/MoS_2/Gr stack. The series resistance is caused by the graphene ribbon. The measured current is then the sum of the I_P, I_{SH} and I_S. The transfer curve of the device under dark is shown in **Figure A4**, where the V-shape of the curve suggests

that the density of states of the semimetal graphene mainly dominates the carrier transport of the device[79].

When light shines on the active region, electron−hole pairs are generated in MoS_2, with an efficient dissociation time from 700 fs to 60 ps[158]. In reality, the local dielectric environment causes a difference in the doping level of the top and bottom graphene. This leads to an asymmetric tunnelling barrier between Gr_T/MoS_2 and Gr_B/MoS_2[79,120,159]. In the device, top graphene is more p-doped than the bottom one. Therefore, the Schottky barrier height (SBH) between top graphene and MoS_2 will be slightly lower, causing more electrons to migrate to the top graphene. Due to different possibilities of the electrons tunnelling to the Gr_B and Gr_T under illumination, our device can potentially be self-powered by this intrinsic photovoltaic effect.

I quantify the photovoltaic effect by two parameters: short-circuit current (I_{sc}) and open-circuit voltage (V_{oc}). As shown in **Figure 4.6**f−i, the device generates positive I_{sc} and negative V_{oc}. This is because during the photocurrent measurement, bottom graphene was grounded as the source electrode (**Figure 4.6**a). The applied external current flows from the top to bottom graphene, which has the same current flow direction as the internal one. Therefore, a positive bias results in an increase in the current value. When applying a back-gate voltage, the electric field will cause a continuous band gap tuning in bilayer MoS_2[160]. Also, graphene has a finite density of states and thus, the SBH can be modulated through an external gate voltage. However, the degree of influence induced by the gate voltage is different to the bottom and top graphene (MoS_2) because of the proximity[79,120]. In other words, when applying a positive gate voltage, bottom graphene (MoS_2) will have a stronger n-doping effect

than the top one. In the device as shown in **Figure 4.6**f, when the back gate steps toward the positive direction, the I_{ds}−V_{ds} curves experienced a gradual downshift from a maximum I_{sc} reaching around 43.9 nA (V_{oc}∼1.23 mV) to a minimum value of 2.64 nA (0.08 mV).

This can be explained by showing the band diagrams in **Figure 4.6**c−e. When there is no gate voltage, the electrons excited in MoS_2 will flow to the top graphene driven by the asymmetric barrier heights. The barrier height can be tuned when applying a back gate voltage[159]. If a negative back-gate voltage is applied, it causes an increase of the work function in graphene, leading to an enhanced band slope in MoS_2. This will help more electrons and holes to separate, and both the I_{sc} and V_{oc} will increase. On the contrary, a positive back-gate voltage will decrease the work function in graphene, and the reduced band slope will inhibit the electron−hole separation. Therefore, lower I_{sc} and V_{oc} are observed.

I then exposed our devices under different laser powers with a maximum power of 1.118 mW and studied the dependence on the illumination power. As shown in **Figure 4.6**g, when the laser power increased from 0 to 1.118 mW, a stronger photovoltaic effect can be observed with upshifting lines, reaching I_{sc} around 56.8 nA (V_{oc} ∼1.75 mV). This is because as the power increases, more electron−hole pairs are generated and contribute to the current. As an important figure of merit, photoresponsivity (R) is used to evaluate the device performance. It is defined as

$$R = \frac{I_{sc}}{P_{laser}} \qquad (4.1)$$

where P_{laser} is the laser power illuminated on the overlapping region of the device. It can be seen that both I_{sc} and R have a power-law dependence on the laser power (**Figure 4.6**i). The decreasing photoresponsivity with increasing laser power is attributed to the photo-absorption saturation in MoS_2. Detectivity (D^*) characterizes a photodetector's sensitivity with regards to the geometry, bandwidth, and noise of the device. For a simple estimation, we assume that the shot noise from the dark current is the major contributor to the total noise, and thus it is given by

$$D^* = \frac{R \times A^{1/2}}{(2eI_d)^{1/2}} \qquad (4.2)$$

where R is the photoresponsivity of the device, A is the effective area of the detector, e is the unit charge, and I_d is the dark current. The estimated detectivity is 3.45×10^9 Jones (Jones = cm $Hz^{1/2}$ W^{-1}).

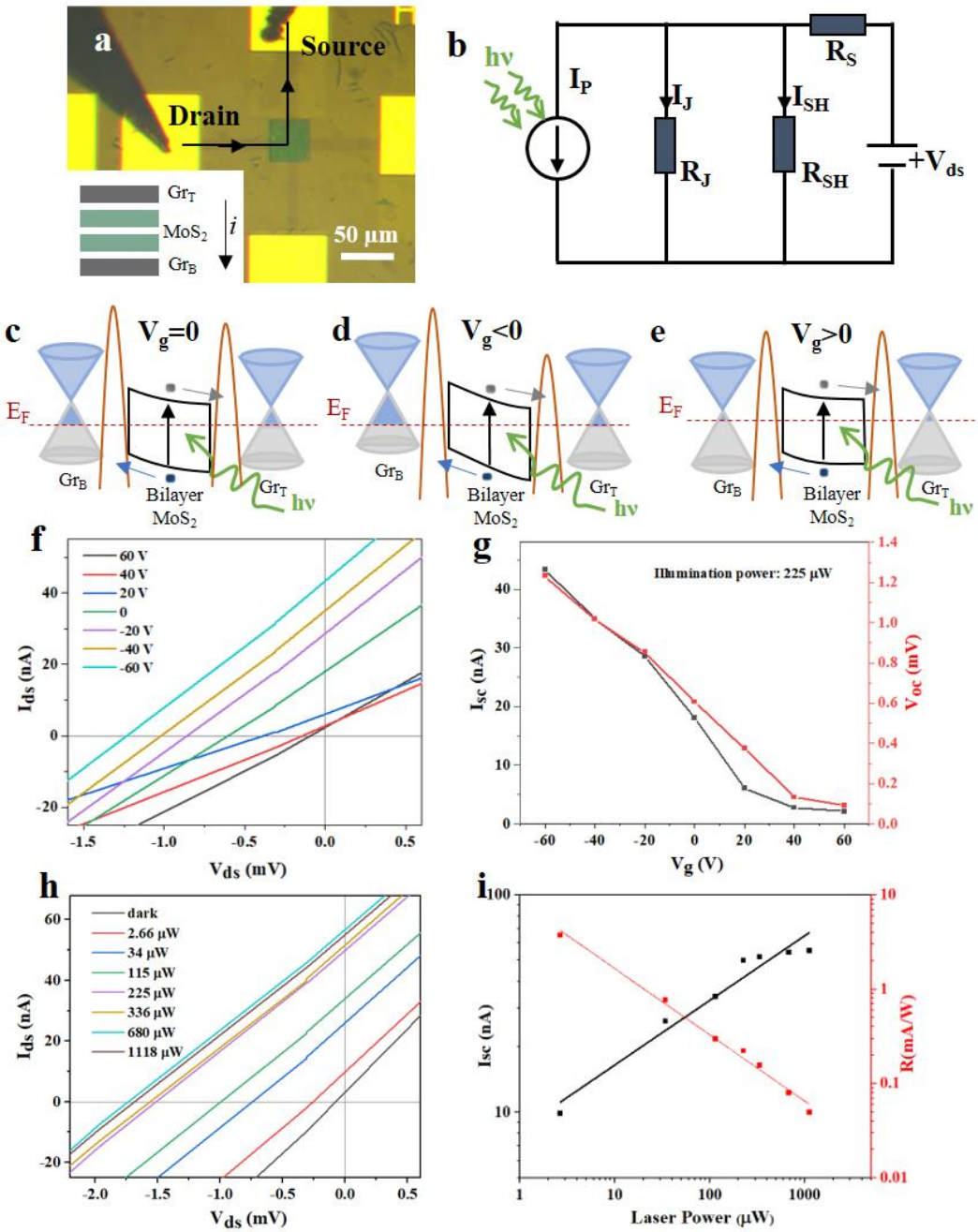


Figure 4.6 Electrical characterization of the Gr/MoS_2(2L)/Gr device arrays. (a) Electrical measurement setup of a device. Inset: current flow direction in the device. (b) Equivalent circuit model of the vertical device. I_p is the photo-generated current. R_J, R_{SH}, R_S represent the junction, shunt and series resistances, respectively. (c–e) Band diagrams of the device with zero, negative, and positive back-gate voltages, V_{ds}=0. Under light, MoS_2 is excited with electron–hole pairs being generated in both layers. The electrons then transport to graphene ribbons. The grey and blue dots represent electrons and holes, respectively. The black, grey, and blue arrows indicate the generation of electron–hole pairs, the flow of electrons and holes. The red dotted line is the Fermi level of the device. (f) Output I_{ds}–V_{ds} curves under different back gates with a fixed illumination power of 225 μW. (g) Dependence of I_{sc} and V_{oc} on the

back gate in (f). (h) Output I_{ds}–V_{ds} curves under different laser powers with −60 V back gate. (i) Dependence of I_{sc} and responsivity on the laser powers in (g). The black and red lines are the fitting curves for the I_{sc} and responsivity.

The photovoltaic effect can be further enhanced by adding another layer of WS_2 to form the $Gr_B/WS_2/MoS_2(2L)/Gr_T$ structure, where the type-II energy band will facilitate the exciton dissociation and charge separation[161]. I show the performance uniformity of the devices by providing the statistic result of the extracted short circuit current from I_{ds}–V_{ds} curves under different illumination powers, as shown in **Figure 4.7**. The average I_{sc} reaches up to 195 nA under an excitation power of 1.118 mW, which improved by more than 3 times than that in the structure without WS_2 under the same illumination conditions. I summarized the results from this work and the previous investigations from my group on the VLH which used CVD-grown WS_2 or MoS_2 domains (**Table A1**). Considering the structure and experimental condition, two sets of data from the previous paper were selected for comparison. The short-circuit current of $Gr_B/WS_2/MoS_2/Gr_T$ and $Gr_B/MoS_2/WS_2/Gr_T$ under an illumination of 0.27 mW with -60 V gate voltage is 0.67-0.88 nA/μm^2 while the short-circuit current of the $Gr_B/MoS_2(2L)/Gr_T$ device in this project is 0.44 nA/μm^2 under an illumination of 0.225 mW with the same gate voltage. It should be noticed that the $Gr_B/WS_2/MoS_2/Gr_T$ ($Gr_B/MoS_2/WS_2/Gr_T$) structure has a type-II band alignment and also a higher illumination power was used. Moreover, 2D films tend to have more grain boundaries, vacancies and mixtures of mono- and bilayers during the synthesis, which will further degrade the device performance. Despite this, our stacks show a comparable result to the previous studies, indicating again the applicability of this aligned stacking method.

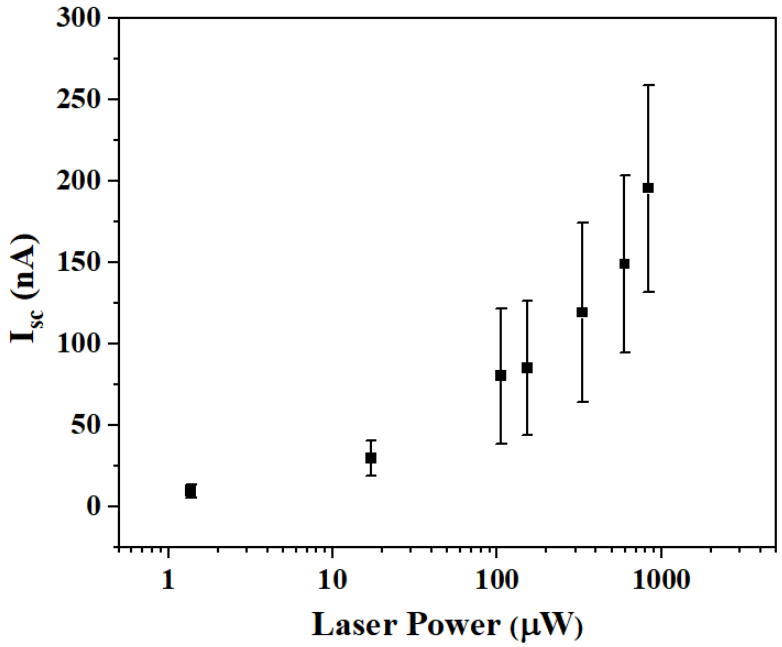


Figure 4.7 Statistic results of the extracted short circuit current from I_{ds}-V_{ds} curves of $Gr_B/WS_2/MoS_2(2L)/Gr_T$ under different illumination powers.

4.3 Conclusion

In summary, I have developed a novel method to fabricate large-scale ultrathin all-2D device arrays. All the 2D materials used are grown into large continuous films, prepatterned with desired sizes, shapes, and spacings on a substrate and then transferred to the device substrate with aligned precision. In order to achieve long-range alignment across the wafer, interlocking marker pairs are used to help guide the lateral accuracy and reduce rotational error. Over 200 $Gr/MoS_2(2L)/Gr$ devices are produced with 2D periodic spacing on a 1 cm ×1 cm SiO_2/Si substrate, with evident photovoltaic effects observed. This work provides pathways for the large-scale fabrication of ultrathin all 2D optoelectronics that forms the basis of 2D pixelated cameras and displays. As for the future work, on the one hand, the replacement of manual operation by the robotic arm will further improve the precision and efficiency

of the stacking. On the other hand, more investigations should be taken to test the integration of these 2D device arrays with CMOS, which caters to the future trend.

4.4 Contribution Statement

Linlin Hou provided constructive help in device fabrication. Yang Lu provided the MoS_2. Jun Chen did the ADF-STEM. Dr. Yingqiu Zhou and Dr.Viktoryia Shautsova provided training in device fabrication and offered some discussions.

Chapter 5 Ultrathin All-2D Lateral Diodes Using Top and Bottom Contacted Laterally Spaced Graphene Electrodes to WS_2 Semiconductor Monolayers.

5.1 Introduction

The study of the metal-semiconductor interface is essential for the development of the microelectronic devices, such as photodiodes, power rectifiers, and metal-semiconductor FETs[162,163,164]. Unlike the 3D structure, 2D Schottky junctions are free of chemical disorder and defect states which suppresses the Fermi level pinning effect[165,166]. Additionally, 2D materials have a dangling-bond free surface which allows the various combination of different layers. Therefore, to fabricate and investigate the 2D metal-semiconductor heterojunction is crucial for the suppression of metal-induced gap states and tuning the SBH.

In the last chapter, a marker-assisted stacking technique was developed for the free assembly of 2D device arrays[167]. In fact, the same approach can be further applied to construct some other interesting architectures. For example, previous studies have shown a hybrid structure where two graphene electrodes are patterned and laterally distributed on the SiO_2/Si substrate with TMDs vertically stacked on the gap[78,118]. Less studies have been focused on the structure where two graphene electrodes are in the different dielectric environments, namely $graphene_{bottom}(Gr_B)$-TMDs-$graphene_{top}(Gr_T)$. This is because the structure requires to selectively etch the 2D materials without

destroying their adjacent layer which the conventional lithography procedures cannot achieve. However, by utilizing the aligned stacking method, this problem can be easily solved.

In this chapter, a graphene-WS_2 2D van der Waals Schottky heterojunction is investigated. I use CVD-grown materials to fabricate the Gr_B-WS_2-Gr_T structure and study its optoelectronic performances. This is achieved by using the aforementioned stacking method which requires each 2D material pre-patterned and then align-transferred. Another structure of Gr_B-WS_2-Gr_B is also fabricated for comparison. Several techniques, including OM, SEM, Raman and PL, are used to characterize the as-fabricated sample for the interactions between the graphene and WS_2. The photodetecting and light-emitting behaviours of the device are also examined. This work contributes to the current understanding of the 2D metal−semiconductor heterojunction and offers an idea to obtain all-2D Schottky diodes by retaining the ultrathin device concept.

5.2 Results and Discussion

5.2.1 Demonstration of the Asymmetric Structure

The optical images of the CVD-grown 2D continuous films and their corresponding patterned building blocks are displayed in **Figure 5.1**a-d. The fabrication process of the lateral-graphene contacted vertically stacked WS_2 heterostructure is described as below. First, Cr/Au (10 nm/70 nm) bond pads are deposited on the SiO_2/Si substrate using EBL and thermal evaporation. A CVD-grown graphene film is transferred to the substrate and then patterned to ribbons of 10 μm width by RIE to form the bottom graphene electrode (Gr_B). Semiconducting WS_2 is grown into a continuous film via CVD and patterned to 40 μm × 40 μm square. The

as-patterned WS_2 is then align-transferred to the bottom graphene using our previously reported method. Finally, another layer of the pre-patterned graphene ribbon (Gr_T) is transferred perpendicularly to the bottom graphene as the top electrodes.

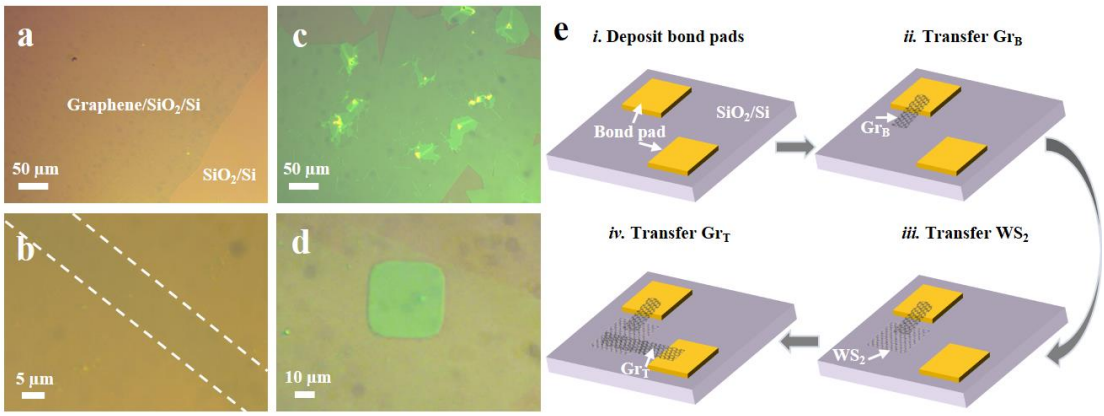


Figure 5.1 Demonstration of the Gr_B-WS_2-Gr_T structure. (a) Optical image of the CVD-grown graphene continuous film transferred to the SiO_2/Si substrate. (b) Optical image of the patterned graphene ribbon with a width of 10 μm. (c) Optical image of the CVD-grown WS_2 continuous film on the SiO_2/Si substrate. (d) Optical image of the patterned WS_2 square with a dimension of 40 μm × 40 μm. (e) Fabrication steps for creating the asymmetric structure. The bond pads are first deposited on the substrate. Subsequently, a piece of graphene film is transferred to the substrate and patterned to ribbons. Finally, the building blocks of pre-patterned WS_2 and top graphene are aligned transferred to the target position.

As shown in **Figure 5.1**e, there is no overlapping area between the bottom graphene electrode and the top one, and its gap is covered by the WS_2 square. I also fabricated the Gr_B-WS_2-Gr_B structure for comparison. As for this structure, the last fabrication step is not necessary as the two graphene electrodes can be patterned together before the transfer of WS_2. After the above process, the two types of devices, Gr_B-WS_2-Gr_T and Gr_B-WS_2-Gr_B, are obtained. The gap width is 10 μm, the same as the width of the graphene ribbon. As for the gap length, the target value is 5 μm, but the manual transfer process of the top ribbon in the Gr_B-WS_2-Gr_T structure brings variations.

5.2.2 SEM, Raman and PL Characterization

2D materials used in the heterostructure are characterized first by SEM, then Raman and PL spectroscopy, with a 532 nm excitation. **Figure 5.2**a shows the SEM image of the asymmetric lateral device, with one graphene electrode on top of the WS_2 square and the other below the WS_2 square. **Figure 5.2**b is the Raman spectrum of the graphene electrode, where three typical peaks are presented: a D peak at 1346 cm^{-1}, a G peak at 1582 cm^{-1} and a 2D peak at 2685 cm^{-1}. The D peak represents the defects in graphene and a small D peak is favoured in the material. The FWHM values of G and 2D are 21 cm^{-1} and 43 cm^{-1}, respectively. The 2D/G area and intensity ratios are 3.2 and 2, indicating monolayer graphene with an estimated doping level of $< 5\times10^{12}$ cm^{-2} [146,148]. Multilayer graphene islands can also be found but this will not be a major influence to the performance of the device. The Raman spectrum of the semiconducting WS_2 was fitted by six Lorentzian peaks, with the in-plane (E^1_{2g}) and out-of-plane (A_{1g}) vibrational modes at 354.9 cm^{-1} and 417.6 cm^{-1}, respectively. The frequency difference between these two modes is 62.7 cm^{-1}, consistent with the monolayer WS_2 in the previous reports[79,122].

The PL integrated intensity mapping of the active region of the device is shown in **Figure 5.2**d, where a quenching effect is clearly observed in the graphene/WS_2 stack. This is because the photoexcited electrons in WS_2 travel to the graphene, causing a suppressed recombination process. This phenomenon indicates a good contact between the graphene and WS_2, in accordance with the previous research[79,122]. Their corresponding PL spectra are presented in **Figure 5.2**e with the black line for the WS_2 on the SiO_2/Si substrate and the red line for the WS_2 on graphene. The PL spectrum of the WS_2 on the SiO_2/Si substrate was fitted with two Lorentzian peaks. They are peaks

at 2.01 eV and 1.98 eV, corresponding to the exciton and negative trion emissions, respectively. These values leads to a binding energy of 30 meV.

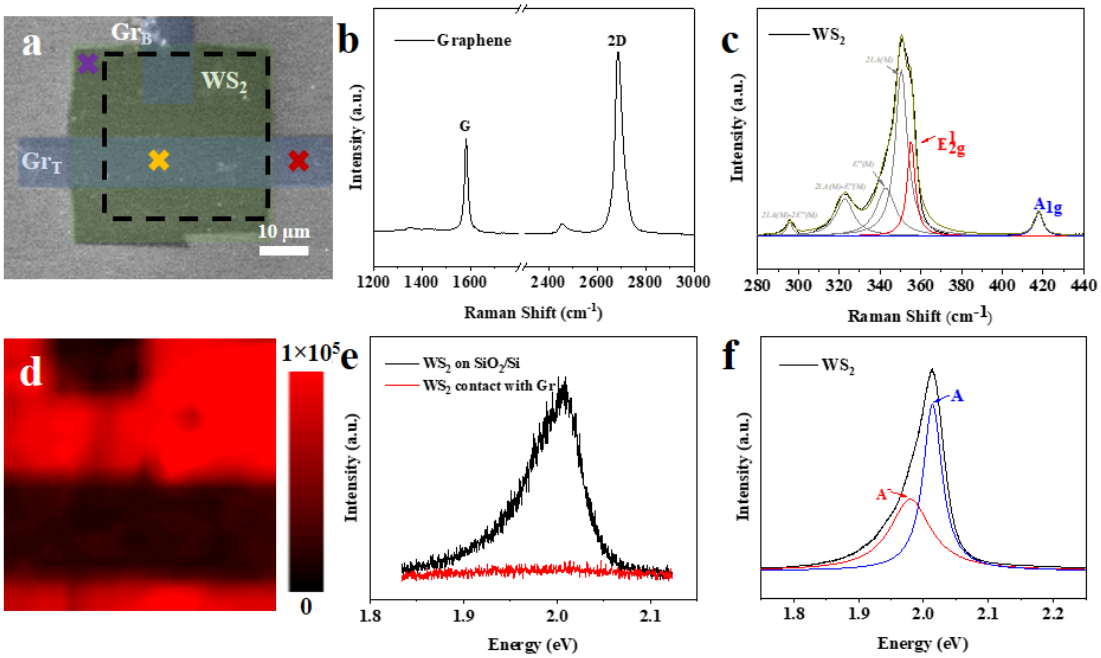


Figure 5.2 Optical characterization of the asymmetric device. (a) SEM image of a typical asymmetric lateral device. (b) Raman spectrum of the graphene electrode, obtained from the red cross in (a). (c) Raman spectrum of the semiconducting WS_2, obtained from the purple cross in (a). (d) PL integrated intensity mapping from the black dashed box in (a). (e) PL spectra of the WS square: black for WS_2 on SiO_2/Si and red for WS_2 on graphene. (f) PL spectrum of WS_2 with two fitted Lorentzian peaks representing exciton emission (A) and negative trion emission (A^-).

5.2.3 Photodetecting Characterization

The atomic models of the asymmetric and symmetric structures are displayed in **Figure 5.3**a,b. I conducted I-V measurements under different laser powers on these two devices to show the different performances. As shown in **Figure 5.3**c,d, probe tips were used to penetrate into the bond pads. In the Gr_B-WS_2-Gr_T device, the top graphene serves as the drain electrode. As for the Gr_B-WS_2-Gr_B, either graphene ribbon can be the drain as the two ribbons are in the same environment. A clear difference can be observed in the I-V characteristic curves of the two structures, as displayed in **Figure 5.3**e,f. For the Gr_B-WS_2-Gr_T structure, there is an obvious current rectification where

the current is easier to flow through under a positive bias, behaving like a diode, However, in the Gr_B-WS_2-Gr_B one, the current can flow in both directions symmetrically.

This difference can be explained by introducing Schottky barriers formed between $graphene_{bottom(top)}$ and WS_2. The Schottky-Mott rule is expressed as:

$$\emptyset_{SB} = \emptyset_M - \chi_S \qquad (5.1)$$

where $\emptyset_M$ is the work function of the metal electrode and χ_S is the electron affinity of the semiconductor. In theory, the estimated work function of graphene is 4.6 eV and the electron affinity of WS_2 is 4.0 eV[168]. Therefore, the height of the Schottky barrier is estimated to be 0.6 eV. These values are all under static conditions, and will vary by the internal and external influences. In reality, as for the Gr_B-WS_2-Gr_T device, the top graphene electrode is between the WS_2 and air while the bottom one is between the SiO_2/Si substrate and WS_2. The bottom and top graphene electrodes are thus under different dielectric environments, resulting in a doping level difference in graphene. This causes an initial Schottky barrier difference between Gr_B-WS_2 and Gr_T-WS_2 interfaces. This barrier inhibits the injection of electrons through thermionic emissions. For the asymmetric device, bottom graphene is less p-doped and thus it is easier for electrons to migrate from the bottom graphene to WS_2 because of the lower Schottky barrier. As a result, the measured current is much higher under a positive bias, leading to an asymmetric behaviour. In contrast, in the Gr_B-WS_2-Gr_B structure, two graphene electrodes are under the same environment. Therefore, a symmetric behaviour is expected. Their corresponding band diagrams are shown in **Figure B1**.

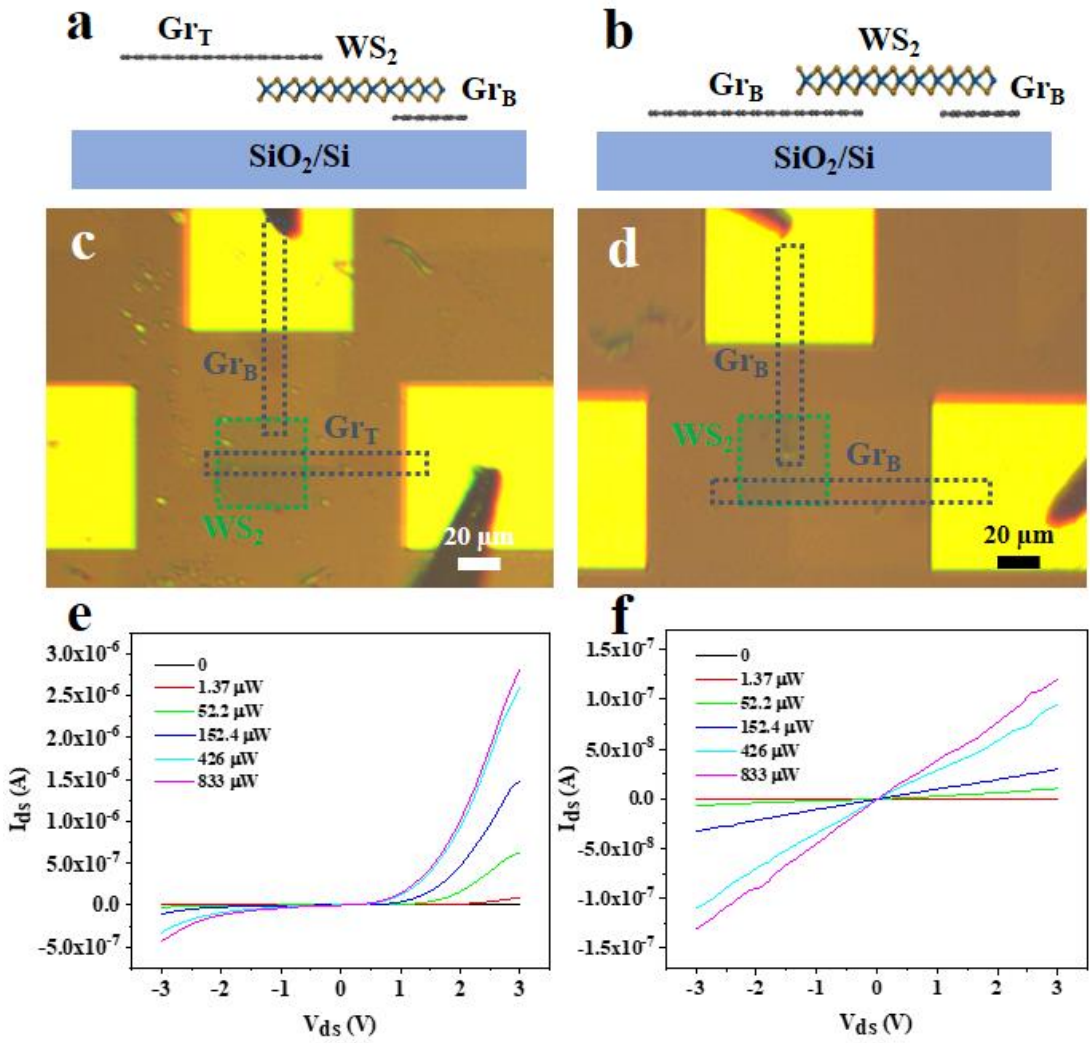


Figure 5.3 Comparison between the Gr_B-WS_2-Gr_T and Gr_B-WS_2-Gr_B structures. (a-d) Atomic models and corresponding optical images of the asymmetric and symmetric structures, respectively. (e,f) Corresponding output I_{ds}-V_{ds} curves of the two structures under different laser powers. The Gr_B-WS_2-Gr_T device shows a rectification behaviour while the Gr_B-WS_2-Gr_B device performs symmetrically.

In these two structures, both the on-current and off-current go up with an increasing laser illumination. This can be explained by the photogating mechanism. It is recorded that the Schottky barrier formed at the heterojunction can hugely impact the resistance of the metal-semiconductor contact[169]. As more electrons are excited, they migrate to the graphene and contribute to the current while holes are localized

because of the existence of the trap states. These trap states can be vacancies, defects or surface adsorbates. The accumulated holes act as a positive gate and lead to an increase in the Fermi level of graphene. This lowers down the SBH between graphene and WS_2, which further helps the re-injection of electrons. The same explanation has also been documented in some prior papers where the Schottky barrier of Gr-TMD can be modulated by tuning the work function of graphene[118,159,162,170,171,172,173,174]. The same explanation is thus expected here.

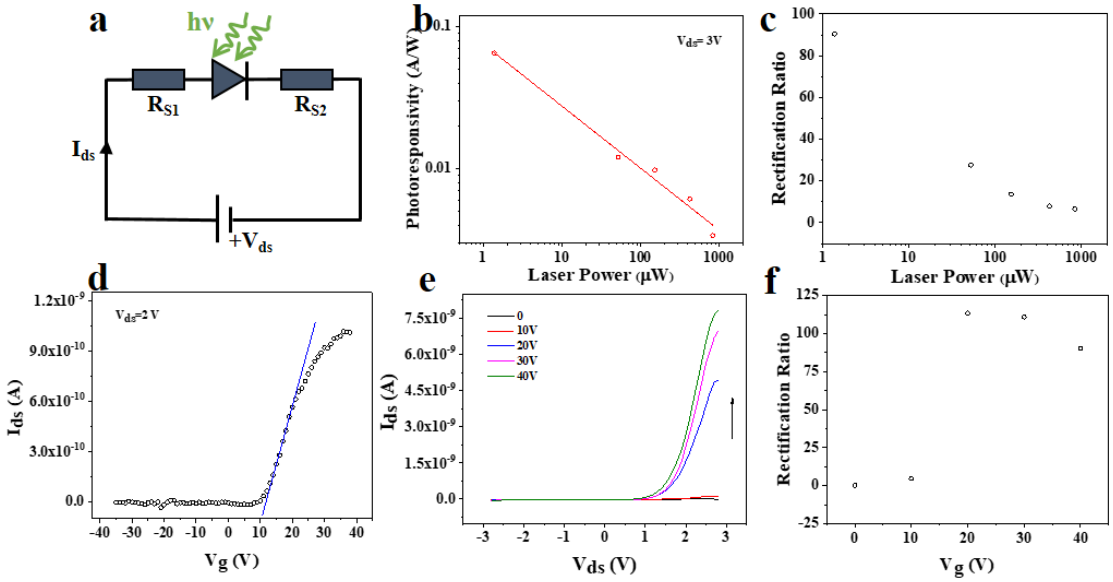


Figure 5.4 Electrical characterization of the Gr_B-WS_2-Gr_T structure. (a) Equivalent circuit model of the device. R_{s1} and R_{s2} represent the series resistances contributed by the top and bottom graphene ribbons, respectively. (b) Dependence of responsivity on the laser powers with 3V source-drain bias. (c) Rectification ratio at V_{ds}=±3 V under different laser powers. (d) Output I_{ds}-V_g curve of the device, showing an N-type property. (e) Output I_{ds}-V_{ds} curves under different back gates showing the rectifying behaviour. (f) Rectification ratio at V_{ds}=±3 V under different back gates.

More detailed optoelectrical studies were then conducted on the Gr_B-WS_2-Gr_T structure. The asymmetric Gr_B-WS_2-Gr_T structure can be considered as a resistor, a diode and another resistor in series, as demonstrated in **Figure 5.4**a. The symbols of R_{S1} and R_{S2} represent the series resistances contributed by the top and bottom graphene

ribbons. The photocurrent was extracted and the corresponding photoresponsivity was plotted with a function of the laser powers. The photoresponsivity (R) is defined as:

$$R = \frac{I_{Photo}}{P_{laser}} \qquad (5.2)$$

where I_{photo} is the photocurrent and P_{laser} is the laser power. As displayed in **Figure 5.4**b, this power dependence trend of Gr_B–WS_2–Gr_T photodetector's photoresponsivity decreases monotonously with increasing incident powers, suggesting the photo absorption saturation in monolayer WS_2. A maximum photoresponsivity of 0.065 A/W is calculated under +3 V applied bias with an illumination power of 1.37 μW.

In **Figure 5.4**c, it is found that the laser illumination has an evident influence on the rectifying performance of the device. The rectification ratio (RR) defines as:

$$RR = |\frac{I_{+V}}{I_{-V}}| \qquad (5.3)$$

which means the ratio between the currents for the same bias but for the opposite direction. The rectification ratio decreases apparently from 90 to 6 with an increase of the laser power. This indicates that the illumination could result in a decrease in the difference between Schottky barriers between Gr_B-WS_2 and Gr_T-WS_2. This is because the electrons transfer to the graphene will reduce its work function, or increase the Fermi level in other words. With an increasing illumination intensity, more electrons are excited and transfer to graphene, resulting in a decrease in the barrier height. The impact of illumination on the barriers of Gr_B-WS_2 and Gr_T-WS_2 is of different degrees, with the height difference narrowed down.

I also performed the gate sweep to the sample, as shown in **Figure 5.4**d. The

transfer curve shows a typical N-type behaviour with a threshold voltage of ~10 V. This is because of the contact formed between graphene and WS_2. The rectification ratio is tunable under the back-gate voltage. A positive back-gate voltage will increase both the graphene Fermi level as well as decrease the conduction band of WS_2. When the gate voltage is 0 or 10 V, the SBHs for both Gr_B-WS_2 and Gr_T-WS_2 are high, so the channel is not conductive for both directions. The small mismatch leads to low rectification ratios. When the gate voltage reaches 20 V, the channel for the positive direction first becomes conductive due to the lower SBH for Gr_B-WS_2. This results in a huge increase in the positive current, while the opposite current only changes a little. Therefore, the rectification ratio under this gate voltage shows the largest value (~100). When the gate voltage is above 20 V, both the SBHs for Gr_B-WS_2 and Gr_T-WS_2 are further lowered so that the channel becomes conductive for both directions. The mismatch gradually becomes smaller, leading to decreased rectification ratios.

The rectification ratio in our device is among the general value (10-10^4) compared with the other 2D Schottky junctions. For the 2D Schottky diode in superior cases, a value of 10^5 to 10^6 can be achieved. This ultrahigh value is usually obtained by the chemical doping of the surface or employing two different metal electrodes, such as Au-WS_2-graphene or Au-MoS_2-1T'$MoTe_2$[163,168]. However, for the structure in this study, an intrinsic doping caused by the dielectric environment is utilized to obtain different doping levels of graphene.

5.2.4 Light-emitting Characterization

The asymmetric device can also act as an LED. The red EL signal was collected by a homemade spectrometer system with a CCD camera to record the emission. A

rather high voltage is selected to operate the device because the long channel length leads to a large resistance in the device. The way to apply the voltage on the device is to first exert a negative gate voltage (-30 V), and then apply a constant bias voltage (+25 V). In this case, the decrease of the Fermi level of graphene can further facilitate the injection of holes to WS_2. This increases the amount of holes that can recombine with the injected electrons later.

As shown in **Figure 5.5**a, the device generates a strip-shaped red EL, which is located in the junction area. Its corresponding intensity profile, shown in **Figure 5.5**d, has a bell-shaped curve and can be regarded as a Gaussian distribution. **Figure 5.5**b shows the time-dependence of the current during the measurement. The current flowing through the device first rises rapidly, reaching 1×10^{-4} A in a second. As time goes on, it then drops gradually in the following 16 s. The average current during this period is calculated to be 2.16×10^{-5} A. This suggests a degradation in materials as carriers are laterally injected into the semiconducting WS_2 which is exposed to air and thus oxidizes easily, making it vulnerable under the operational conditions of a constant high bias. Encapsulating the device with few-layered h-BN can help protect the device from degradation in the future. As the emission video and the corresponding spectrum cannot be recorded at the same time in the existing experimental condition, I repeated the same electrical measurement on another device to collect the spectrum. As demonstrated in **Figure 5.5**c, the EL peak collected for an accumulation time of 30 s is beyond the capture range due to the very strong signal.

The mechanism of the strong EL emission is elaborately explained in **Figure 5.5**e,f. Primarily, our device has a metal-semiconductor-metal structure and Schottky

barriers exist at the interfaces of the graphene-WS_2. The current flowing through the device is generated by the thermionic emission. The Fermi-level of graphene is closer to the conduction band of WS_2. Therefore, when the bias voltage is low, the current is very small because limited thermionic emission occurs which produced a small amount of the electrons. Only electrons are injected from the graphene ribbons to the WS_2. However, under a high bias voltage, some minority holes are also generated by one electrode which can then recombine with electrons from the other electrode and gives rise to the EL emission[141]. Additionally, there are some local p-type dopants in the WS_2, either defects or the adsorbates from the air or the photoresists. The interactions between these dopants and the electrons can also attribute to the EL signal.

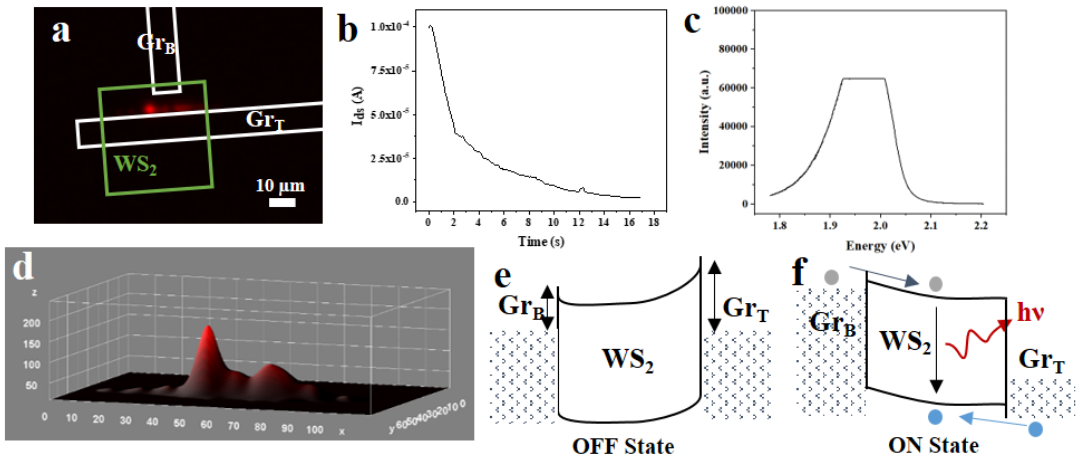


Figure 5.5 Electroluminescence of the asymmetric structure. (a) Optical image of the red emission. The white boxes represent graphene ribbons while the green box is the WS_2 square. (b) Corresponding output I-t curve of the device. (c) Recorded EL spectrum of another device under the same experimental condition. The signal is very strong, beyond the capture range. (d) Intensity profile of the red emission in (a). (e,f) Band diagrams of the device under non operating state and EL emission state. The grey and blue dots represent electrons and holes, respectively. The grey and blue arrows indicate the injection of electrons and holes. Under a high bias, both electrons and holes are injected and then recombine to generate the emission.

Previous studies have shown that the EL emission preferentially occurs in the defect regions of the materials. These defects can either be grain boundaries, vacancies and dopants[141]. **Figure 5.6** shows the time-dependence of the EL emission in the WS_2 region under the electrical measurement in **Figure 5.5**b. The video started recording ~2 s prior to the voltage apply, and the source meters took another ~2 s to reach the target voltage value. With the applied persistent voltage, the device starts the emission on the 5 s. The emission gradually achieves its best performance and then starts to degrade, evolving from a dot to a strip, and back to a dot. The total time of the emission is ~15 s. It is interesting that although the flowing current almost monotonously decreases, the as-produced EL signal is not the same.

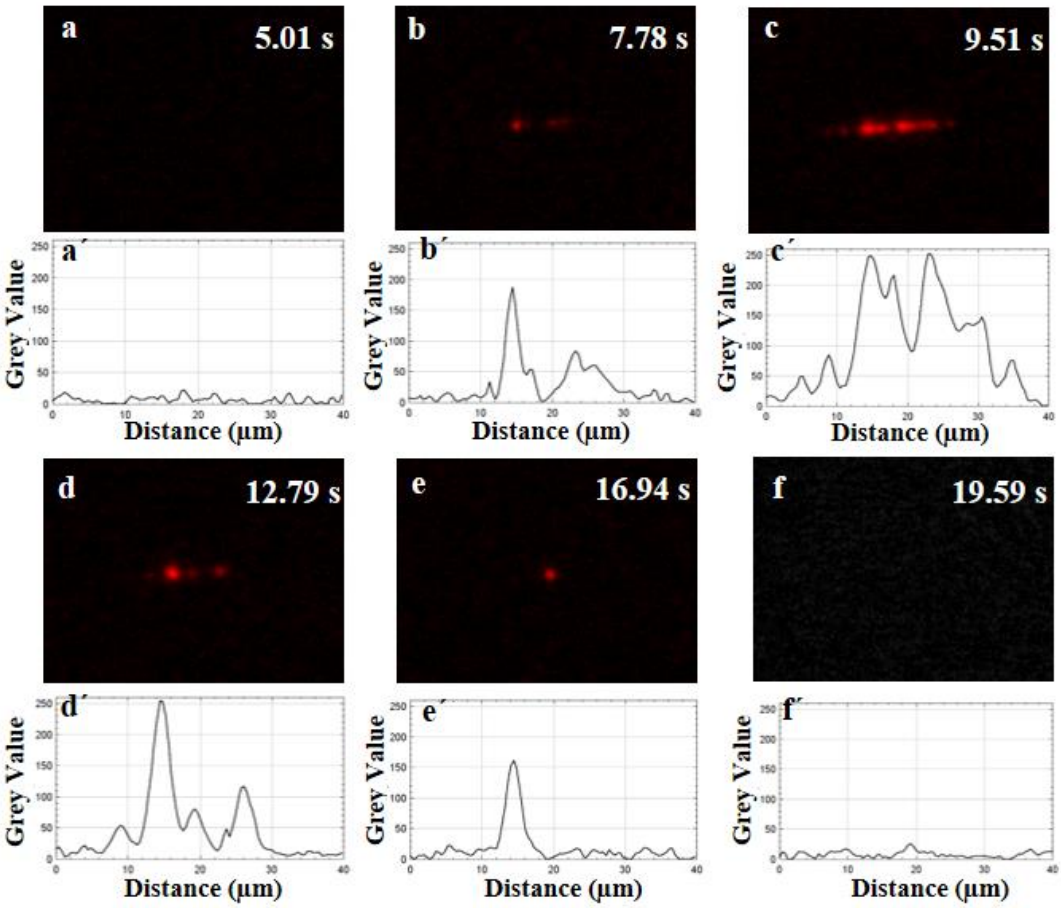


Figure 5.6 Time-dependence of the EL emission in the junction region. (a-f) Optical images showing the evolution of the EL emission and (a'-f') its corresponding intensity line profiles. It shows that the EL starts, grows from a dot towards a strip, diminishes from a strip towards a dot, and finally fades away.

In the lateral geometry, the emission area is spatially confined at WS_2 region between the two graphene electrodes. However, in various devices, the position of the emission spot can be different. The same electrical measurement is then repeated on three more devices to show this location variations. As demonstrated in **Figure 5.7**, the EL emissions of different devices not only have variations in positions, but intensities as well. This can be caused by many factors, such as the intrinsic defects in CVD-synthesized WS_2, doping during the stacking process and also molecules in air.

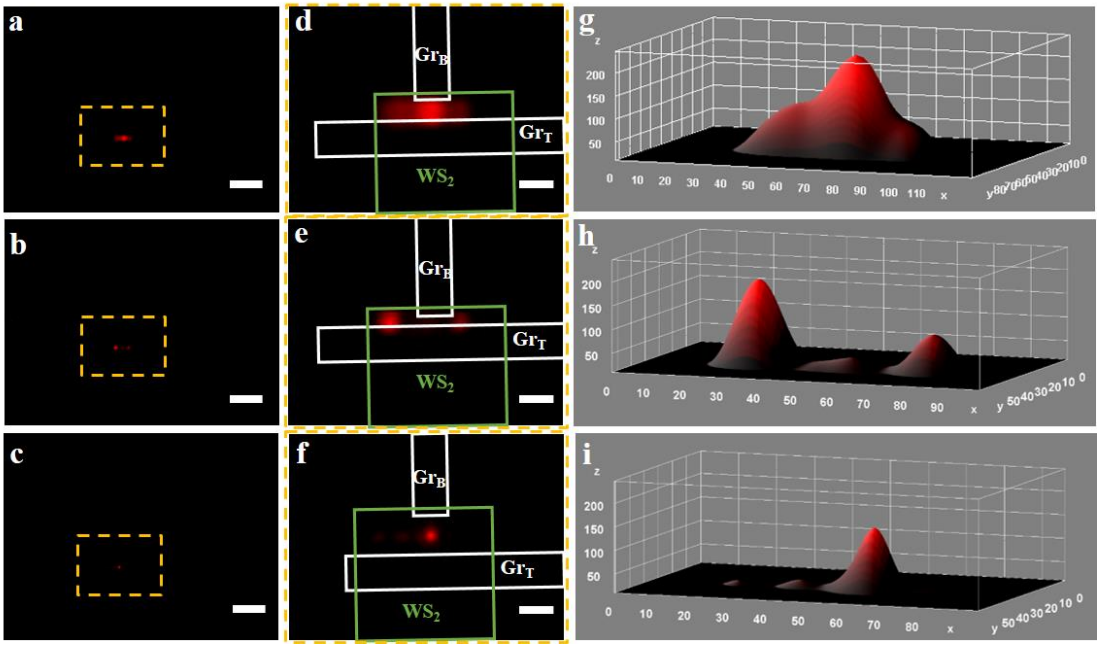


Figure 5.7 EL signals in various asymmetric devices. (a-c) Optical images of EL from three different devices under the same experimental conditions. Scale bar: 50 μm. (d-f) Enlarged optical images of the yellow dashed boxes in (a-c). Scale bar: 10 μm. (g-i) EL intensity profiles of the EL emissions in (d-f).

For a further comparison, the vertical structure Gr/WS_2/Gr was also constructed, as shown in **Figure B2**a,b. It is interesting to notice that the vertical one exhibits a quite different EL mechanism as the lateral one does. In a vertical structure, WS_2 is sandwiched between two graphene ribbons and thus the charge carriers migrate by the tunnelling effect. As a result, a larger current is expected in the vertical structure if the same bias voltage is applied to the device. **Figure B2**c shows the colour map of the EL spectra as a function of the source-drain bias. The results indicate that the switch point for triggering EL in a vertical structure is much smaller, less than 6.5 V at a forward bias, which confirms that electrons and holes are easier to inject and combine.

Unlike the lateral structure, the vertical device shows a charge neutrality point (V_{CNP}) in its transfer curve. As shown in **Figure B2**d, the transfer curve owns a V-shape, very similar to that of pristine graphene on a SiO_2/Si substrate. Normally the

graphene shows a p-doped behaviour on the SiO_2/Si substrate. The V_{CNP} of the device is located around 18 V, in the range of the previous studies. The back gate changes the EL intensity of the device simply by controlling the value of the current flowing through the device. As displayed in **Figure B2**e, two curves show good agreement where a larger current causes a stronger EL. Besides, they also exhibit a V-shape with the lowest point in the range of 0 to 20 V, in accordance with the transfer curve of the device. Its EL intensity characteristics under a constant bias of 25 V but negative back-gate voltage of -30 V, switched on and off over several cycles, are also investigated. As shown in **Figure B2**f, ten EL spectra were taken, with the back gate applied intermittently. The time interval between each two measurements is 1 min. The grey dashed line indicates the EL average intensity value under -30 V back-gate voltage, and the black dashed line marks the weaker EL emission when no back-gate voltage is applied. In spite of the slight difference in the peak intensity under the same condition, the overall status is quite clear. It is obvious that the EL emission under -30 V back gate is much stronger than that under zero back gate, with the same bias applied.

When the back-gate voltage is smaller than V_{CNP}, holes are the majority carriers in the device. Similarly, when the back-gate voltage is larger than V_{CNP}, electrons are the majority carriers. The device shows the largest resistivity at V_{CNP}. The more the difference between the Vg and V_{CNP}, the more holes/electrons will be induced and attributed to the current value, which further leads to an increased EL emission.

5.3 Conclusion

To conclude, I have investigated the graphene-WS_2 van der Waals Schottky heterojunction. CVD-grown materials are used to fabricate the Gr_B-WS_2-Gr_T structure. It shows that the device behaves as a diode which is attributed by the different SBHs of Gr_B-WS_2 and Gr_T-WS_2. This is evidenced by constructing the symmetric structure, Gr_B-WS_2-Gr_B, where the two graphene ribbons are in the same dielectric environment. It is found that both the laser power and the back-gate voltage can tune the rectification behaviour of the device. Its light-emitting performance is further studied. A constant bias voltage applied to the device causes a strong EL in the junction area, with an average current of 2.16×10^{-5} A. This work contributes to the current understanding of the 2D metal−semiconductor heterojunction and offers an idea to obtain all-2D Schottky diodes by retaining the ultrathin device concept.

5.4 Contribution Statement

Linlin Hou helped with some of the data analysis of the EL. Dr. Viktoryia Shautsova helped provide the graphene ribbons for the fabrication of symmetric devices.

Chapter 6 Single- and Multi-Stacked Heterostructures

6.1 Introduction

As I have mentioned before, TMDs exhibit strong light−matter interactions, which makes them excellent candidates for the ultrathin optoelectronic devices[175]. 2D materials own a rather high light absorption if considering their thickness. However, it is yet far from ideal and there is plenty of room to improve the performance. The basic principle to enhance the absorption of the device is to reduce the reflection and transmission of light from the materials. For example, common ways to confine the light in the materials involve using single/double reflective mirrors, creating nanocavities and patterning plasmonic 2D materials[176]. Despite these new designs, several problems are found in these structures such as the large thickness, complex fabrication and high narrowband.

To solve these problems, one can create an all-2D device by stacking several layers in the vertical direction to create VLHs, which have strong interlayer coupling between each 2D material due to the large surface area contact. Moreover, individual devices can be stacked on top of each other, to result in an increased total light absorbed or emission. For example, Withers et al. employed multiple QWs stacked in

series, which increases the overall thickness of the tunnelling barriers and enhances the probability for injected carriers to recombine. This leads to an enhanced QE of up to 8.4%[129].

To potentially increase the overall photosensitivity, one can stack individual photodetectors on top of each other. In this work, by utilizing graphene as a metallic electrode and TMDs as the active semiconductor material, two kinds of vertical stacked devices are fabricated: single-stacked heterostructure (SSH) Gr/WS_2/MoS_2/Gr and multi-stacked heterostructure (MSH) Gr/WS_2/MoS_2/Gr/MoS_2/WS_2/Gr. These all-2D stacks are a new class of optoelectronic devices that are ultrathin, flexible, and with potential ultrahigh photon-charge exchange efficiencies. All the 2D materials are grown into continuous films and then patterned to building blocks for the stacking process. Their optoelectronic performances under illumination are then investigated and compared. This study brings forward a novel concept of multi-stacked architectures which extends the current research range and paves up ways for the high efficiency yet ultrathin photodetectors in the future.

6.2 Results and Discussions

6.2.1 Fabrication of the Single-Stacked Heterostructure

Considering the complexity of the structures, it is not feasible to use randomly distributed TMD domains because the structures require both WS_2 and MoS_2 cover the overlapping area formed by the graphene cross-bar. Therefore, to fabricate the device, all the 2D materials used are first grown into continuous films on a large scale. Their corresponding SEM images are shown in **Figure 6.1**a-c. The films are patterned into building blocks via EBL, and a marker-assist-aligned stacking method is used to assemble them, forming the target structures[167].

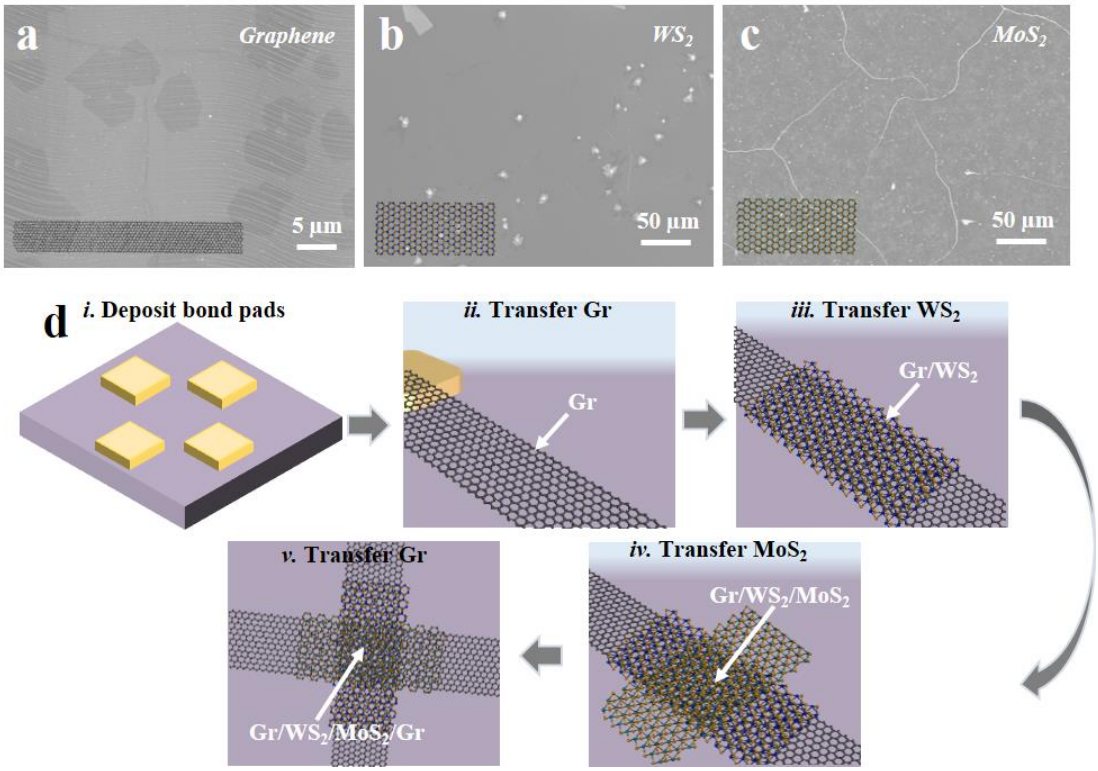


Figure 6.1 Demonstration of the single-stacked heterostructure. (a-c) SEM images with atomic models at the bottom-left corner of three kinds of 2D materials used for the device fabrication. They are graphene grown on the copper foil via CVD, WS_2 grown on the SiO_2/Si substrate via CVD and MoS_2 grown on the glass via sulfurization, respectively. (d) Fabrication steps for creating the single-stacked heterostructure. Step i: Deposit Cr/Au (10 nm/70 nm) as bond pads on the SiO_2/Si substrate. Step ii: Transfer a piece of graphene film and pattern it to ribbons as electrodes. Step iii: Transfer pre-patterned WS_2 squares onto bottom graphene electrodes. Step iv: Transfer pre-patterned MoS_2 squares onto the Gr/WS_2 stacks. Step v: Transfer another batch of graphene electrodes onto the Gr/WS_2/MoS_2 stacks. This forms the single-stacked heterostructure.

The graphene ribbon is designed in 10 μm width as before, and the WS_2 and MoS_2 squares are in a dimension of 30 μm × 40 μm. **Figure 6.1**d presents the fabrication process for the single-stacked structure. In details, Cr/Au (10 nm/70 nm) are first deposited as bond pads on the SiO_2/Si substrate. A piece of graphene film is then transferred and EBL is used to pattern it to ribbons. Subsequently, prepatterned WS_2 and MoS_2 squares are transferred onto the graphene with the aid of the aligned stacking

technique. Finally, another batch of graphene ribbons are transferred on the WS_2 and MoS_2, perpendicular to the first graphene ribbon, forming a cross-bar structure. By now, the fabrication of the single-stacked device is completed.

6.2.2 SEM, Raman and PL Characterization

SEM, Raman and PL spectroscopy are used to characterize the layer number and strain of 2D crystals after the fabrication. **Figure 6.2**a shows the SEM image of a typical single-stacked device where WS_2/MoS_2 is sandwiched between two graphene ribbons, forming cross-bar structure. The graphene is characterized by Raman and its spectrum is displayed in **Figure 6.2**b. As it presents, the positions of G and $2D$ peaks are 1588 cm^{-1} and 2682 cm^{-1} with corresponding FWHMs of 27.8 cm^{-1} and 42.3 cm^{-1}. The area and intensity ratios of $2D/G$ is 2.4 and 1.5, respectively. These indicate the graphene is monolayer with an estimated doping level of ~5×10^{12} cm^{-2} [148]. The small D peak at 1341 cm^{-1} reflects its high quality[146]. As mentioned before, there are some thicker regions in graphene but this does not make a big influence to the device performance.

The Raman and PL spectra of WS_2, MoS_2 and their stack are also studied, shown in **Figure 6.2**c,d. As for the WS_2, the E_{2g}^1 and A_{1g} peaks are located at 347 cm^{-1} and 415 cm^{-1}, respectively. The difference of the two modes is 68 cm^{-1}, consistent with those for bilayer WS_2[177]. In the stack, the E_{2g}^1 mode of WS_2 is stiffened, with its peak at 349 cm^{-1}, while the A_{1g} mode remains unchanged. The A_{1g} mode, corresponding to the out-of-plane vibration of sulphur atoms, can be used to analyse the doping level. The unchanged position of the A_{1g} mode shows the doping level of the WS_2 remains as before. The E_{2g}^1 mode represents the in-plane vibration of tungsten and sulphur

atoms, and is sensitive to the lattice strain. The stiffening of the E^1_{2g} mode in the stack indicates a lattice strain is introduced. Bilayer MoS_2 is confirmed with typical in-plane/out-of-plane phonon vibration modes located at 382 cm^{-1}/404 cm^{-1}, with the frequency difference of 22 cm^{-1}. It is interesting to find that both the E^1_{2g} and A_{1g} modes of MoS_2 are softened in the stack, with a shift of 2 cm^{-1}. This indicates a tensile strain in MoS_2.

Compared with the WS_2, there is an obvious PL signal drop at the WS_2/MoS_2 heterolayer region (only ~15% signal of that of WS_2), suggesting a suppressed recombination of photoexcited electron-hole pairs within the stack due to the interlayer charge transfer[178]. However, the PL signal of the stack is still stronger than that of the bilayer MoS_2, due to the indirect band gap of bilayer MoS_2. Such results imply a strong interlayer coupling between WS_2 and MoS_2.

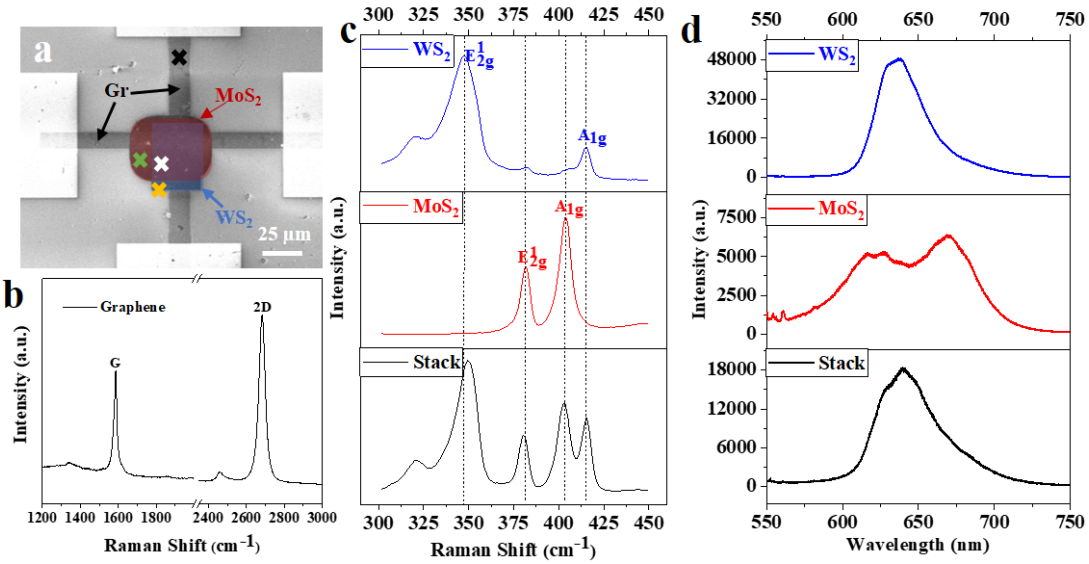


Figure 6.2 Optical characterization of the single-stacked heterostructure. (a) SEM image of a typical single-stacked device, where WS_2/MoS_2 is sandwiched between two graphene ribbons. (b) Raman spectrum of the graphene electrode, obtained from the black cross in (a). (c) Raman spectra of WS_2, MoS_2 and their stack, obtained from the yellow, green and white crosses in (a), respectively. The spectrum of the stack contains the Raman modes of both WS_2 and MoS_2. (d) PL spectra of WS_2, MoS_2 and their stack.

6.2.3 Limitation of the Single-Stacked Heterostructure

As reported in some previous work, utilizing bilayer WS_2 or MoS_2 to replace the monolayer ones leads to an increase in the photocurrent due to the larger absorption[78,161]. In spite of the linear scaling in absorption versus number of layers for 2D materials up to few layers, the value of optical absorption in the bulk is different[175]. This indicates that after increasing the layer number of the 2D materials to a specific value, the performance of the material will be like a bulk. For TMDs, this linear dependence only retains up to 3-4 layers[23]. Keeping adding the layers of TMDs beyond this value will not help the light absorption further. Additionally, the equation of the direct tunnelling current I_{DT} can be expressed as:

$$I_{DT}(V) = \frac{A_{eff}\sqrt{m\varphi_B}e^2V_{ds}}{h^2d}\exp[\frac{-4\pi\sqrt{m^*\varphi_B}d}{h}] \qquad (6.1)$$

where A_{eff}, φ_B, e, m, m^*, d and h are the effective contact area, barrier height, electron charge, free electron mass, effective electron mass, barrier width (WS_2/MoS_2 thickness) and Plank's constant, respectively[179]. It shows that the direct tunnelling current (I_{DT}) is in inverse proportion to the barrier width (d). Therefore, as the thickness of the device becomes larger, it will be more difficult for the electrons to tunnel through from one electrode to the other. To solve the limitations, one possible way is to construct the multi-stacked architecture where a second current channel is created.

6.2.4 Demonstration of the Multi-Stacked Heterostructure

As shown in **Figure 6.3**, there are two different heterostructures: SSH of Gr/WS_2/MoS_2/Gr and MSH of Gr/WS_2/MoS_2/Gr/MoS_2/WS_2/Gr. The schematics in **Figure 6.3**a,b illustrate these two configurations for comparison. In the single-stacked device, two graphene ribbons are placed orthogonally to each other, forming the cross-bar structure. One ribbon serves as the source while the other is the drain. Sandwiched between them is the WS_2/MoS_2 vertical stack which has a type-II band alignment. This structure is a typical individual photodetector which has been already explored in *Chapter 4*. However, it has been reported that the absorption of WS_2(1L)/MoS_2(1L) stack is only about 10.8%[161,175], indicating the majority of the incident light is transmitted. To potentially increase the overall photosensitivity, a new type of photodetectors is designed and fabricated by repetitively stacking another individual photodetector on top of the existing one, forming the multi-stacked structure. In the multi-stacked device Gr/WS_2/MoS_2/Gr/MoS_2/WS_2/Gr, one more pair of MoS_2/WS_2 stack is transferred to increase the absorption of light. Another graphene ribbon is also transferred as the electrode. Here, the bottom and top graphene electrodes are both connected to the source while the middle one acts as the drain.

Their corresponding band diagrams are further depicted in **Figure 6.3**c-f. The photocurrent generation for this type of structure without the external bias is based on the photovoltaic effect. Under a 532 nm light illumination, WS_2/MoS_2 stack is excited with electron-hole pairs in both layers. The electrons then flow from WS_2 to MoS_2 due to the type-II energy band and subsequently collect by the graphene electrode. Here, the tunnelling barriers formed between graphene, WS_2 and MoS_2 play a minor role in determining the direction of the electron transfer. It is the band offset formed by the

WS_2/MoS_2 stack that decides the electrons flow from WS_2 to MoS_2 in a zero bias condition[161].

By adding another MoS_2/WS_2 stack on the existing device as the photoabsorber and graphene as the electrode, a second current channel is thus created which will contribute to the overall photocurrent. The total amount of light absorbed by the stack is nearly doubled (or less to be specific if considering that graphene absorbs 2.3% of light so the bottom device cannot receive as much light as the top one). As a result, a higher photodetection efficiency should be achieved using this vertically spaced graphene electrodes with semiconductors in the middle. The photocurrent can be further enhanced by applying an external voltage bias, as shown in **Figure 6.3**e,f.

To stack the second individual device, another batch of MoS_2, WS_2 and graphene are successively transferred to the existing individual device one-by-one. This forms the final target structure of MSH. The corresponding schematic diagrams and optical images of the stacking process from the SSH to MSH are displayed in **Figure 6.4**, where the overlapping region shows a more distinct colour because of the large thickness.

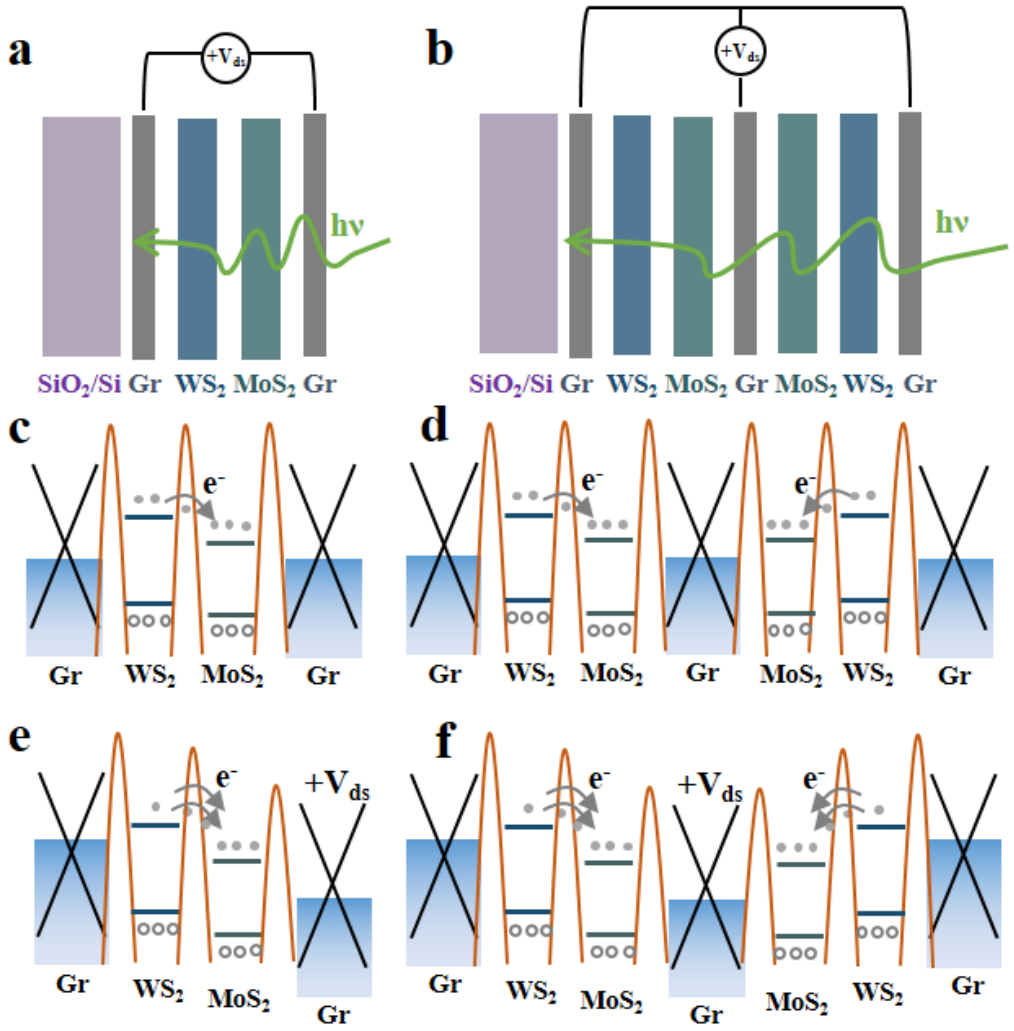


Figure 6.3 Demonstration of the single- and multi-stacked heterostructures. (a,b) Schematics of the single- and multi-stacked vertical heterostructures: Gr/WS_2/MoS_2/Gr and Gr/WS_2/MoS_2/Gr/MoS_2/WS_2/Gr. The green curvy arrows indicate the illumination by laser. (c,d) Corresponding band diagrams under zero source-drain voltage. The grey arrows demonstrate the photoexcited electrons transfer. The orange lines indicate the tunnelling barriers between each 2D layered materials. In the single-stacked configuration, the electrons flow from WS_2 to MoS_2. As a contrast, in the multi-stacked configuration, a second current channel is created, so the overall photocurrent is increased. (e,f) Band diagrams of the two stacks under positive source-drain voltage, where more electrons are generated because the external electric field facilitates the transfer of electrons.

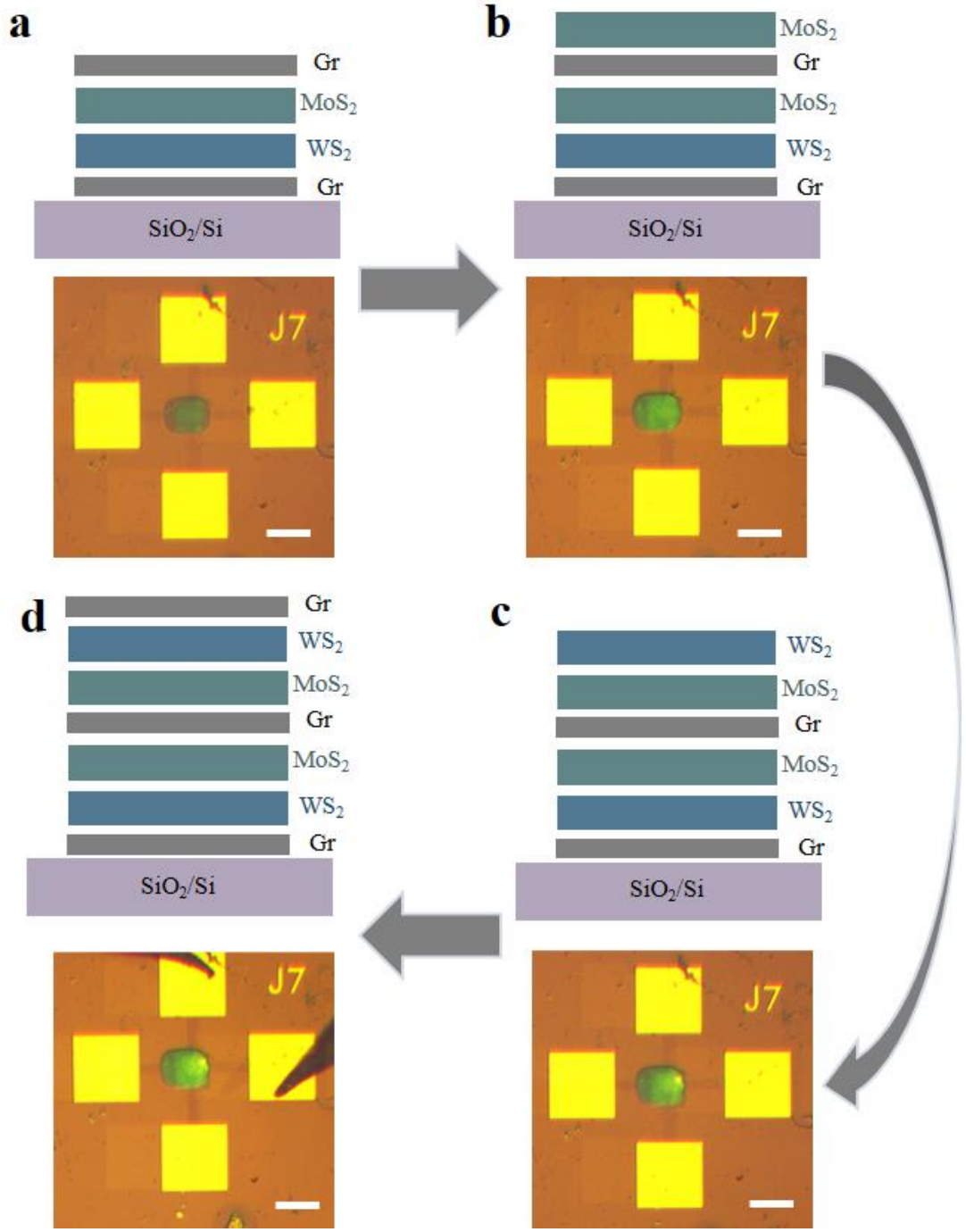


Figure 6.4 Fabrication steps for stacking the single- to multi-stacked heterostructures. Schematics with corresponding optical images of (a) single-stacked heterostructure Gr/WS_2/MoS_2/Gr, (b) Gr/WS_2/MoS_2/Gr/MoS_2, (c) Gr/WS_2/MoS_2/Gr/MoS_2/WS_2 and (d) multi-stacked heterostructure Gr/WS_2/MoS_2/Gr/MoS_2/WS_2/Gr. Scale bar: 50 µm.

6.2.5 Comparative Study on the Single- and Multi-Stacked Heterostructures

A 532-nm green laser is used to excite the WS_2/MoS_2 stack because the band gaps of WS_2 and MoS_2 locate in the red light range. **Figure 6.5**a shows the current-voltage curves under different illuminations in the single-stacked device. The current increases with the power of the illuminated light because it excites more electron-hole pairs. The curves do not pass through the origin of coordinate because of the aforementioned photovoltaic effect under zero bias voltage. The source-drain currents under a voltage of 0.05 V are then extracted under different laser powers, as shown in **Figure 6.5**b.

Their corresponding multi-stacked devices are then fabricated and measured. It is found that the dark current of the multi-stacked device is around twice compared with that of the individual device, shown in **Figure 6.5**c. This is because a second current channel is created in the multi-stacked device, and thus the dark current should be doubled. It should be pointed out that the merit of this multi-stacked device does not lie in the ON/OFF ratio (defined as I_{Photo}/I_{dark}), but the photoresponsivity. This is because the dark current will be doubled after the formation of the second channel but the photo absorbed by WS_2/MoS_2 is less than twice. In reality, there are variations among the device performance, so the actual increased photocurrent can sometimes be more than twice.

To calculate the photoresponsivity of the two types of devices, the following formula is used:

$$R = \frac{I_{photo}}{P_{laser}} \qquad (6.2)$$

where R is the photoresponsivity. I_{Photo} is the generated photocurrent and

P_{laser} is the laser power. As shown in **Figure 6.5**d,e, under a low laser power, there is an obvious increase in the photoresponsivity after stacking another device on top of the existing one, as what we expected. However, when the laser power increases, the difference in photoresponsivity between these two stacks become smaller. This phenomenon is probably due to the laser-induced thermal effect[30]. During the laser illumination, the SiO_2/Si substrate acts as a heat sink, the thermal conductivity of which is 5 orders of magnitude than that of air[122]. The laser power distribution conforms to the Gaussian profile. As the thickness of the stack increases, the heat generated in the top layer becomes more difficult to dissipate. Hu et al. show that a prominent temperature difference, approximate 400 K, exists between the top and bottom layers in a 10-layer MoS_2 under a fixed laser power of 2.5 mW[32]. Similar laser sensitivity has also been observed in monolayers. In case of monolayer WS_2 material, a laser exposure of 1.8 mW will result in the local material modification. Monolayer MoS_2 material requires much higher laser powers to induce observable material transformation, as high as 7.8 mW[31]. In our case, although the laser power is not that high, less than 1 mW, the exposure time (~30 s) is much longer if compared with the previous investigations, where the exposure time was controlled for less than 1 s per position. Additionally, our stack is fabricated by manually transfer, which means the distance between each adjacent layer is larger. Therefore, the laser-induced heat becomes more difficult to dissipate. This suggests that a low intensity of laser power is preferred in a multi-stacked device. The statistic results in **Figure 6.4**f are provided to compare the net photocurrents of the two structures. Five devices are measured, marked as (1−5). The grey dashed line indicates the average value of the net photocurrent of the SSH (9.648×10^{-8} A), while the red dashed line marks the average

value of the net photocurrent of the MSH (2.212×10^{-7} A). This shows the average net photocurrent of the MSH is around 2.3 times than that of the SSH. Optical images of the corresponding devices for the statistical data are displayed in **Figure C1**. In spite of the performance variations, the overall trend is clear where an obvious current increase is observed after the stacking of the second device on top of the existing one.

The corresponding equivalent circuit models of the single- and multi-stacked devices are presented in **Figure 6.6**. A current source along with a diode and resistor are used to represent the cross-bar area in a single-stacked device. The resistance induced by the graphene ribbons cannot be neglected, namely the series resistance. As for the multi-stacked device, it is illustrated by two devices in parallel, namely cell 1 and 2.

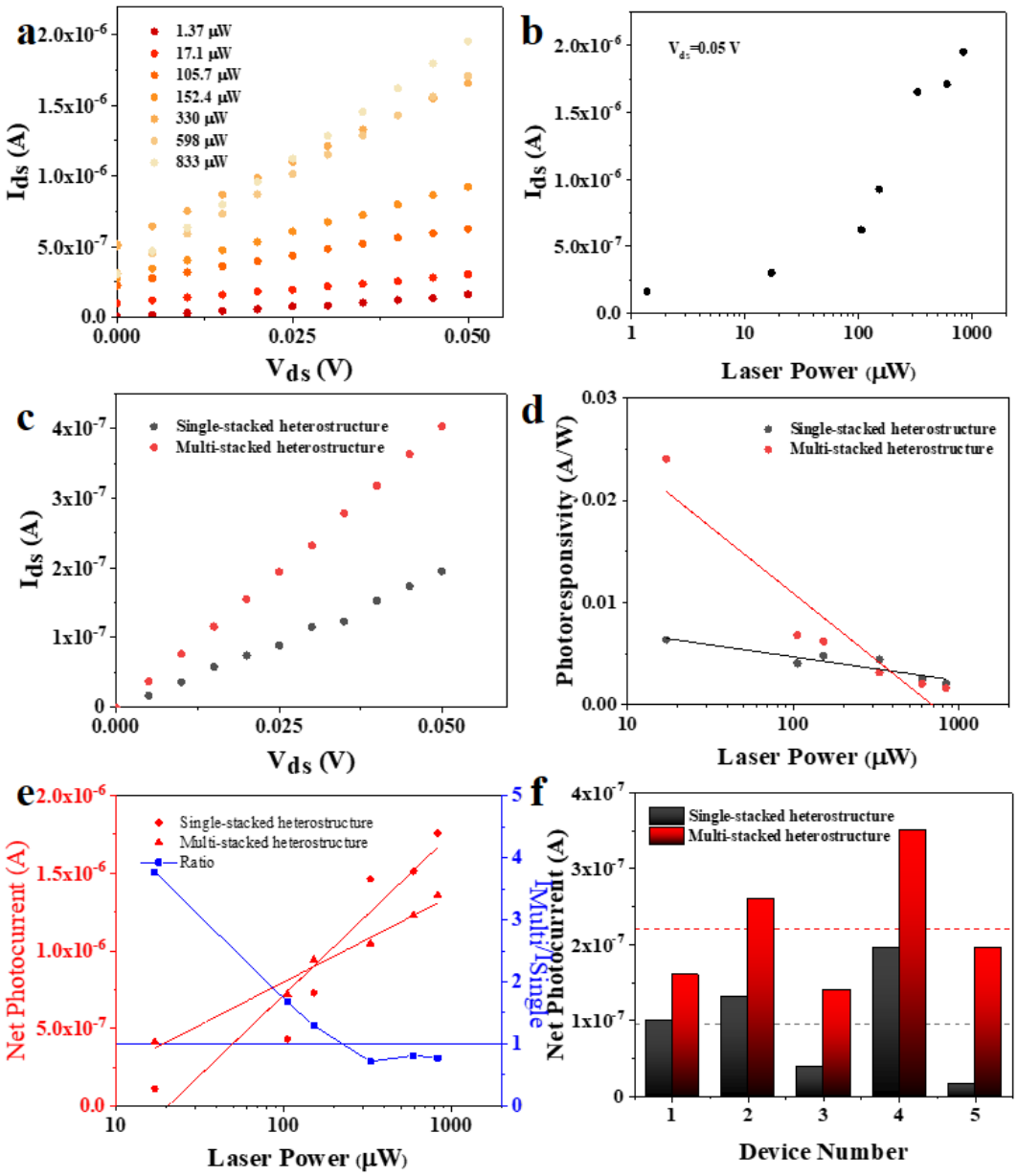


Figure 6.5 Optoelectrical characterization of the single- and multi-stacked heterostructures. (a) Output I_{ds}-V_{ds} curves of Gr/WS_2/MoS_2/Gr under different laser powers. (b) Dependence of I_{ds} on the laser powers in (a). (c) Comparison of the I_{ds}-V_{ds} curves of SSH and MSH under the dark condition. (d) Comparison of the responsivity of the two types of heterostructures under different laser powers. (e) Net photocurrents of the two types of heterostructures and their ratios. (f) Statistic results of the net photocurrents of the two types of heterostructures in different devices under a fixed laser power of 1.37 μW.

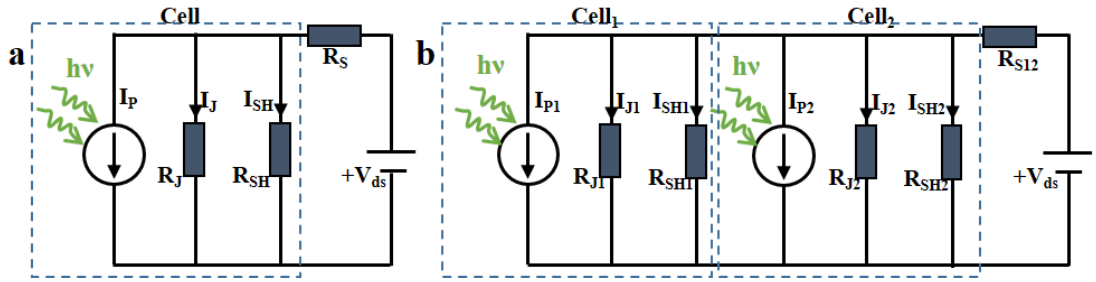


Figure 6.6 Equivalent circuit models of the single- (a) and multi-stacked (b) heterostructures. I_p is the photo-generated current. R_J, R_{SH}, R_S represent the junction, shunt and series resistances, respectively. The circuit in the blue dashed box can be considered as a cell. In a multi-stacked device, the two cells are in parallel, like a 'tandem cell'.

6.3 Conclusion

In summary, a new type of photodetectors has been demonstrated with an enhanced photodetecting efficiency by creating the multi-stacked heterostructure from various 2D crystals including graphene, WS_2 and MoS_2. All the 2D materials are grown into continuous films by bottom-up approaches and then patterned to building blocks for the stacking process. OM, SEM, Raman and PL are used to characterize the devices. A 532 nm green laser with different intensities of illumination is selected to study their optoelectronic performances. It is shown that the average net photocurrent of the multi-stacked heterostructure is around 2.3 times than that of the single-stacked one due to the increased light absorbed. This study brings forward a novel concept of multi-stacked architectures which extends the current research range and paves up ways for the high efficiency yet ultrathin photodetectors. For the future work, on the one hand, this concept can be expanded by using multiples of the same stacks, to further increase photosensitivity. On the other hand, this approach can be expanded to create single colour pixel 'red-green-blue' photodetector elements, where red, green and blue photodetector devices stacked in the appropriate order can fulfil full colour sensitivity.

6.4 Contribution Statement

Linlin Hou provided constructive help in device fabrication. Yang Lu provided the MoS_2.

Chapter 7 Conclusion and Future Outlook

In this final chapter, the main findings of my doctoral project are summarized. The prospects for the future trend and existing challenges are further discussed.

7.1 Thesis Summary

In *Chapter 4,* a novel method for assembling large-scale ultrathin all-2D device arrays were demonstrated. All the 2D materials used were grown into large continuous films, prepatterned with desired sizes, shapes, and spacings on a substrate and then transferred to the device substrate with aligned precision. In order to achieve long-range alignment across the wafer, interlocking marker pairs were designed to help guide the lateral accuracy and reduce rotational error. Over 200 Gr/MoS_2(2L)/Gr devices were produced with 2D periodic spacing on a 1 cm × 1 cm SiO_2/Si substrate, with evident photovoltaic effects observed. The statistic result of the short-circuit currents under different laser powers were extracted to examine the device uniformity, with values comparable to devices made by CVD-grown materials. This work provides pathways for the large-scale fabrication of ultrathin all 2D optoelectronics that forms the basis of 2D pixelated cameras and displays.

In *Chapter 5*, the graphene-WS_2 van der Waals Schottky heterojunction was explored. I show the device of WS_2 with laterally spaced graphene electrodes behaves as a diode with a rectification ratio up to 90 under a laser power of 1.37 μW at a bias voltage of ±3 V. This is attributed by the different dielectric environments of two graphene electrodes, leading to asymmetric Schottky barriers of $graphene_{bottom}$-WS_2 and $graphene_{top}$-WS_2. It is then evidenced by constructing a symmetric structure, $graphene_{bottom}$-WS_2-$graphene_{bottom}$. Both the laser illumination and back-gate voltage can tune the rectification behaviour of the device. Furthermore, a constant bias voltage applied to the device causes a strong EL in the junction area, with an average current of 2.16×10^{-5} A. This work contributes to the current understanding of the 2D metal−semiconductor heterojunction and offers an idea to obtain all-2D Schottky diodes by retaining the ultrathin device concept.

Finally in *Chapter 6*, a new type of photodetectors with an enhanced photodetecting efficiency was shown by creating the multi-stacked heterostructure. The average net photocurrent of the multi-stacked (graphene/WS_2/MoS_2/graphene/MoS_2/WS_2/graphene) device is increased around 2.3 times than that of the single-stacked (graphene/WS_2/MoS_2/graphene) one due to the improved light absorbed. This study brings forward a novel concept of multi-stacked architectures which extends the current research range and paves up ways for the high efficiency yet ultrathin photodetectors.

7.2 Future Outlook

It is believed that research in 2D materials will further explosively increase in the years to come, with diverse aspects across synthesis method, operation technology,

characterization assessment, and device applications. More novel 2D semiconductors are expected to be isolated with various band gaps, which will span the entire visible spectrum of red, green and blue. Monolayer WS_2 and MoS_2, which are already explored in this thesis, act as ideal 2D materials for the red channel. Monolayer 2D metal halide PbI_2 with a band gap of 2.35 eV and 2D GaS with 2.5 eV band gap are possible candidates for the green and blue channels[180,181]. This will result in extensively more work to bring to fruition for sure. Additionally, the devices can be fabricated on a wide range of substrates, starting with Si with 300 nm oxide, which can be seen as a standard device substrate, then to transparent glass, and flexible polymers such as PET[28,182,183]. Furthermore, the combination of 2D optoelectronics with textiles and fibres will lead to the exciting implementation in wearable and implantable technologies[184].

However, there are still many huge challenges remaining in this area, making the journey for the 2D optoelectronics from the lab to the fab yet to be difficult. On the one hand, the performance variations exist in the devices. This is because it is uneasy to obtain 2D materials with a very high uniformity across the wafer-scale, and the contamination between each layer introduced during the transfer is also a problem. On the other hand, 2D materials are sensitive to the external environment, such as the temperature, laser, strain, applied voltage and molecules in air, which will decrease their working performance and life time[115,122,185,186].

To conclude, the future of the 2D materials is promising in optoelectronic devices. The research focus is not only to replace some conventional materials, but more importantly, to show their own unique and unrivalled properties.

Appendix A Supporting Information of Chapter 4

A1 Image of the experimental setup

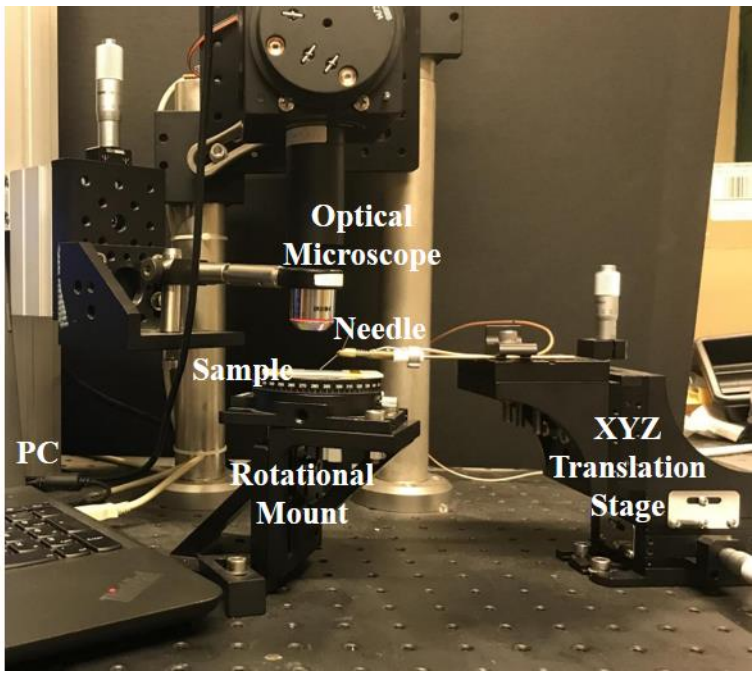


Figure A1 The experimental setup for the marker-assist aligned transfer. It consists of a rotational mount, a needle fixed to an XYZ translation stage, and an optical microscope connected to a laptop.

A2 TEM image of mono- and bilayer MoS_2

TEM was taken of the bilayer MoS_2 material. Some small area was found showing only a monolayer region which provides the monolayer-bilayer step edge. This shows the sample as bilayer with the 3R stacking structure.

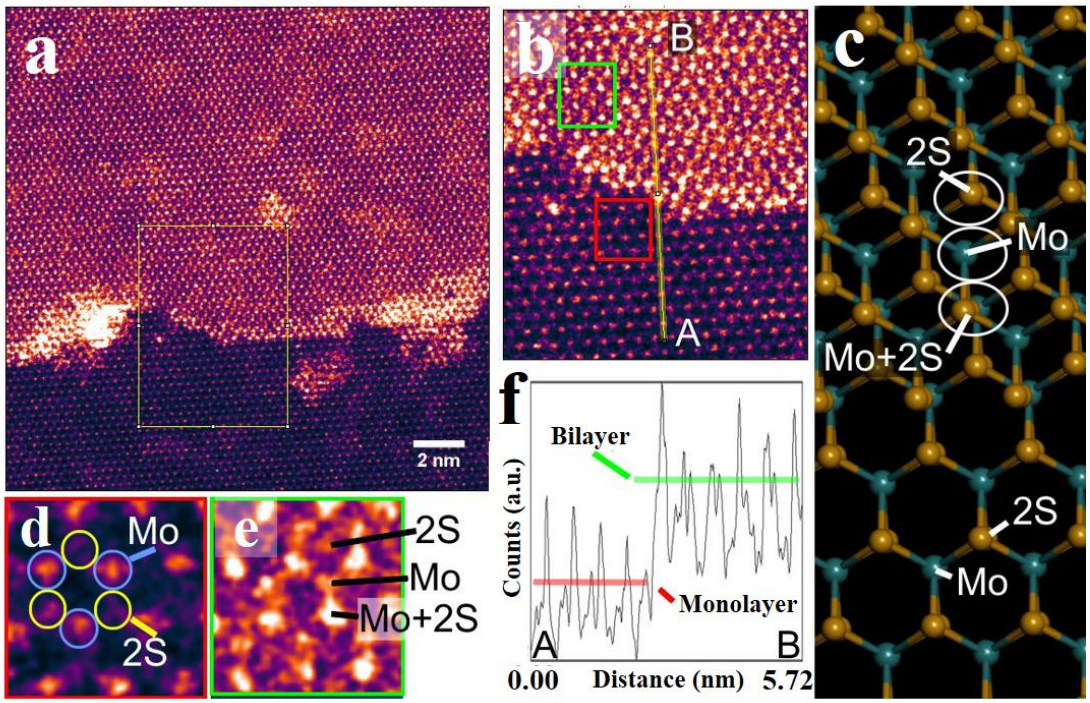


Figure A2 TEM characterization of the bilayer MoS_2. (a) ADF-STEM image of the mono- and bilayer MoS_2 film with false colour. (b) Magnified view of the boxed region in (a), showing the contrast between mono- and bilayer MoS_2. (c) Atomic model of the 3R-stacked bilayer MoS_2. White ellipses show the 2S, Mo, and Mo+2S columns. Model is slightly tilted in projection to observe the 3D depth. (d,e) Expanded view of the red and green box in (b), showing mono- and bilayer MoS_2, respectively. In (d), hexagonal lattices of MoS_2 with bright spots represent Mo atoms and dim spots represent two stacked S atoms. (f) Intensity line profile measured from the labelled region in (b).

A3 Raman spectra of bilayer graphene and monolayer MoS_2

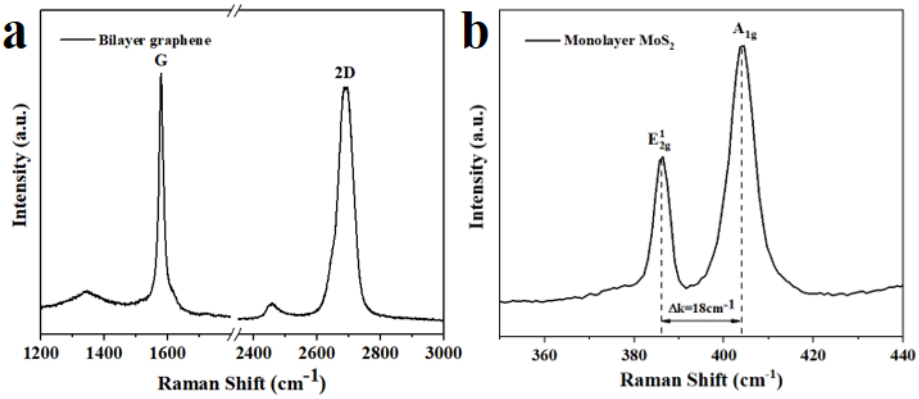


Figure A3 (a) Raman spectrum of bilayer graphene. (b) Raman spectrum of monolayer MoS_2 with a delta value of 18 cm^{-1}, in the range of our previous report[145].

A4 Transfer curve of the Gr/MoS_2(2L)/Gr device

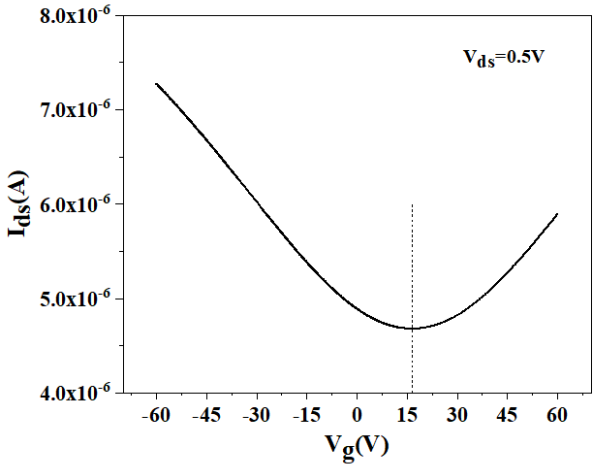


Figure A4 Transfer curve of the Gr/MoS_2(2L)/Gr device under 0.5 V fixed bias with SiO_2/Si substrate as the back gate. The V_{CNP} is around 17 V.

A5 Summary of the photovoltaic performances from our previous work and this work

Table A1 Gr/TMDs/Gr photodetectors with their corresponding active area, short-circuit current, laser power and back-gate voltage.

Device Structure	Active Area (μm^2)	I_{SC} (nA)	Laser Power (mW)	V_g (V)	Ref
Gr/WS_2(1L)/Gr	20 ×20	15	1.77	0	79
Gr/WS_2(2L)/Gr	20 ×20	900	1.77	0	79
Gr_B/WS_2/MoS_2/Gr_T	10 ×10	88	0.27	-60	161
Gr_B/MoS_2/WS_2/Gr_T	10 ×10	67	0.27	-60	161
Gr/WS_2(1L)/Gr	10 ×10	11	1.118	0	187
Gr_B/WS_2/h-BN(1-2L)/Gr_T	10 ×10	77	1.118	0	187
Gr_B/h-BN(1-2L)/WS_2/Gr_T	10 ×10	68	1.118	0	187
Gr_B/h-BN(3-5L)/WS_2/Gr_T	10 ×10	750	1.118	0	187
Gr/MoS_2(2L)/Gr	10 ×10	43.9	0.225	-60	This work
Gr_B/WS_2/MoS_2(2L)/Gr_T	10 × 10	195	1.118	0	This work

Appendix B Supporting Information of Chapter 5

B1. Band diagrams of the asymmetric and symmetric structures

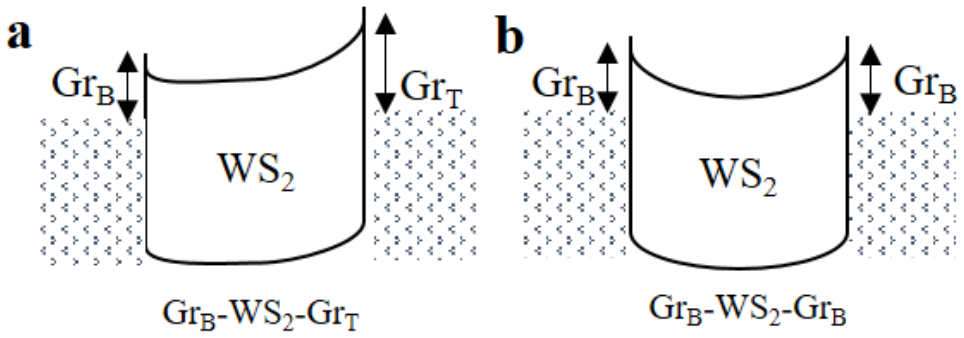


Figure B1 Band diagrams of the asymmetric (a) and symmetric (b) structures under zero bias and back-gate voltage. The top graphene is more p-doped than the bottom one. Therefore, the Fermi level of the top graphene is lower, resulting in a higher Schottky barrier.

B2. Electroluminescence of the Gr/WS_2/Gr vertical structure

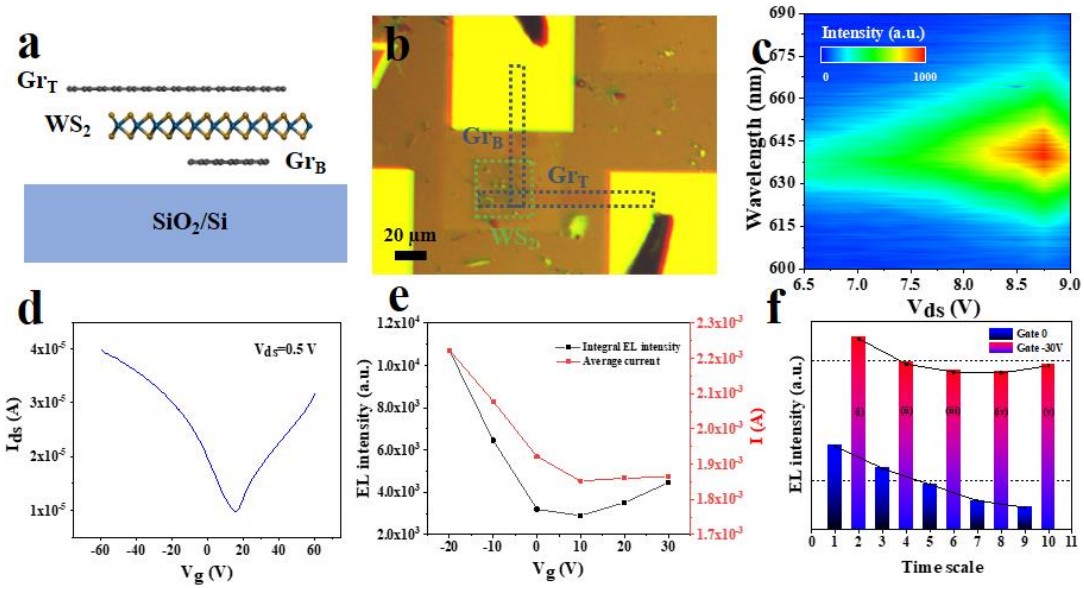


Figure B2 Electroluminescence of the vertical structure. (a) Atomic model and (b) optical image of a typical Gr/WS_2/Gr vertical structure where WS_2 is sandwiched between two graphene ribbons. (c) Spatial mapping of the EL spectra for the device when $V_{ds} > 0$. (d) Transfer curve of the device under a constant bias voltage of 0.5 V, similar like that of pristine graphene on SiO_2/Si substrate. The V_{CNP} is around 18 V. (e) EL intensity and current flow through the device as a function of the back-gate voltage. (f) Transient EL intensity characteristics under switch-on gate voltage ($V_g = -30$ V) and zero gate voltage.

Appendix C Supporting Information of Chapter 6

C1. Optical images of the corresponding devices for the statistical data

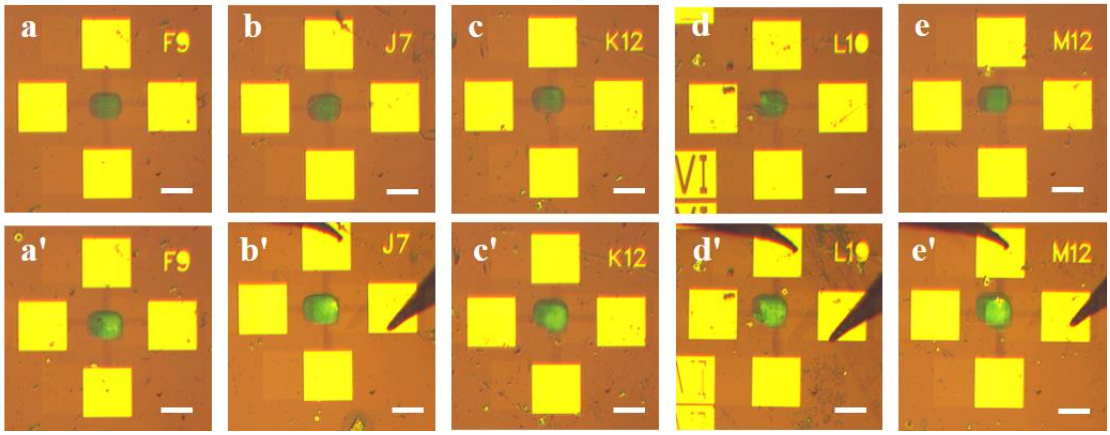


Figure C1 Optical images of the devices for the statistical data. (a-e) Optical images of the Gr/WS_2/MoS_2/Gr individual devices. (a'-e') Optical images of the corresponding Gr/WS_2/MoS_2/Gr/MoS_2/WS_2/Gr multi-stacked devices. Scale bar: 50 μm.

References

1. Novoselov, K. S. *et al.* Electric field effect in atomically thin carbon films. *Science* **306**, 666–669 (2004).
2. Akinwande, D. *et al.* A review on mechanics and mechanical properties of 2D materials—Graphene and beyond. *Extrem. Mech. Lett.* **13**, 42–77 (2017).
3. Nicolosi, V. *et al.* Liquid exfoliation of layered materials. *Science* **340**, 1226419 (2013).
4. Novoselov, K. S. *et al.* 2D materials and van der Waals heterostructures. *Science* **353**, aac9439 (2016).
5. Jariwala, D. *et al.* Mixed-dimensional van der Waals heterostructures. *Nat. Publ. Gr.* **16**, 170-181 (2016).
6. Britnell, L. *et al.* Strong light-matter interactions in heterostructures of atomically thin films. *Science* **340**, 1311–1315 (2013).
7. Tongay, S. *et al.* Tuning interlayer coupling in large-area heterostructures with CVD-grown MoS_2 and WS_2 monolayers. *Nano Lett.* **14**, (2014).
8. Zhang, J. *et al.* Observation of strong interlayer coupling in MoS_2/WS_2 heterostructures. *Adv. Mater.* **28**, 1950-1956 (2015).
9. Geim, A. K. *et al.* Van der Waals heterostructures. *Nature* **499**, 419–425 (2013).
10. Wan, X. *et al.* Focusing on energy and optoelectronic applications: A journey for graphene and graphene oxide at large scale. *Acc. Chem. Res.* **45**, 598–607 (2012).
11. Morozov, S. V. *et al.* Giant intrinsic carrier mobilities in graphene and its bilayer. *Phys. Rev. Lett.* **100**, 11–14 (2008).
12. Nair, R. R. *et al.* Fine structure constant defines visual transparency of graphene. *Science (80).* **320**, 1308 (2008).
13. Ho, K. I. *et al.* A self-aligned high-mobility graphene transistor: decoupling the channel with fluorographene to reduce scattering. *Adv. Mater.* **27**, 6519–6525 (2015).

14. Peres, N. M. R. The electronic properties of graphene and its bilayer. *Vacuum* **83**, 1248–1252 (2009).

15. Du, X. *et al.* Fractional quantum Hall effect and insulating phase of Dirac electrons in graphene. *Nature* **462**, 192–195 (2009).

16. Chhowalla, M. *et al.* The chemistry of two-dimensional layered transition metal dichalcogenide nanosheets. *Nat. Chem.* **5**, 263–275 (2013).

17. Radisavljevic, B. *et al.* Single-layer MoS_2 transistors. *Nat. Nanotechnol.* **6**, 147–150 (2011).

18. Splendiani, A. *et al.* Emerging photoluminescence in monolayer MoS_2. *Nano Lett.* **10**, 1271–1275 (2010).

19. Wilson, J. A. *et al.* The transition metal dichalcogenides discussion and interpretation of the observed optical, electrical and structural properties. *Adv. Phys.* **18**, 193–335 (1969).

20. Mak, K. F. *et al.* Photonics and optoelectronics of 2D semiconductor transition metal dichalcogenides. *Nat. Photonics* **10**, 216–226 (2016).

21. Sallen, G. *et al.* Robust optical emission polarization in MoS_2 monolayers through selective valley excitation. *Phys. Rev. B - Condens. Matter Mater. Phys.* **86**, 3–6 (2012).

22. Reyes-Retana, J. A. *et al.* Spin-orbital effects in metal-dichalcogenide semiconducting monolayers. *Sci. Rep.* **6**, 1–10 (2016).

23. Mak, K. F. *et al.* Atomically thin MoS_2: A new direct-gap semiconductor. *Phys. Rev. Lett.* **105**, 2–5 (2010).

24. Sundaram, R. S. *et al.* Electroluminescence in single layer MoS_2. *Nano Lett.* **13**, 1416–1421 (2013).

25. Yin, Z. *et al.* Single-layer MoS_2 phototransistors. *ACS Nano* **6**, 74–80 (2012).

26. Lopez-Sanchez, O. *et al.* Ultrasensitive photodetectors based on monolayer MoS_2. *Nat. Nanotechnol.* **8**, 497–501 (2013).

27. Geim, A. K. Graphene : Status and Prospects. *Science* **324**, 1530–1535 (2009).

28. Bae, S. *et al.* Roll-to-roll production of 30-inch graphene films for transparent electrodes. *Nat. Nanotechnol.* **5**, 574–578 (2010).

29. Yi, M. *et al.* A review on mechanical exfoliation for the scalable production of graphene. *J. Mater. Chem. A* **3**, 11700–11715 (2015).

30. Castellanos-Gomez, A. *et al.* Laser-thinning of MoS_2: On demand generation of a single-layer semiconductor. *Nano Lett.* **12**, 3187–3192 (2012).

31. Shautsova, V. *et al.* Direct laser patterning and phase transformation of 2D $PdSe_2$ films for on-demand device fabrication. *ACS Nano* **13**, 14162–14171 (2019).

32. Hu, L. *et al.* Laser thinning and patterning of MoS_2 with layer-by-layer precision. *Sci. Rep.* **7**, 1–9 (2017).

33. Fratini, S. *et al.* Substrate-limited electron dynamics in graphene. *Phys. Rev. B - Condens. Matter Mater. Phys.* **77**, 1–5 (2008).

34. Wang, L. Y. *et al.* Seeded growth of 2D materials. *Matter* **4**, 2699–2701 (2021).

35. Patsha, A. *et al.* Seeded-growth of WS_2 atomic layers: The effect on chemical and optical properties. *Nanoscale* **11**, 22493–22503 (2019).

36. Kobayashi, T. *et al.* Production of a 100-m-long high-quality graphene transparent conductive film by roll-to-roll chemical vapor deposition and transfer process. *Appl. Phys. Lett.* **102**, 1–5 (2013).

37. Rong, Y. *et al.* Controlling sulphur precursor addition for large single crystal domains of WS_2. *Nanoscale* **6**, (2014).

38. Wang, S. *et al.* Shape Evolution of Monolayer MoS_2 Crystals Grown by Chemical Vapor Deposition. *Chem. Mater.* **26**, 6371–6379 (2014).

39. Rong, Y. *et al.* Controlled preferential oxidation of grain boundaries in monolayer tungsten disulfide for direct optical imaging. *ACS Nano* **9**, 3695–3703 (2015).

40. Sheng, Y. *et al.* Hydrogen addition for centimeter-sized monolayer tungsten disulfide continuous films by ambient pressure chemical vapor deposition. *Chem. Mater.* **29**, 4904–4911 (2017).

41. Wang, S. *et al.* Substrate control for large area continuous films of monolayer MoS_2 by atmospheric pressure chemical vapor deposition. *Nanotechnol.* **27**, 085604 (2016).

42. Sheng, Y. *et al.* Uniformity of large-area bilayer graphene grown by chemical vapor deposition. *Nanotechnol.* **26**, (2015).

43. Oshima, C. *et al.* Hetero-epitaxial-double-atomic-layer system of monolayer graphene/monolayer h-BN on Ni(111). *Solid State Commun.* **116**, 37–40 (2000).

44. Ding, X. *et al.* Direct growth of few layer graphene on hexagonal boron nitride by chemical vapor deposition. *Carbon N. Y.* **49**, 2522–2525 (2011).

45. Son, M. *et al.* Direct growth of graphene pad on exfoliated hexagonal boron nitride surface. *Nanoscale* **3**, 3089 (2011).

46. Tang, S. *et al.* Nucleation and growth of single crystal graphene on hexagonal boron nitride. *Carbon N. Y.* **50**, 329–331 (2012).

47. Kim, S. M. *et al.* Synthesis of patched or stacked graphene and hBN flakes: A route to hybrid structure discovery. *Nano Lett.* **13**, 933–941 (2013).

48. Okada, M. *et al.* Direct chemical vapor deposition growth of WS_2 atomic layers on hexagonal boron nitride. *ACS Nano* **8**, 8273–8277 (2014).

49. Ling, X. *et al.* Role of the seeding promoter in MoS_2 growth by chemical vapor

deposition. *Nano Lett.* **14**, 464–472 (2014).

50. Wang, S. *et al.* All chemical vapor deposition growth of MoS_2:h-BN vertical van der Waals heterostructures. *ACS Nano* **9**, 5246–5254 (2015).

51. Rossi, A. *et al.* Scalable synthesis of WS_2 on graphene and h-BN: An all-2D platform for light-matter transduction. *2D Mater.* **3**, (2016).

52. Zhang, Z. *et al.* Direct chemical vapor deposition growth and band-gap characterization of MoS_2/h-BN van der Waals heterostructures on Au foils. *ACS Nano* **11**, 4328-4336 (2017).

53. Qian, Y. *et al.* Large-area high-quality AB-stacked bilayer graphene on h-BN/Pt foil by chemical vapor deposition. *ACS Appl. Mater. Interfaces* **10**, 29069−29075 (2018).

54. Makino, R. *et al.* Controlled CVD growth of lateral and vertical graphene/h-BN heterostructures. *Appl. Phys. Express* **13**, (2020).

55. Hong, M. *et al.* Applied surface science controlled growth of in-plane graphene/h-BN heterostructure on a single crystal Ge substrate. *Appl. Surf. Sci.* **554**, 149655 (2021).

56. Chen, T. *et al.* Hydrogen-assisted growth of large-Area continuous films of MoS_2 on monolayer graphene. *ACS Appl. Mater. Interfaces* **10**, 7304–7314 (2018).

57. Shi, Y. *et al.* Van der Waals epitaxy of MoS_2 layers using graphene as growth templates. *Nano Lett.* **12**, 2784–2791 (2012).

58. Lin, Y.-C. *et al.* Direct synthesis of van der Waals solids. *ACS Nano* **8**, 3715–3723 (2014).

59. Liu, Z. *et al.* Direct growth of graphene/hexagonal boron nitride stacked layers. *Nano Lett.* **11**, 2032–2037 (2011).

60. McCreary, K. M. *et al.* Large-area synthesis of continuous and uniform MoS_2 monolayer films on graphene. *Adv. Funct. Mater.* **24**, 6449–6454 (2014).

61. Chen, C. *et al.* Large-scale synthesis of a uniform film of bilayer MoS_2 on graphene for 2D heterostructure phototransistors. *ACS Appl. Mater. Interfaces* **8**, 19004–19011 (2016).

62. Novoselov, K. S. *et al.* Two-dimensional crystals-based heterostructures: Materials with tailored properties. *Phys. Scr.* 014006 (2012).

63. Barin, G. B. *et al.* Optimized graphene transfer: Influence of polymethylmethacrylate (PMMA) layer concentration and baking time on grapheme final performance. *Carbon N. Y.* **84**, 82–90 (2015).

64. Van Ngoc, H. *et al.* PMMA-etching-free transfer of wafer-scale chemical vapor deposition two-dimensional atomic crystal by a water soluble polyvinyl alcohol polymer method. *Sci. Rep.* **6**, 1–9 (2016).

65. Sabki, S. N. *et al.* Graphene transfer process and optimization of graphene coverage. *EPJ Web of Conferences* **162**, 01049 (2017).

66. Ando, T. Screening effect and impurity scattering in monolayer graphene. *J. Phys. Soc. Japan* **75**, 1–7 (2006).

67. Hwang, E. H. *et al.* Carrier transport in two-dimensional graphene layers. *Phys. Rev. Lett.* **98**, 2–5 (2007).

68. Chen, J. H. *et al.* Intrinsic and extrinsic performance limits of graphene devices on SiO_2. *Nat. Nanotechnol.* **3**, 206–209 (2008).

69. Ishigami, M. *et al.* Atomic structure of graphene on SiO_2. *Nano Lett.* **7**, 1643–1648 (2007).

70. Katsnelson, M. *et al.* Electron scattering on microscopic corrugations in graphene. *Philos. Trans. R. Soc. A Math. Phys. Eng. Sci.* **366**, 195–204 (2008).

71. Dean, C. R. *et al.* Boron nitride substrates for high-quality graphene electronics. *Nat. Nanotechnol.* **5**, 722–726 (2010).

72. Roy, K. *et al.* Graphene-MoS_2 hybrid structures for multifunctional photoresponsive memory devices. *Nat. Nanotechnol.* **8**, 826–830 (2013).

73. Bertolazzi, S. *et al.* Nonvolatile memory cells based on MoS_2/graphene heterostructures. *ACS Nano* **7**, 3246–3252 (2013).

74. Lee, G.-H. *et al.* Flexible and transparent MoS_2 field-effect transistors on hexagonal boron nitride-graphene heterostructures. *ACS Nano* **7**, 7931–7936 (2013).

75. Zomer, P. J. *et al.* A transfer technique for high mobility graphene devices on commercially available hexagonal boron nitride. *Appl. Phys. Lett.* **99**, (2011).

76. Schneider, G. F. *et al.* Wedging transfer of nanostructures. *Nano Lett.* **10**, 1912–1916 (2010).

77. Sheng, Y. *et al.* Mixed multilayered vertical heterostructures utilizing strained monolayer WS_2. *Nanoscale* **8**, 2639–2647 (2016).

78. Tan, H. *et al.* Lateral graphene-contacted vertically stacked WS_2/MoS_2 hybrid photodetectors with large gain. *Adv. Mater.* **29**, 1–8 (2017).

79. Zhou, Y. *et al.* Utilizing interlayer excitons in bilayer WS_2 for increased photovoltaic response in ultrathin graphene vertical cross-bar photodetecting tunneling transistors. *ACS Nano* **12**, 4669–4677 (2018).

80. Castellanos-Gomez, A. *et al.* Deterministic transfer of two-dimensional materials by all-dry viscoelastic stamping. *2D Mater.* **1**, (2014).

81. Buscema, M. *et al.* Photocurrent generation with two-dimensional van der Waals semiconductors. *Chem. Soc. Rev.* **44**, 3691–3718 (2015).

82. Park, J. *et al.* Imaging of photocurrent generation and collection in single-layer graphene. *Nano Lett.* **9**, 16–18 (2009).

83. Buscema, M. *et al.* Large and tunable photothermoelectric effect in single-layer MoS_2. *Nano Lett.* **13**, 358–363 (2013).

84. Groenendijk, D. J. *et al.* Photovoltaic and photothermoelectric effect in a double-gated WSe_2 device. *Nano Lett.* **14**, 5846–5852 (2014).

85. Freitag, M. *et al.* Photoconductivity of biased graphene. *Nat. Photonics* **7**, 53–59 (2013).

86. Vicarelli, L. *et al.* Graphene field-effect transistors as room-temperature terahertz detectors. *Nat. Mater.* **11**, 865–871 (2012).

87. Kwon, H. J. *et al.* Analysis of flicker noise in two-dimensional multilayer MoS_2 transistors. *Appl. Phys. Lett.* **104**, 1–5 (2014).

88. Renteria, J. *et al.* Low-frequency 1/f noise in MoS_2 transistors: Relative contributions of the channel and contacts. *Appl. Phys. Lett.* **104**, 153104 (2014).

89. Ghatak, S. *et al.* Microscopic origin of low frequency noise in MoS_2 field-effect transistors. *APL Mater.* **2**, 092515 (2014).

90. Kufer, D. *et al.* Highly sensitive, encapsulated MoS_2 photodetector with gate controllable gain and speed. *Nano Lett.* **15**, 7307–7313 (2015).

91. Lee, E. J. H. *et al.* Contact and edge effects in graphene devices. *Nat. Nanotechnol.* **3**, 486–490 (2008).

92. Xia, F. *et al.* Photocurrent imaging and efficient photon detection in a graphene transistor. *Nano Lett.* **9**, 1039–1044 (2009).

93. Xia, F. *et al.* Ultrafast graphene photodetector. *Nat. Nanotechnol.* **4**, 839–843 (2009).

94. Mueller, T. *et al.* Graphene photodetectors for high-speed optical communications. *Nat. Photonics* **4**, 297–301 (2010).

95. Yoo, T. J. *et al.* Zero-Bias operation of CVD graphene photodetector with asymmetric metal contacts. *ACS Photonics* **5**, 365–370 (2018).

96. Choi, W. *et al.* High-detectivity multilayer MoS_2 phototransistors with spectral response from ultraviolet to infrared. *Adv. Mater.* **24**, 5832–5836 (2012).

97. Jena, D. *et al.* Enhancement of carrier mobility in semiconductor nanostructures by dielectric engineering. *Phys. Rev. Lett.* **98**, 1–4 (2007).

98. Zhang, W. *et al.* High-gain phototransistors based on a CVD MoS_2 monolayer. *Adv. Mater.* **25**, 3456–3461 (2013).

99. Kretinin, A. V. *et al.* Electronic properties of graphene encapsulated with different two-dimensional atomic crystals. *Nano Lett.* **14**, 3270–3276 (2014).

100. Shautsova, V. *et al.* Hexagonal boron nitride assisted transfer and encapsulation of large area CVD graphene. *Sci. Rep.* **6**, 1–8 (2016).

101. Hong, X. *et al.* Ultrafast charge transfer in atomically thin MoS_2/WS_2 heterostructures. *Nat. Nanotechnol.* **9**, 682–686 (2014).

102. Huo, N. *et al.* Novel and enhanced optoelectronic performances of multilayer MoS_2-WS_2 heterostructure transistors. *Adv. Funct. Mater.* **24**, 7025–7031 (2014).

103. Xue, Y. *et al.* Scalable production of a few-Layer MoS_2/WS_2 vertical heterojunction array and its application for photodetectors. *ACS Nano* **10**, 573–580 (2016).

104. Tsai, D. S. *et al.* Few-layer MoS_2 with high broadband photogain and fast optical switching for use in harsh environments. *ACS Nano* **7**, 3905–3911 (2013).

105. Perea-López, N. *et al.* CVD-grown monolayered MoS_2 as an effective photosensor operating at low-voltage. *2D Mater.* **1**, (2014).

106. Kwon, J. *et al.* Giant Photoamplification in Indirect-Bandgap Multilayer MoS2Phototransistors with Local Bottom-Gate Structures. *Adv. Mater.* **27**, 2224–2230 (2015).

107. Kufer, D. *et al.* Highly sensitive, encapsulated MoS_2 photodetector with gate controllable gain and speed. *Nano Lett.* **15**, 7307–7313 (2015).

108. Wang, X. *et al.* Ultrasensitive and broadband MoS_2 photodetector driven by ferroelectrics. *Adv. Mater.* **27**, 6575–6581 (2015).

109. Kang, D. H. *et al.* High-performance transition metal dichalcogenide photodetectors enhanced by self-assembled monolayer doping. *Adv. Funct. Mater.* **25**, 4219–4227 (2015).

110. Abderrahmane, A. *et al.* High photosensitivity few-layered $MoSe_2$ back-gated field-effect phototransistors. *Nanotechnol.* **25**, 365202 (2014).

111. Xia, J. *et al.* CVD synthesis of large-area, highly crystalline $MoSe_2$ atomic layers on diverse substrates and application to photodetectors. *Nanoscale* **6**, 8949 (2014).

112. Jung, C. *et al.* Highly crystalline CVD-grown multilayer $MoSe_2$ thin film transistor for fast photodetector. *Sci. Rep.* **5**, 1–9 (2015).

113. Perea-Lõpez, N. *et al.* Photosensor device based on few-layered WS_2 films. *Adv. Funct. Mater.* **23**, 5511–5517 (2013).

114. Huo, N. *et al.* Photoresponsive and gas sensing field-effect transistors based on multilayer WS_2 nanoflakes. *Sci. Rep.* **4**, 5209 (2015).

115. Lan, C. *et al.* Large-area synthesis of monolayer WS_2 and its ambient-sensitive photo-detecting performance. *Nanoscale* **7**, 5974–5980 (2015).

116. Zhang, W. *et al.* Role of metal contacts in high-performance phototransistors based on WSe_2 monolayers. *ACS Nano* **8**, 8653–8661 (2014).

117. Chen, J. *et al.* Chemical vapor deposition of large-sized hexagonal WSe_2 crystals on dielectric substrates. *Adv. Mater.* **27**, 6722–6727 (2015).

118. Tan, H. *et al.* Ultrathin 2D photodetectors utilizing chemical vapor deposition grown WS_2 with graphene electrodes. *ACS Nano* **10**, 7866–7873 (2016).

119. Huo, N. *et al.* Interlayer coupling and optoelectronic properties of ultrathin two-dimensional heterostructures based on graphene, MoS_2 and WS_2. *J. Mater. Chem. C* **3**, 5467–5473 (2015).

120. Yu, W. J. *et al.* Unusually efficient photocurrent extraction in monolayer van der Waals heterostructure by tunnelling through discretized barriers. *Nat. Commun.* **7**, 1–9 (2016).

121. Wang, J. *et al.* Electroluminescent devices based on 2D semiconducting transition metal dichalcogenides. *Adv. Mater.* **30**, 1802687 (2018)

122. Sheng, Y. *et al.* High-performance WS_2 monolayer light-emitting tunneling devices using 2D materials grown by chemical vapor deposition. *ACS Nano* **13**, 4530-4537 (2019).

123. Hou, L. *et al.* Operational limits and failure mechanisms in all-2D van der Waals vertical heterostructure devices with long-lived persistent electroluminescence. *ACS Nano* **14**, 15533-15543 (2020).

124. Man, M. K. L. *et al.* Protecting the properties of monolayer MoS_2 on silicon based substrates with an atomically thin buffer. *Nat. Publ. Gr.* **6**, 20890 (2016).

125. Amani, M. *et al.* Near-unity photoluminescence quantum yield in MoS_2. Science **350**, 6264 (2015).

126. Amani, M. *et al.* Recombination kinetics and effects of superacid treatment in sulfur- and selenium-based transition metal dichalcogenides. *Nano Lett.* **16**, 2786−2791 (2016).

127. Jo, S. *et al.* Mono- and bilayer WS_2 light-emitting transistors. *Nano Lett.* **14**, 2019−2025 (2019).

128. Cheng, R. *et al.* Electroluminescence and photocurrent generation from atomically sharp WSe_2/MoS_2 heterojunction p−n diodes. *Nano Lett.* **14**, 5590−5597 (2014).

129. Withers, F. *et al.* Light-emitting diodes by band-structure engineering in van der Waals heterostructures. *Nat. Mater.* **14**, 301–306 (2015).

130. Rivera, P. *et al.* Observation of long-lived interlayer excitons in monolayer $MoSe_2$-WSe_2 heterostructures. *Nat. Commun.* **6**, 4–9 (2015).

131. Rivera, P. *et al.* Valley-polarized exciton dynamics in a 2D semiconductor heterostructure. *Science* **351**, 6274 (2016).

132. Ross, J. S. *et al.* Interlayer exciton optoelectronics in a 2D heterostructure p−n junction. *Nano Lett.* **17**, 638−643 (2017).

133. Cheng, R. *et al.* Electroluminescence and photocurrent generation from atomically sharp WSe_2/MoS_2 heterojunction p-n diodes. *Nano Lett.* **14**, 5590–5597 (2014).

134. Sundaram, R. S. *et al.* Electroluminescence in single layer MoS_2. *Nano Lett.* **13**, 1416−1421 (2013).

135. Baugher, B. W. H. *et al.* Optoelectronic devices based on electrically tunable p–n diodes in a monolayer dichalcogenide. *Nat. Nanotechnol.* **9**, 262-267 (2014).

136. Pospischil, A. *et al.* Solar-energy conversion and light emission in an atomic monolayer p–n diode. *Nat. Nanotechnol.* **9**, 257–261 (2014).

137. Ross, J. S. *et al.* Electrically tunable excitonic light-emitting diodes based on monolayer WSe_2 p–n junctions. *Nat. Nanotechnol.* **9**, 268–272 (2014).

138. Lopez-sanchez, O. *et al.* Terms of use light generation and harvesting in a van der Waals heterostructure. *ACS Nano* **8**, 3042–3048 (2014).

139. Ye, Y. *et al.* Exciton-dominant electroluminescence from a diode of monolayer MoS_2. *Appl. Phys. Lett.* **104**, 193508 (2014).

140. Withers, F. *et al.* WSe_2 Light-emitting tunneling transistors with enhanced brightness at room temperature. *Nano Lett.* **15**, 8223−8228 (2015).

141. Rong, Y. *et al.* Electroluminescence dynamics across grain boundary regions of monolayer tungsten disulfide. *ACS Nano* **10**, 1093–1100 (2016).

142. Palacios-berraquero, C. *et al.* Atomically thin quantum light-emitting diodes. *Nat. Commun.* **7**, 12978 (2016).

143. Wang, S. *et al.* Efficient carrier-to-exciton conversion in field emission tunnel diodes based on MIS-type van der Waals heterostack. *Nano Lett.* **17**, 5156−5162 (2017).

144. Xu, X. *et al.* Nanocavity integrated van der Waals heterostructure light-emitting tunneling diode. *Nano Lett.* **17**, 200−205 (2017).

145. Lu, Y. *et al.* Self-limiting growth of high-quality 2D monolayer MoS_2 by direct sulfurization using precursor-soluble substrates for advanced field-effect transistors and photodetectors. *ACS Appl. Nano Mater.* **2**, 369-378 (2018).

146. Ferrari, A. C. *et al.* Raman spectrum of graphene and graphene layers. *Phys. Rev. Lett.* **97**, 187401, (2006).

147. Li, H. *et al.* From bulk to monolayer MoS_2: evolution of Raman scattering. *Adv. Funct. Mater.* **22**, 1385–1390 (2012).

148. Das, A. *et al.* Monitoring dopants by Raman scattering in an electrochemically top-gated graphene transistor. *Nat. Nanotechnol.* **3**, 210–215 (2008).

149. Lee, C. *et al.* Anomalous lattice vibrations of single- and few-layer MoS_2. *ACS Nano* **4**, 2695–2700 (2010).

150. Berkdemir, A. *et al.* Identification of individual and few layers of WS_2 using

Raman Spectroscopy. *Sci. Rep.* **3**, 1–8 (2013).

151. Gusakova, J. *et al.* Electronic properties of bulk and monolayer TMDs: theoretical study within DFT framework (GVJ-2e Method). *Phys. Status Solidi Appl. Mater. Sci.* **214**, 1–7 (2017).

152. Xu, W. *et al.* Large dendritic monolayer MoS_2 grown by atmospheric pressure chemical vapor deposition for electrocatalysis. *ACS Appl. Mater. Interfaces* **10**, 4630-4639 (2018).

153. De, S. *et al.* Are there fundamental limitations on the sheet resistance and transmittance of thin graphene films? *ACS Nano* **4**, 2713–2720 (2010).

154. Peng, S. A. *et al.* The sheet resistance of graphene under contact and its effect on the derived specific contact resistivity. *Carbon N. Y.* **82**, 500–505 (2015).

155. Kim, M. S. *et al.* Sheet resistance analysis of interface-engineered multilayer graphene: mobility versus sheet carrier concentration. *ACS Appl. Mater. Interfaces* **12**, 30932–30940 (2020).

156. Bianco, G. V. *et al.* Extraordinary low sheet resistance of CVD graphene by thionyl chloride chemical doping. *Carbon N. Y.* **170**, 75–84 (2020).

157. Gong, C. *et al.* 2D nanomaterial arrays for electronics and optoelectronics. *Adv. Funct. Mater.* **28**, 1706559 (2018).

158. Borzda, T. *et al.* Charge photogeneration in few-layer MoS_2. *Adv. Funct. Mater.* **25**, 3351–3358 (2015).

159. Yu, W. J. *et al.* Highly efficient gate-tunable photocurrent generation in vertical heterostructures of layered materials. *Nat. Nanotechnol.* **8**, 952–958 (2013).

160. Chu, T. *et al.* Electrically tunable bandgaps in bilayer MoS_2. *Nano Lett.* **15**, 8000−8007 (2015).

161. Zhou, Y. *et al.* Symmetry-controlled reversible photovoltaic current flow in ultrathin all 2D vertically stacked graphene/MoS_2/WS_2/graphene devices. *ACS Appl. Mater. Interfaces* **11**, 2234-2242 (2019).

162. Huang, H. *et al.* High-performance two-dimensional Schottky diodes utilizing chemical vapour deposition-grown graphene–MoS_2 heterojunctions. *ACS Appl. Mater. Interfaces* **10**, 37258-37266 (2018).

163. Zhang, X. *et al.* Near-ideal van der Waals rectifiers based on all-two-dimensional Schottky junctions. *Nat. Commun.* **12**, 1–10 (2021).

164. Speed, P. *et al.*. Metal semiconductor field-effect transistor with MoS_2/conducting NiOx van der Waals Schottky interface for intrinsic high mobility and photoswitching speed. *ACS Nano* **9**, 8312–8320 (2015).

165. Liu, Y. *et al.* Van der Waals metal-semiconductor junction: weak Fermi level pinning enables effective tuning of Schottky barrier. *Sci. Adv.* **2**, 1–7 (2016).

166. Quang, T. Le *et al.* Scanning tunneling spectroscopy of van der Waals graphene/

semiconductor interfaces: absence of Fermi level pinning. *2D Mater.* **4**, 035019 (2017).

167. Zhang, Q. *et al.* Large-scale uniform-patterned arrays of ultrathin all-2D vertical stacked photodetector devices. *ACS Appl. Mater. Interfaces* **13**, 34696–34704 (2021).

168. Huang, H. *et al.* 2D-layer-dependent behavior in lateral Au/WS_2/graphene photodiode devices with optical modulation of Schottky barriers. *ACS Appl. Nano Mater.* **1**, 6874-6881 (2018).

169. Sze S.M. *et al.* Physics of semiconductor devices. *America (NY).* **10**, 739–751 (1995).

170. Fan, Y. *et al.* Photoinduced Schottky barrier lowering in 2D monolayer WS_2 photodetectors. *Adv. Opt. Mater.* **4**, 1573–1581 (2016).

171. Rathi, S. *et al.* Tunable electrical and optical characteristics in monolayer graphene and few-layer MoS_2 heterostructure devices. *Nano Lett.* **15**, 5017–5024 (2015).

172. Shih, C. J. *et al.* Tuning on-off current ratio and field-effect mobility in a MoS_2-graphene heterostructure via schottky barrier modulation. *ACS Nano* **8**, 5790–5798 (2014).

173. Tian, H. *et al.* Novel field-effect schottky barrier transistors based on graphene-MoS_2 heterojunctions. *Sci. Rep.* **4**, 1–9 (2014).

174. Chang, R.-J. *et al.* High-performance all 2D-layered tin disulfide: graphene photodetecting transistors with thickness-controlled interface dynamics. *ACS Appl. Mater. Interfaces* **10**, 13002-13010 (2018).

175. Bernardi, M. *et al.* Extraordinary sunlight absorption and one nanometer thick photovoltaics using two-dimensional monolayer materials. Nano Lett. **13**, 3664−3670 (2013).

176. Li, Q. *et al.* Engineering optical absorption in graphene and other 2D materials: advances and applications. *Adv. Opt. Mater.* **7**, 1–23 (2019).

177. Zeng, H. *et al.* Optical signature of symmetry variations and spin-valley coupling in atomically thin tungsten dichalcogenides. *Sci. Rep.* **3**, 2–6 (2013).

178. Zhang, J. *et al.* Enhancing and controlling valley magnetic response in MoS_2/WS_2 heterostructures by all-optical route. *Nat. Commun.* **10**, 1–8 (2019).

179. Britnell, L. *et al.* Electron tunneling through ultrathin boron nitride crystalline barriers. *Nano Lett.* **12**, 1707–1710 (2012).

180. Zhang, J. *et al.* Layered ultrathin PbI_2 single crystals for high sensitivity flexible photodetectors. *J. Mater. Chem. C* **3**, 4402–4406 (2015).

181. Jung, C. S. *et al.* Red-to-ultraviolet emission tuning of two-dimensional gallium sulfide. *ACS Nano* **9**, 9585–9593 (2015).

182. Tweedie, M. E. P. *et al.* Transparent ultrathin all-two-dimensional lateral Gr:WS_2:Gr photodetector arrays on flexible substrates and their strain induced failure mechanisms. *Mater. Today Adv.* **6**, 100067 (2020).

183. Georgiou, T. *et al.* Vertical field-effect transistor based on graphene-WS_2 heterostructures for flexible and transparent electronics. *Nat. Nanotechnol.* **8**, 100–103 (2013).

184. Xie, C. *et al.* Photodetectors based on two-dimensional layered materials beyond graphene. *Adv. Funct. Mater.* **27**, (2017).

185. Schedin, F. *et al.* Detection of individual gas molecules adsorbed on graphene. *Nat. Mater.* **6**, 652–655 (2007).

186. Tweedie, M. E. P. *et al.* Inhomogeneous strain release during bending of WS_2 on flexible substrates. *ACS Appl. Mater. Interfaces* **10**, 39177-39186 (2018).

187. Hou, L. *et al.* Photocurrent direction control and increased photovoltaic effects in all-2D ultrathin vertical heterostructures using asymmetric h-BN tunneling barriers. *ACS Appl. Mater. Interfaces* **11**, 40274-40282 (2019).